Failure of Peat Dikes due to Drought

Dimitrios Nterekas
1337262

September 2009

TU Delft
Faculty of Civil Engineering and Geosciences
Geotechnical Engineering

Failure of Peat Dikes due to Drought

Master Thesis
of
Dimitrios Nterekas

Supervisors:
Prof. Dr. Ir. F. Molenkamp, Delft University of Technology, CiTG
Dr. Ir. P.J. Visser, Delft University of Technology, CiTG
Ing. H.J. Everts, Delft University of Technology, CiTG
Ir. J.Herbschleb, Royal Haskoning
Ir. F.A.J.M. Mathijssen, Delft University of Technology, CiTG
Ir. J.P. Oostveen, Delft University of Technology, CiTG

September 2009

Summary

This research investigates the Wilnis dike failure that occurred in the dry summer of 2003. It is believed that drought played an important role in decreasing the stability of the dike, finally leading to failure. In the reported MSc project the situation during drought is simulated with the help of finite element method programs Plaxis and PlaxFlow in order to get more insight into the conditions that caused the dike to fail.

First a forensic analysis based on pictures taken directly after the breach is presented, followed by information about relevant failure cases. The interpretation of the soil investigation performed by GeoDelft after the failure is reviewed subsequently. The field data (Borings and Cone Penetration Tests) are used to define the stratification of the soil. The laboratory data (Triaxial, Simple Shear and Ko-CRS tests) are utilised to determine the soil parameters. With this information a finite element model is constructed in Plaxis. The material model used to simulate the different soil types is the Hardening Soil model.

In Plaxis and PlaxFlow 3 different calculation phases are defined. The first 2 have as a purpose to simulate the soil history until the start of drought since this is an important aspect in the further behaviour of soil during drought itself. The third one is the simulated drought period. All the groundwater flow related aspects (groundwater head, excess pore pressures etc.) are calculated by PlaxFlow while the related deformation and stability analyses are done by Plaxis.

A parametric study of the groundwater flow by PlaxFlow is performed leading to the conclusion that the upper layer of the soil consisting of Holland peat has to be separated into 2 parts along the middle of the slope of the dike in order to take the different degrees of saturation of the unsaturated soil above the groundwater table, that affect the unsaturated soil weight, into account.

Finally 9 different models are composed with varying strengths and permeabilities in order to take into consideration the effect of these parameters. The groundwater flow results are realistic. However the deformation results show irregular unexplainable patterns which are inconsistent with some of the observed data of the actual failure.

Furthermore the safety factors are calculated for the end of phase 2 (before drought) and phase 3 (after drought). These results are also very inconsistent and should be discarded.

Table of Contents

1 Introduction

1.1 General

About half of the area of the Netherlands is below sea level. Therefore the importance of flood defenses needs no further outlining. The flood defenses are divided in primary and secondary. Secondary flood defenses prevent polders from flooding. From these 14,000 km of secondary dikes about 3,500 km consist of peat dikes. Peat is abundant in the Netherlands and has been used in the past for many purposes. Actually many of the polders were created from the excavation of peat for fuel and the drying of these areas. These peat dikes are here for a long time and it was believed that they were safe. After some failures with the most recent one the failure of a peat dike at Wilnis in the summer of 2003 it was understood that the behavior of these dikes is still not clear. The calculations in existence return low safety factors for these dikes and the protective measures that are suggested by codes are sometimes unrealistic. It is clear that further research is needed in order to acquire more insight in the way peat dikes work and for possible mitigating measures.

1.2 Problem definition

The behavior of peat dikes in general and under drought in particular is not clear at the moment. Research is needed in order to get more insight into the failure mechanisms of peat dikes due to drought. Various aspects influence the stability of the dike. The most important are the material itself, the groundwater level in the dike as lowered by drought, cracks that may have occurred in the peat due to drought, deformation and seepage as well as the water pressure in the underlying permeable sand layer. During the research it will be attempted to see if any of these factors play a dominant role in the stability of peat dikes.

1.3 Research question

“What are the conditions for the failure of a peat dike to occur due to drought?”

1.4 Research approach

In this research only failure mechanisms connected to drought will be investigated. Since the failure in Wilnis happened due to drought it is obvious that groundwater flow and groundwater evaporation are essential in this case. The main tools that will be used for analysis are Plaxis and PlaxFlow. With these finite element method programs, which can work together, the situation in Wilnis will be simulated as realistically as possible. Insight into the way the failure occurred will be sought in terms of details of behaviour deteriorating the safety of the dike. In this way a better understanding will be gained about how peat dikes behave under drought and what corresponding risks they face. The input data for the research will be based on the interpretation of the soil investigation performed by GeoDelft after the failure. Full attention will be given to the raw data of the soil investigation and the laboratory tests in order to maximise the quality of the computational simulations of the processes in the peat dike, affecting its stability.

2 Case Histories

2.1 Wilnis case

The village of Wilnis is located about 30 km south of Amsterdam (see figure 2.1). There is a ring canal next to the road, which goes from the Vinkeveense Plassen, through Wilnis, towards the city of Mijdrecht. The surface soil layers in the area consist mainly of peat. In some areas the peat has been excavated for heating purposes in older times. One of these areas is the part of Wilnis north of the ring canal where the failure occurred. The polder surface level is 4.40 m below the dike crest. The breach happened in August 2003 one of the driest summers of the last years. A part of the dike around 50m in length moved horizontally to the north for about 10m. Water ran along both sides of the breach causing the north part of the village to flood. The canal was sealed off temporarily the same day. The drop of the water level in the canal due to the breach also caused the south quay to fail as well since the supporting force of the water disappeared. The surface level on the south side is the same as that of the crest of the dike because this area has not been excavated.

In this section photographs taken directly after the failure can be found. There is useful qualitative information that can be derived from these pictures. Below are some pictures of the wider breached dike area (Figures 2.2, 2.3, 2.4). In figures 2.2 and 2.4, on the right side, the same tree can be seen. There is also a crack in the surrounding soil which suggests that the tree stood steady in its position and the soil moved towards it. Therefore it can be concluded that the failure plane was not very deep at that point since the roots of the tree were obviously intact.

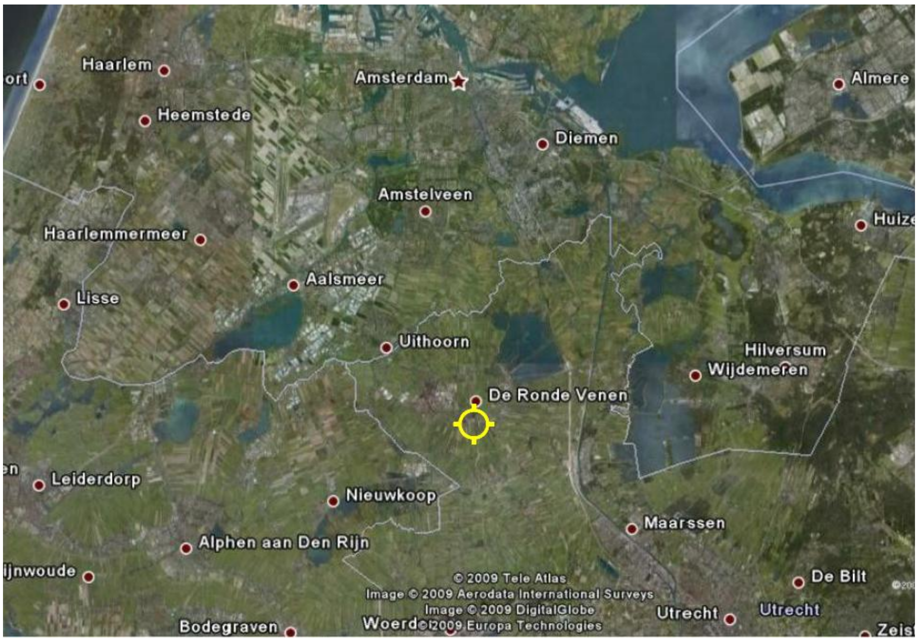

Figure 2.1: Position of Wilnis dike failure (yellow circle – map taken from Google Earth)

Figure 2.2: Aerial photograph of the breach – north to the right (photo from Utrechts Nieuwsblad)

Figure 2.3: Aerial photograph of the breach – north to top (photo from Utrechts Nieuwsblad)

Figure 2.4: Aerial photograph of the breach – north to right (photo from Utrechts Nieuwsblad)

In figure 2.5 the end of the slipped part of the dike can be seen. In this picture no ditch can be identified, something which suggests that the failure plane ended somewhere in the vicinity of the ditch. Also, the ground at the end of the slip surface did not lift very much, indicating some sort of horizontal and not circular failure.

Figure 2.5: End of slipped part of dike (photo by Ir. J.P. Oostveen)

Following is a picture of the sheet piling (Figure 2.6). It consists of wooden planks, 2 short ones in a row (length approximately 3.0m) and a longer one. The thickness of the wooden planks is about 5cm.

Figure 2.6: Wooden sheet piling of the dike (photo by Ir. J.P. Oostveen)

2.2 Similar cases

2.2.1 Boskoop, Rijnland

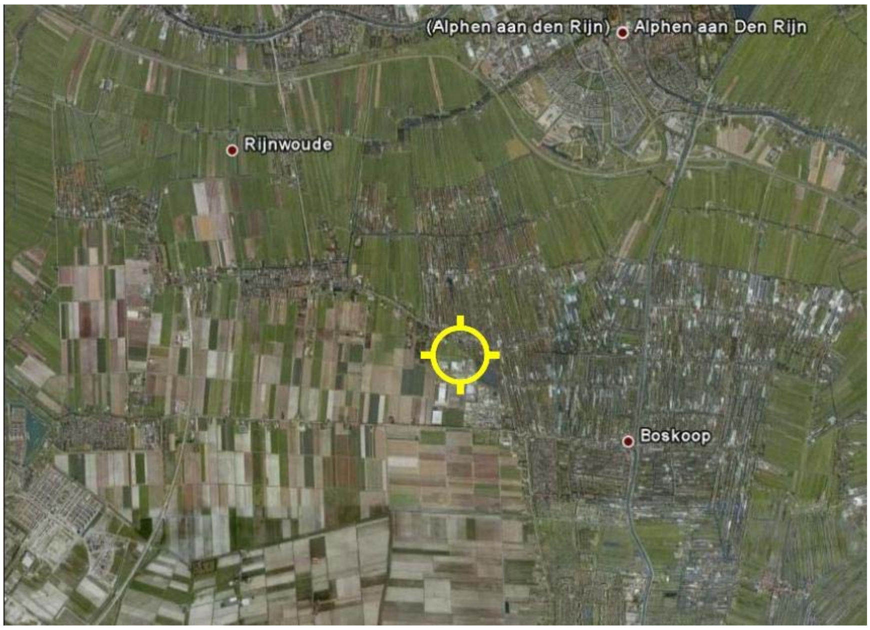

Figure 2.7: Position of Boskoop dike (yellow circle – map taken from Google Earth)

In the summer of 2006 in one of the peat dikes in Boskoop, Rijnland, cracks were observed in a peat dike. The summer of 2006 was a dry summer since there was little rain in the period from the end of May until August. The crest of the dike is at NAP -1.55m and the ditch at the toe of the dike at NAP -5.00m. There is sand from NAP -10.50m and deeper. This dike was not constructed but was created by excavation of the inner side. Therefore the situation is very similar to that of Wilnis. On July 27th and 28th there were visual inspections of the dike conducted by Rijnland which did not reveal any threats. Then, only 3 days afterwards on July 31st, a farmer called the waterboard of Rijnland because he saw some cracks in the dike. Engineers from the Rijnland waterboard (contact engineer: Jaap Stoop) immediately visited the site where they observed 3 cracks and a spot near the toe of the dike where water was coming out. The 3 cracks were parallel to each other and diagonal to the canal. Each was around 2.5m long and 5-10cm wide. There was water in the cracks that had the same level as the water in the canal something that suggests that there was a direct connection of the cracks with the canal. Possibly the peat had a high horizontal permeability or there was some kind of local discontinuity. The "hole" at the toe of the dike near the ditch, out of which water was coming, had floating soil pieces which also suggest a connection with the canal water. Further inspection of the dike revealed a crack at the bottom of the canal at a point where a wooden sheet pile was present. This sheet piling did not extend over the full length of the dike and was put at a specific point in order to deal with problems the dike had in the past.

The crack was between the wooden sheet pile and the peat on the side of the canal. When its depth was attempted to be measured it was not possible since it extended beyond 2.5m deep so it was out of reach for the engineers at that time. Below, in figure 2.8, a sketch of the situation can be seen where it is obvious that the pattern of the cracks is similar to the Wilnis failure. In order to avoid further deformation that would lead to failure the cracks in the canal were filled and covered by clay and 0.5m of clay was added to the toe of the dike to help stabilize it. Furthermore, the canal was blocked off by two dams to limit the amount of water potentially flooding the polder in case of a failure.

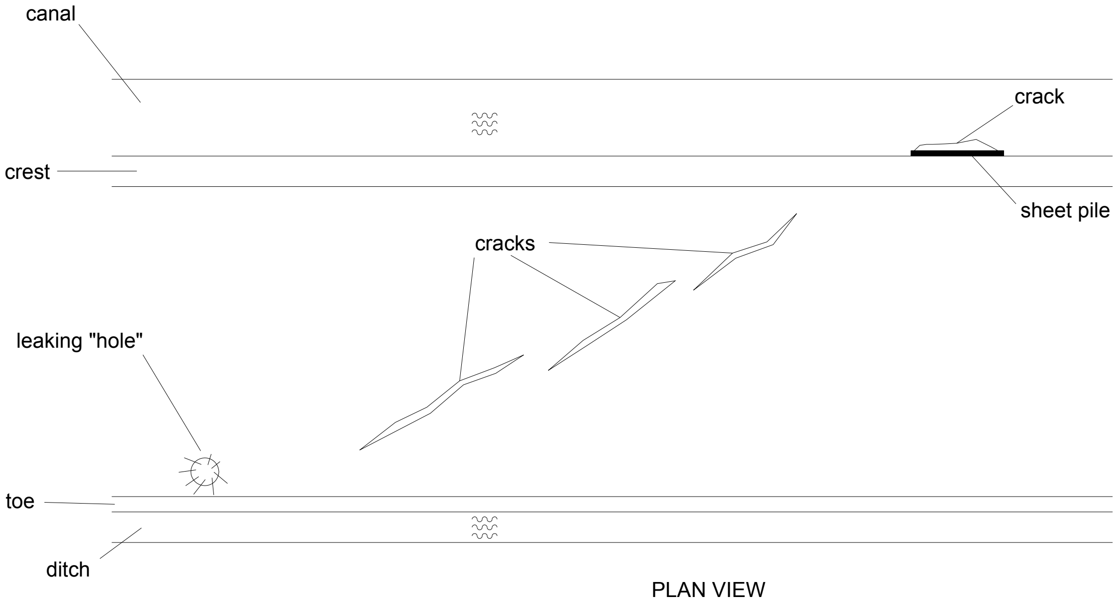

Figure 2.8: Plan view of the situation in Boskoop

2.2.2 Grand Canal, Edenburry, Ireland

Figure 2.9: Aerial photograph of the Grand Canal breach in Edenburry, Ireland (Pigott, 1992 [13])

On the 15th of January 1989 a large breach opened in the north bank of the Grand Canal near the town of Edenburry in Ireland (Figure 2.10). The breach extended over a length of 350m. A large block of the dike approximately 225 m by 105 m in plan view moved laterally for a maximum of 60 m at the eastern end and a few meters at the western. The southern bank was also damaged over a distance of 200 m as a result of the loss of the supporting water pressure. An eye-witness reported that the breach was accompanied by a loud “tearing” sound which suggests tension failure. Immediately after the breach a site investigation consisting of probes to determine the soil stratification, in-situ vane testing and the taking of piston samples was conducted.

The canal was constructed in the 18th century using air-dried peat as a fill material over deep bog. Clay was used for lining the bottom and the sides of the canal as well as the banks. The height of the dike was 3.5m. In order to avoid shear failure the side slopes were very flat leading to a dike that was 19m wide at crest and 135m wide at the toe. The total depth of the peat at the crest, including the fill and the deep bog, was 10m. The channel was 2.4m deep, 7m wide and was filled with water to a depth of 1.8m (see Figure 2.11).

Figure 2.10: Position of Edenberry dike failure (yellow circle – map taken from Google Earth)

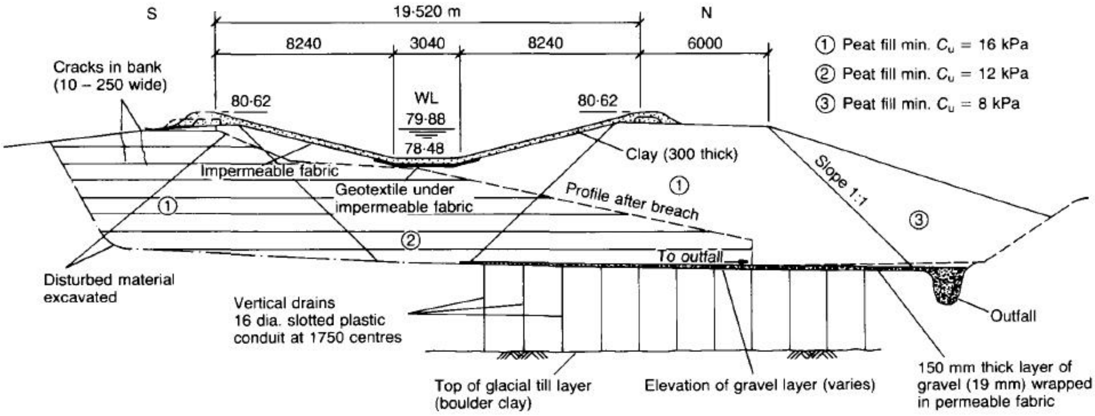

Figure 2.11: Cross-section of the Grand Canal in Ireland (Pigott, 1992 [13])

The failure plane was at a depth of 5.5m below the crest and had a downwards angle of 2.5^0 to the horizontal. The failure plane extended beyond the fill, into the original bog. According to Pigott, Hanrahan & Somers (1992) the failure was caused due to seepage from the canal through cracks in the lining caused by the settlement of the dike and due to shrinkage cracks on the dried peat caused by exposure. Therefore the groundwater level in the dike was raised and since peat has a volumetric weight almost the same as water this would result in a situation where effective stresses were almost zero. At this point the only resistance would come from the cohesion of peat, and since the dike was created by a fill possibly containing extraneous material this resistance could not have been considerable, leading to the failure of the dike.

3 Soil interpretation based on field and laboratory data

3.1 Overview of soil data

GeoDelft performed a number of in-situ and laboratory tests in order to determine the geotechnical characteristics of the area. Namely these tests include the following field data:

- 67 CPTs
- 48 Borings

and the following laboratory data:

- 15 Ko-CRS tests
- 12 Triaxial tests
- 13 Simple Shear tests

The CPTs and borings are spread longitudinally over a length of about 1700 m following the dike axis. A map containing the position of the CPTs and borings can be found in Appendix A, Drawing A1 (GeoDelft report 4, 2004 [38]). Details about the methods used for in-situ testing can be found in Appendix B (GeoDelft report 4, 2004 [38]) while details about the methods for laboratory testing can be found in Appendix C (GeoDelft report 1, 2003 [35]). Most of the soil samples that were tested in the laboratory were taken from borings on the east side of the breach.

3.2 In situ testing and resulting composition of peat dike

The determination of the soil stratification is based on the CPTs and borings performed. All measured data are available in electronic form which also includes the spatial information of each boring or CPT (i.e. the coordinates in x, y and z). Therefore, they can be placed in the right position on a map or in a drawing. The interpretation of the borings is naturally fixed since it was performed by a geologist in the laboratory directly after the samples were taken. A typical example of a borehole interpretation can be seen in figure 3.1 below. Three different soil types are distinguished, namely peat, clay and sand.

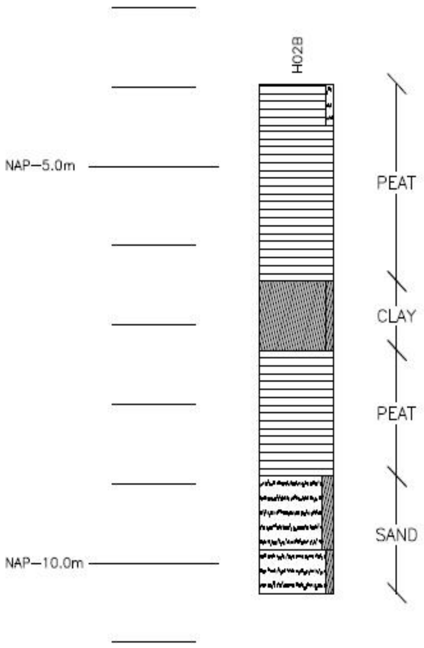

Figure 3.1: Borehole example (borehole H02B – GeoDelft report 4, 2004 [38])

The CPTs give 2 measurements over depth. One is the cone resistance q_c, measured in MPa, and the other is the dimensionless friction ratio R_f defined as $R_f=[(f_s/q_c)*100]$ where f_s is the sleeve friction. In figure 3.2 below the empirical rules for determining the soil type based on CPT measurements can be seen. In figure 3.3 a representative example of a CPT can be found. In the middle is the zero point, to the left is the measurement of the friction ratio R_f and to the right is the measurement of the cone resistance q_c.

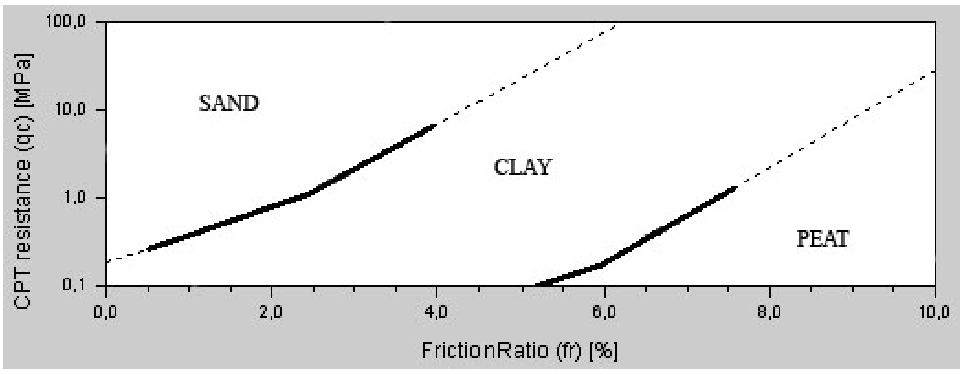

Figure 3.2: CPT interpretation rules

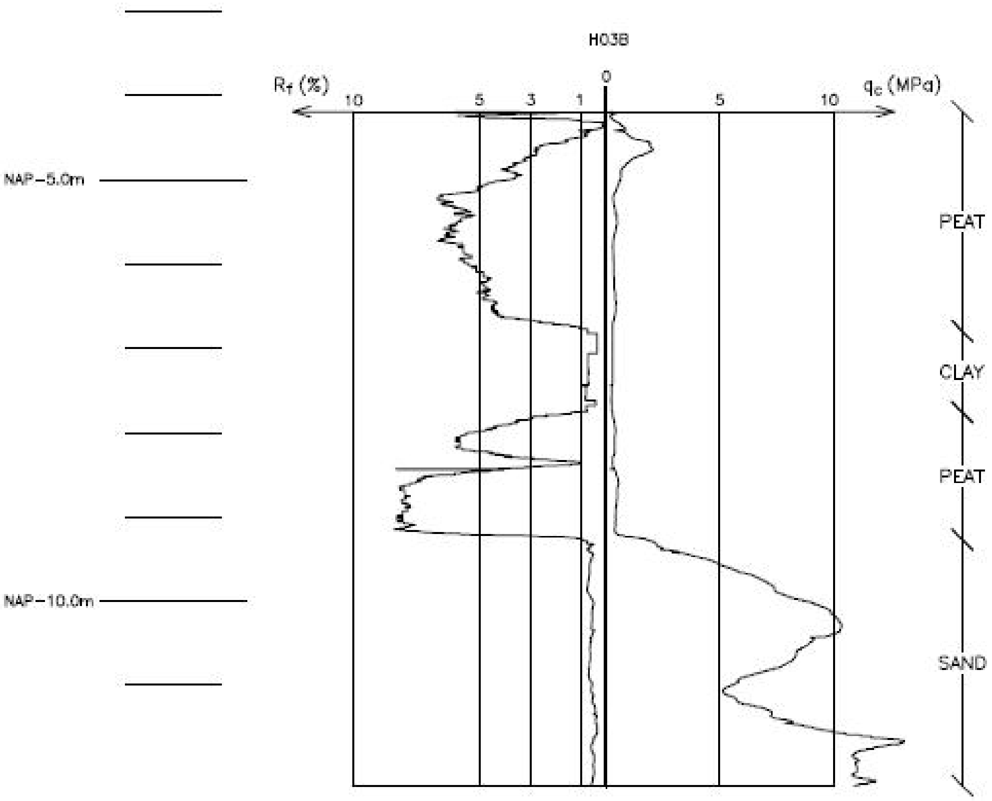

Figure 3.3: CPT interpretation example (CPT H03B – GeoDelft report 4, 2004 [38])

In most cases there were three borings or CPTs performed in a line perpendicular to the dike axis as can be seen in Drawing A1 of Appendix A, one at the crest, one at the slope of the dike and one at the toe. They cover a length of about 1.70 kilometers along the dike, with the area of the breach in the middle. There is a large number of CPTs and borings performed on the breached area but unfortunately no data are available at the places directly east and west of the breach. Such information could give better insight into both the soil stratification and properties of undisturbed soil, although at present the in-situ soil properties may have been affected by the ground works of the repairs. With the information currently available it was possible for 2 geotechnical cross sections to be created, sections AA and BB, both relatively far from the breach. Section AA (Figure 3.4) is located around 280 m west of the breach and section BB (Figure 3.5) about 150 m east of the breach. These large distances from the area that actually failed reduce the usefulness of these cross sections. Also three longitudinal geotechnical profiles were created at different distances from the dike axis following the pattern of the measured points, i.e. one at the crest, one at the slope and one at the toe. The measurements directly on the breach were not taken into account for these longitudinal profiles since the soil there was disturbed. In figures 3.4 and 3.5 below dashed lines have been added to indicate the point where CPTs or borings were performed. It should be noted that the surface lines of these two cross-sections were measured by GPS in 2008 and therefore are different from the actual surface level that existed prior to the breach since there has been sand added on top of the ground in order to increase the stability of the dike and avoid a future failure.

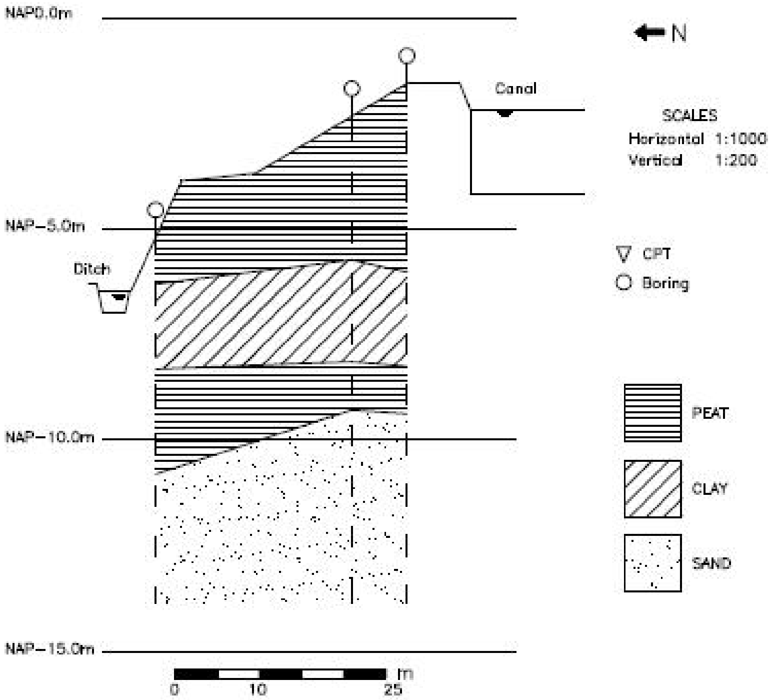

Figure 3.4: Cross section AA

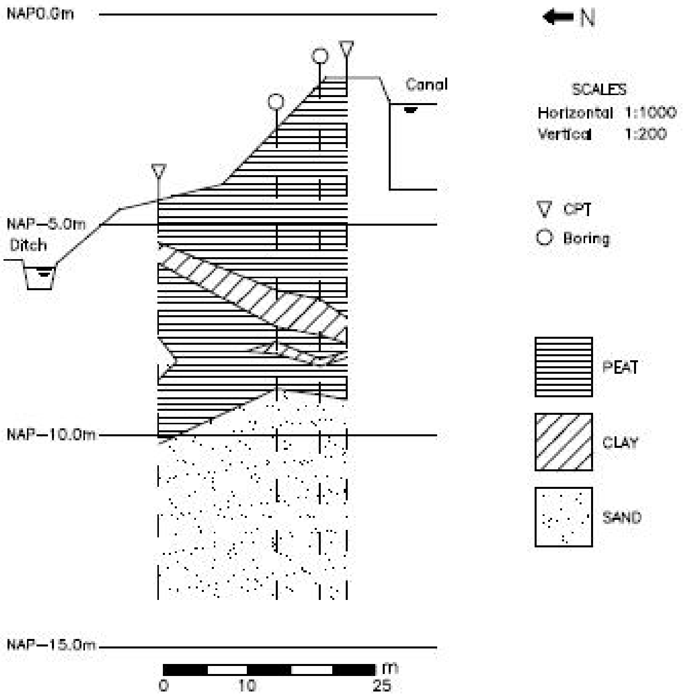

Figure 3.5: Cross section BB

In figure 3.5 above the clay layer seems to have an unrealistically high inclination and creates doubts about the reliability of the created cross-section something that can be attributed to 2 factors. Firstly, the 4 point measurements used (2 CPTs and 2 borings) were not actually in line to the axis of cross section BB (as was the case of cross section AA, see Drawing A1 in Appendix A) but at a distance and their position was projected on the axis of the cross-section. Secondly, the inclination of the clay layer is mostly a result of the CPTs and not the borings (which actually show the clay layer at a similar depth). This can be attributed to the reduced reliability of CPTs when compared to that of borings.

For the breached area a 3D model of the region was created with the help of the program Surfer. With this program surfaces can easily be created from point data by interpolation. The point information came from the CPTs and borings performed. In total 25 CPTs and borings were performed in an area roughly 110 m by 45 m. It should be noted that the measurements are not aligned on a grid and were taken at random points which decreases the accuracy of the created surfaces. The surfaces indicate the interfaces between different soil types. For the interpolation the Kriging method was used. Figure 3.6 shows a top view of the breached area along with the positions of the CPTs and borings, of the cross sections that were created from the 3D model and of the profile along the crest created from the CPTs. In figures 3.7 to 3.10 the created model with different soil layers can be seen.

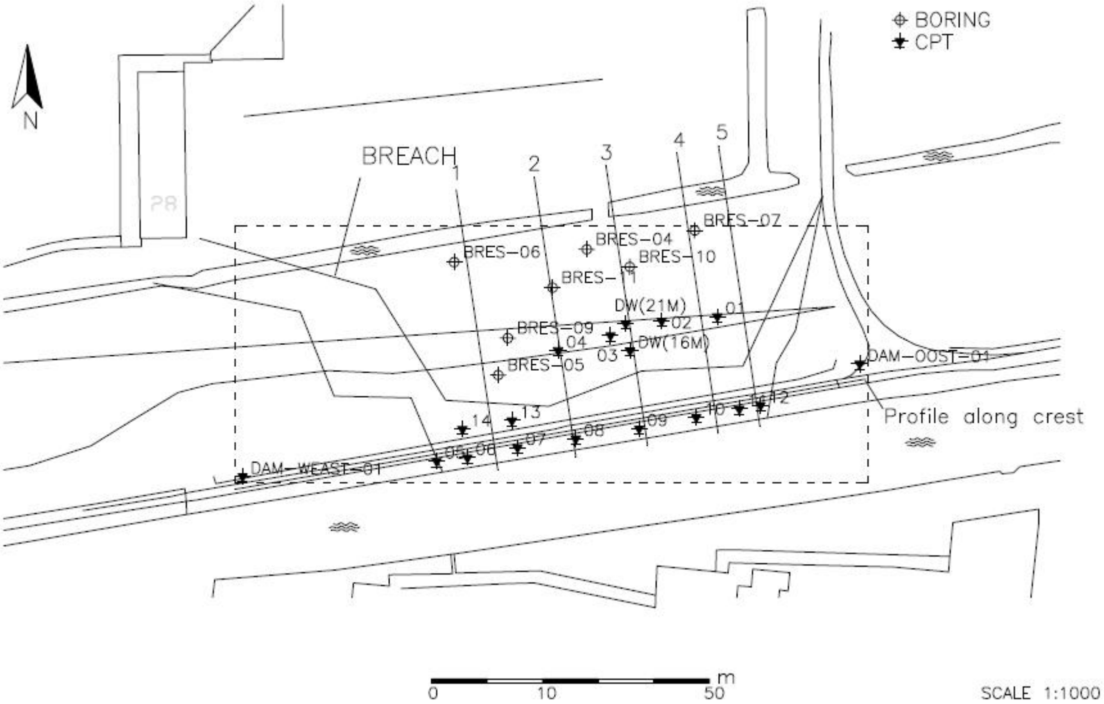

Figure 3.6: Top view of breached area, location of the 5 cross sections and of the crest profile (dashed line indicates the area that is included in the 3D model)

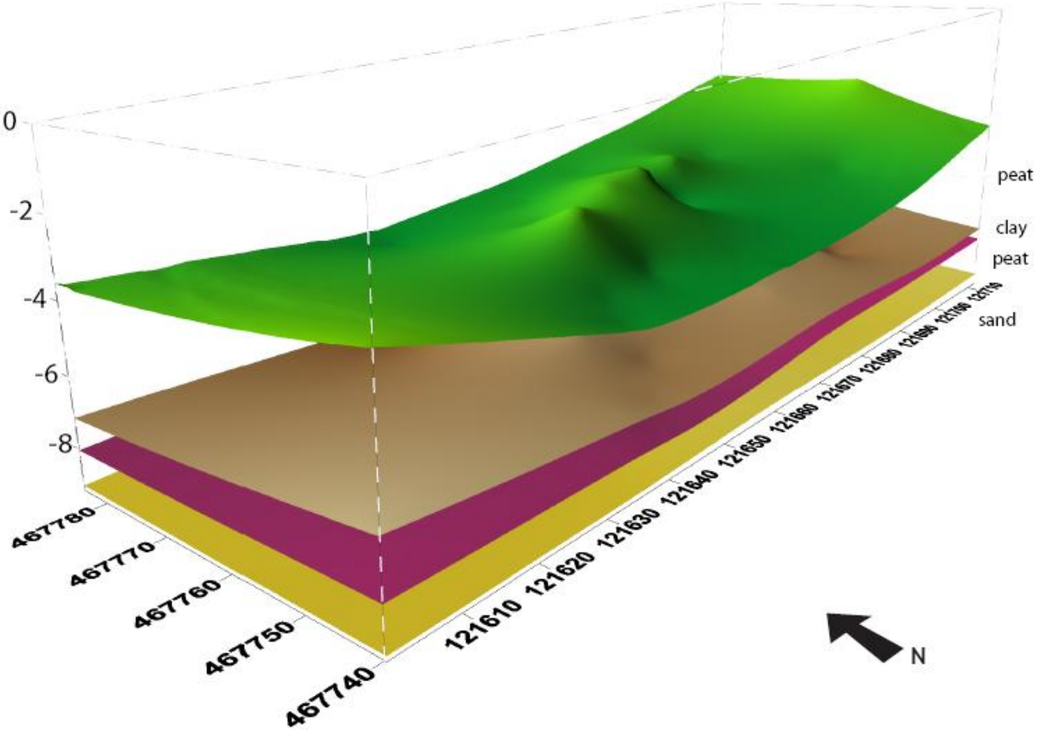

Figure 3.7: 3D model of breached area (green is ground level consisting of peat)

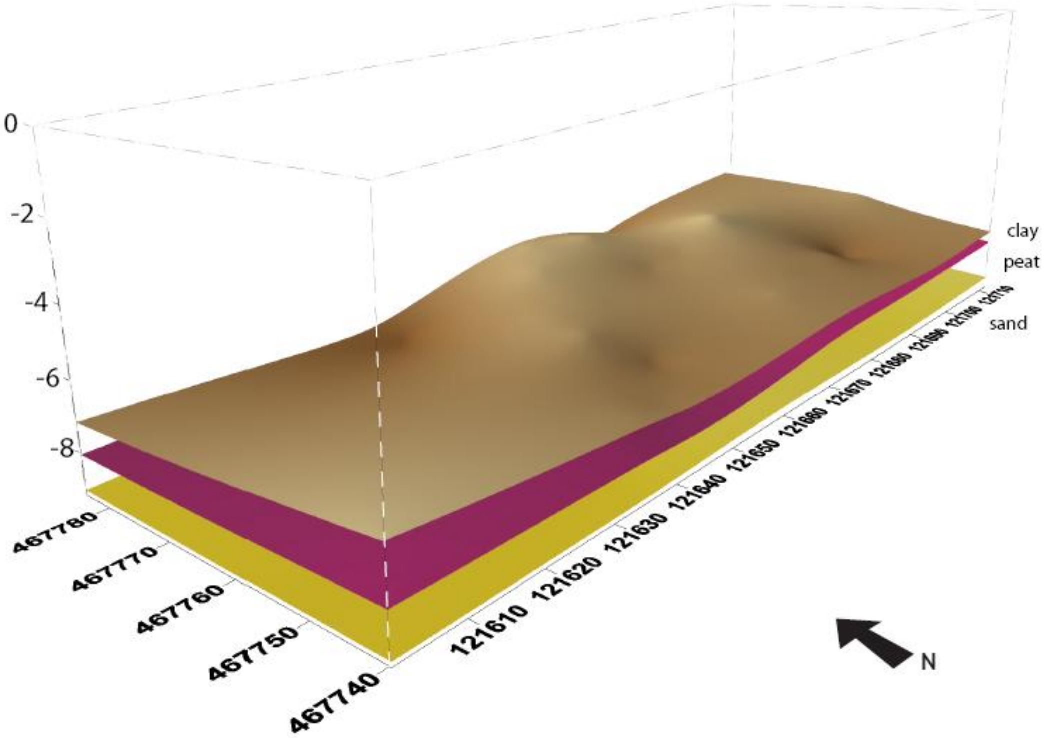

Figure 3.8: 3D model of breached area (brown is top of clay layer)

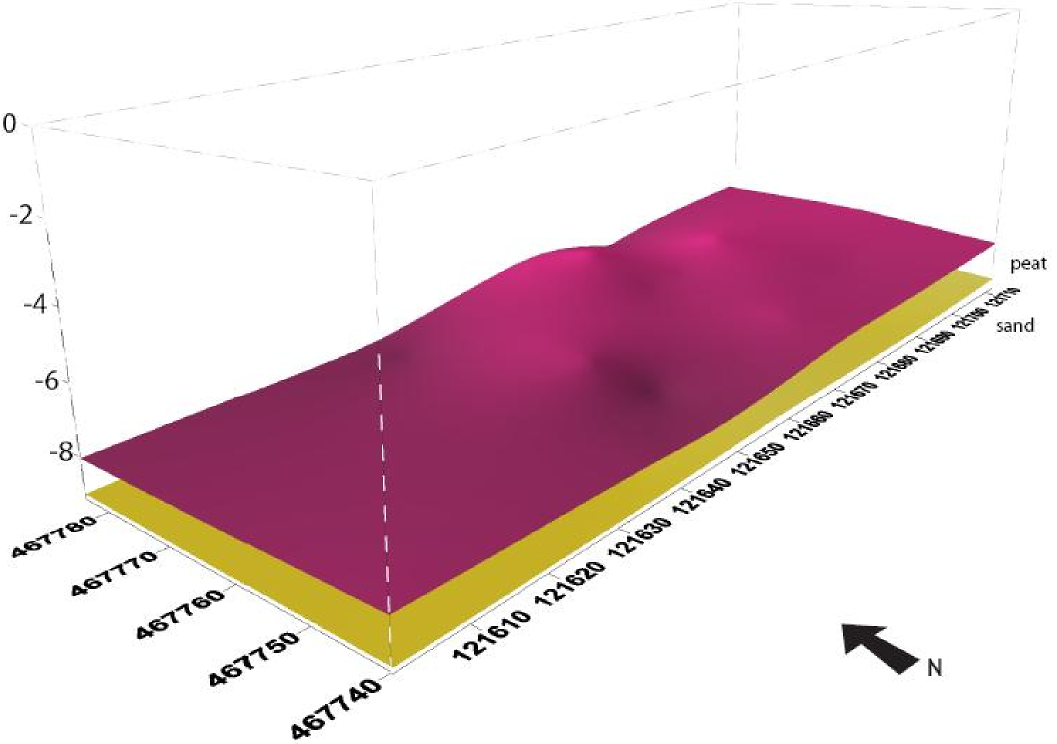

Figure 3.9: 3D model of breached area (purple is top of peat layer)

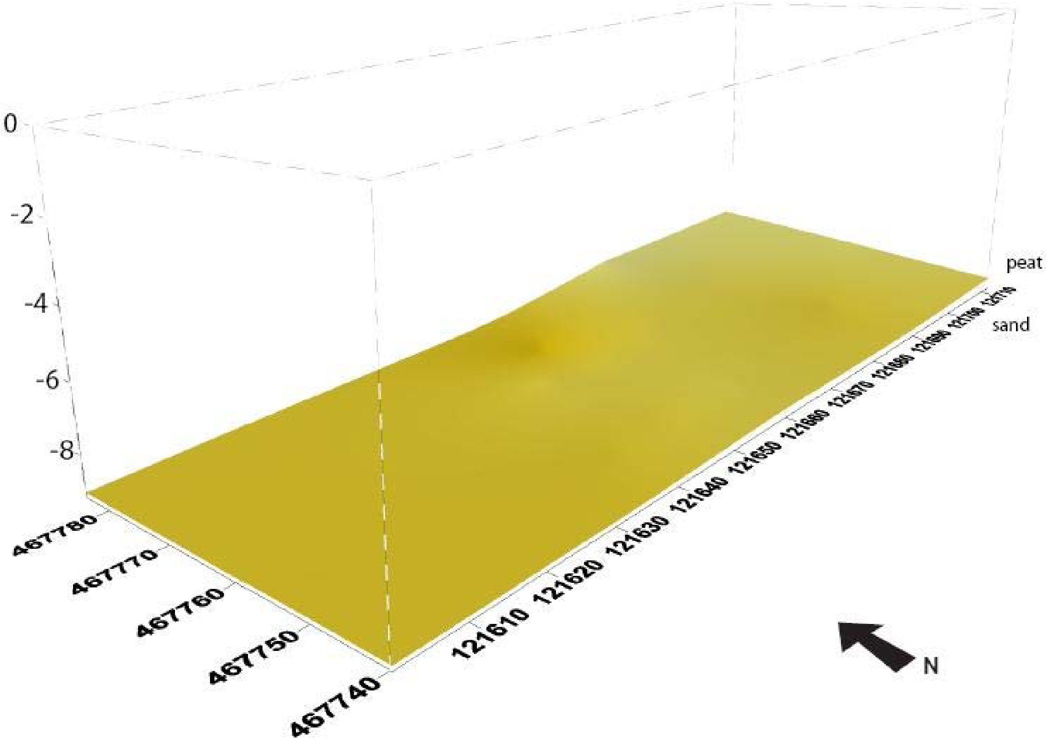

Figure 3.10: 3D model of breached area (yellow is top of sand layer)

As it can be seen from the figures above the soil stratification consists of a deep sand layer followed by peat, then a relatively thin clay layer and on top of that peat again until the ground surface. It can also be noted that at greater depth the soil layers seem more uniform and flat indicating a lower degree of disturbance.

From this model five cross sections of the area are created. In the figures 3.11 to 3.15 below these cross sections can be seen. Also in these figures the geometry of the dike before the breach (as measured by GeoDelft) has been imposed in order to get a more clear view of the ground movement. A rough estimation of the actual ground level directly after the breach is drawn with a dotted line.

Furthermore a longitudinal profile of the crest of the breached dike is shown in figure 3.16. The profile is created from the CPTs that were performed along the crest of the breached area. The positions of these CPTs as well as their names are visible in figure 3.16 with dashed lines. The position of the 5 cross-sections (figures 3.11 till and including 3.15) is shown in figure 3.16 with continuous lines and the dots represent the occurrence of the different soil layers according to the 5 cross-sections created from the 3D model.

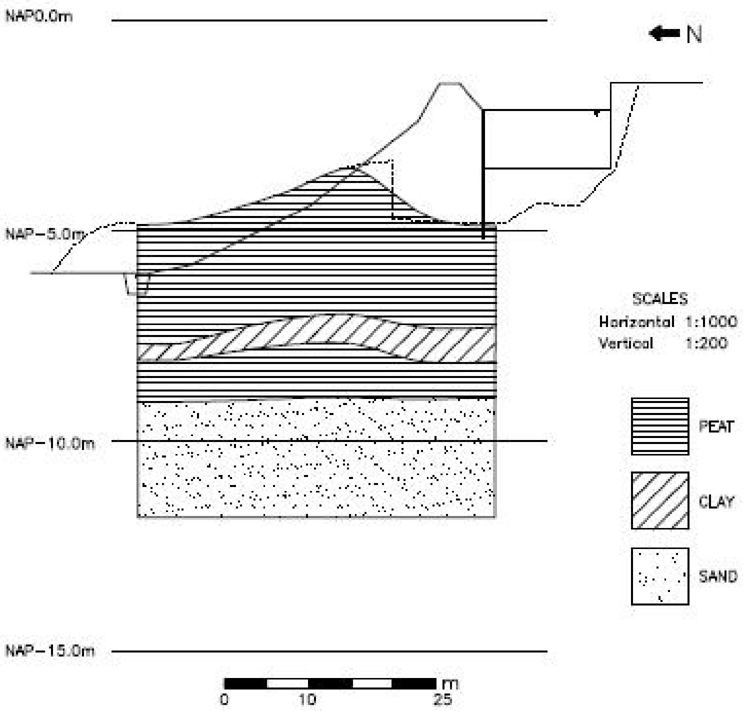

Figure 3.11: Cross section at breach 1 (far west side)

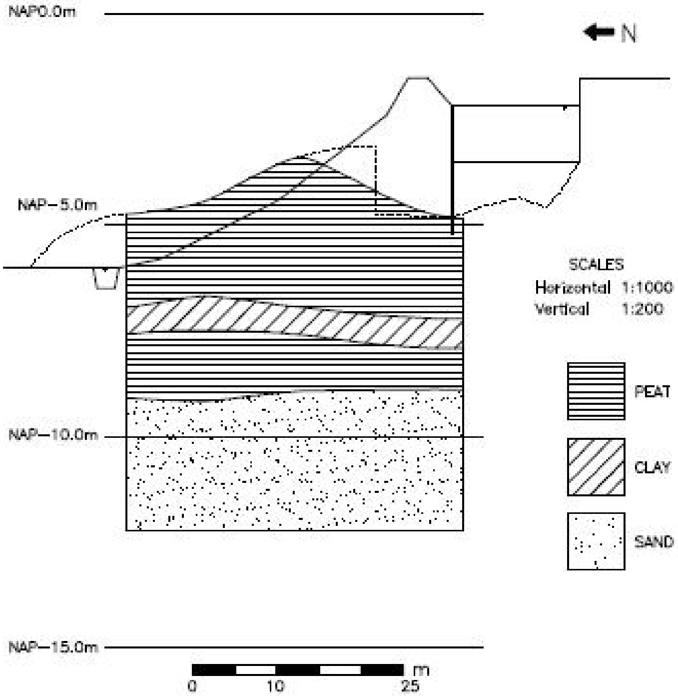

Figure 3.12: Cross section at breach 2 (west)

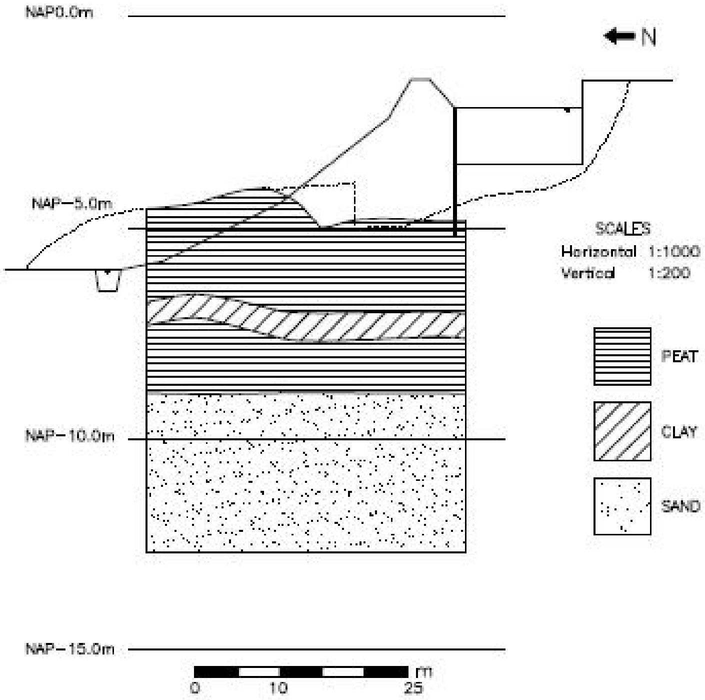

Figure 3.13: Cross section at breach 3 (middle)

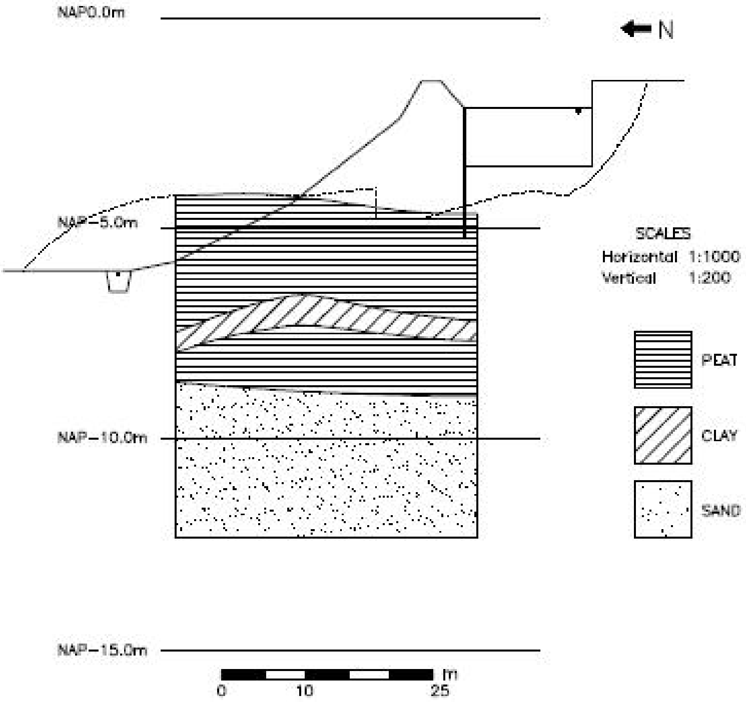

Figure 3.14: Cross section at breach 4 (east)

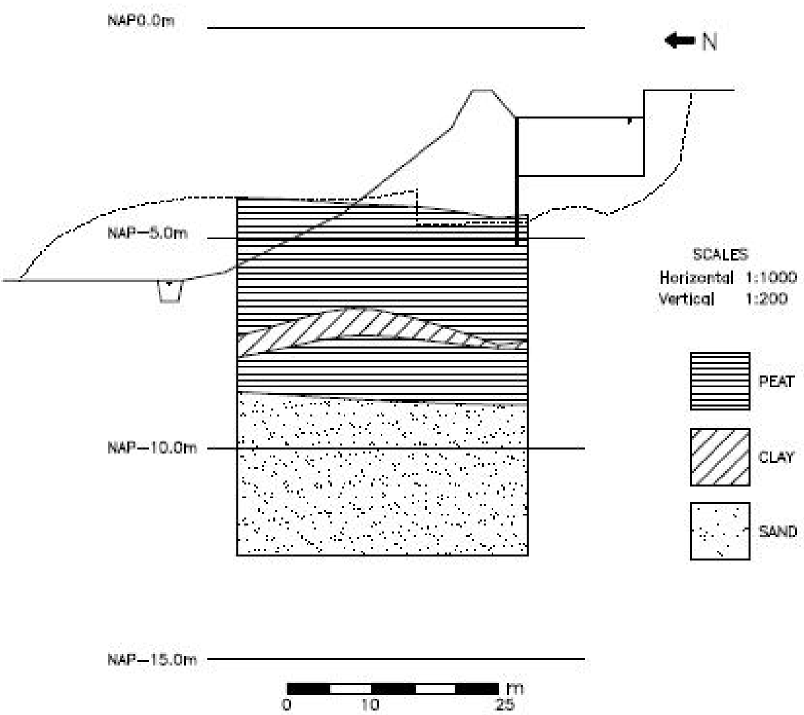

Figure 3.15: Cross section at breach 5 (far east side)

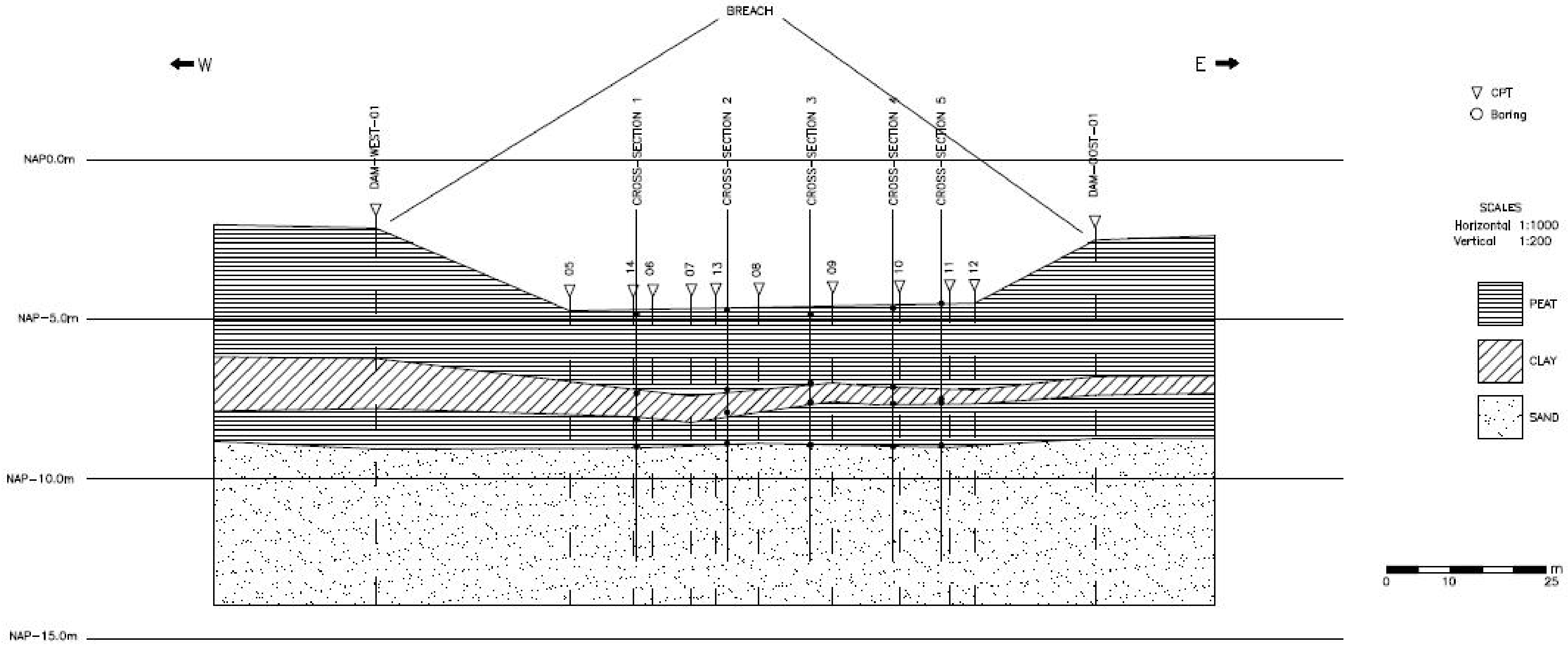

Figure 3.16: Geotechnical profile along breached crest of dike

A number of observations can be made in the above figures. The sand layer seems to be flat starting at about NAP -9.00 m. The clay layer seems to have a “bump” halfway the width of the cross-section in figures 3.12 to 3.15. It may be assumed that this “bump” was mainly caused by the failure, consistent with the situation before the breach involving a flat clay layer. The top of this clay layer seems to occur at around NAP -7.00m and the thickness of the clay layer is about 0.5 m. The top of the crest has, naturally, moved north and downwards during the breach as can be clearly seen in figures 3.11 to 3.13, a fact that is also supported by the photographs in paragraph 2.1. Also, on the crest of the dike there was a bicycle path made of asphalt. It is assumed that 0.5m of sand has been added on the top of the crest since it is not possible to construct the bicycle path directly on peat. With all this in mind the final geotechnical cross section that will be used for the analysis can be seen in figure 3.17 below. Also visible is the hydraulic head of the deep sand layer which has been measured by observation wells and found to be at NAP -6.00m (GeoDelft report 4, 2004 [38]).

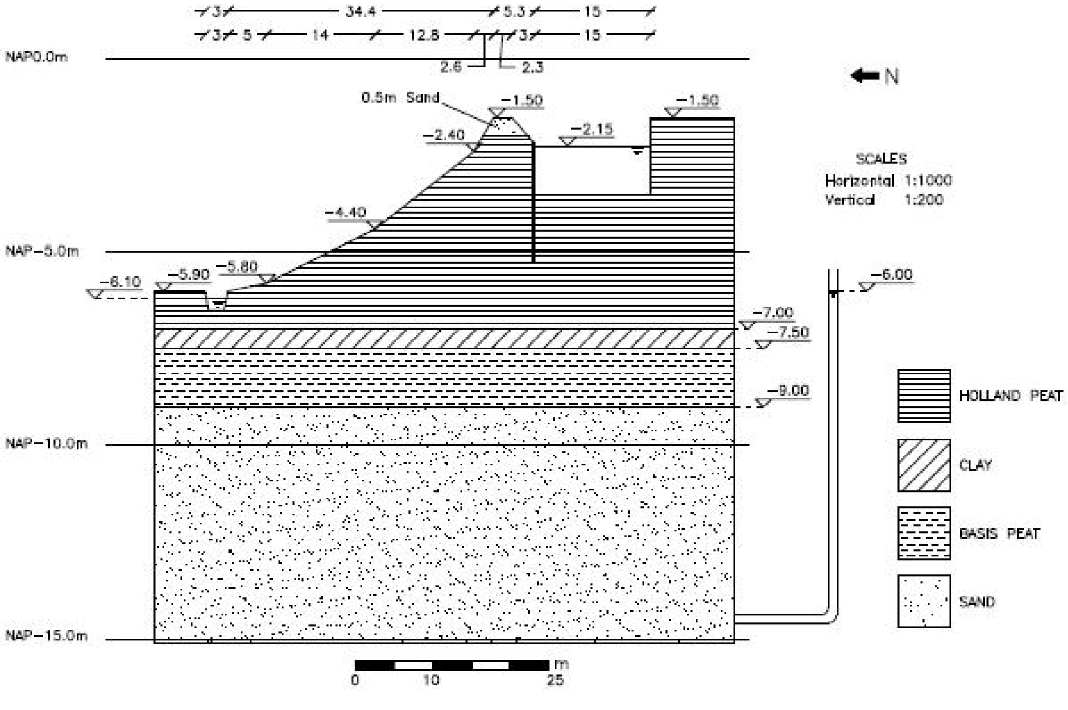

Figure 3.17: Estimated geotechnical cross section before breach

3.3 Laboratory testing

3.3.1 General

The soil properties for the different soil types are determined from the laboratory tests performed. As mentioned in the introduction of this chapter 3 types of laboratory tests have been conducted. These are namely the K_0-CRS test, the Triaxial test and the Simple Shear test. The stiffness parameters are determined mainly from the K_0-CRS test while the strength parameters are derived from the Triaxial and Simple Shear tests. In the peat dike 4 different soil types have been distinguished. These are namely Holland Peat, Clay, Basis Peat and Sand. Holland peat refers to the upper peat layer while basis peat to the lower peat layer between the deep sand layer and the thin clay layer (see figure 3.17 in previous paragraph). In the following sections the main characteristics of the various laboratory test data will be reviewed.

3.3.2 K_0-CRS test

The K_0-CRS (CRS= Constant Rate of Strain) test is a modified oedometer test where a cylindrical specimen is axially compressed at a small constant speed. For more details on the K_0-CRS test setup and procedure see also Appendix C. In total 15 K_0-CRS tests have been performed. The main results of the tests are one vertical stress σ versus axial strain ε graph (see figure 3.19). The apparatus used is also able to measure the horizontal stress thus providing the K_0 value ($K_0 = \frac{\sigma_h}{\sigma_v}$, ratio of horizontal to vertical stress). Consequently also the K_0 value versus axial strain ε graph is obtained (see figure 3.20). The graph in figure 3.19, of stress versus strain, is used in order to determine stiffness parameters.

It should be noted that in the applied K_0-CRS test the excess pore pressure was not measured. In fact it was assumed that initially an undrained response occurred gradually leading to a drained response due to consolidation of the excess pore pressure at the applied sufficiently low strain rate.

In one dimensional compression the logarithmic strain ε is given by formula 3.1 (Brinkgreve 2002 [30]):

$$\varepsilon = -A \cdot \ln(\frac{\sigma'}{\sigma'_0}) - B \cdot \ln(\frac{\sigma_{pc}}{\sigma_{p0}}) - C \cdot \ln(\frac{\tau_c + t'}{\tau_c}) \qquad (3.1)$$

where,

ε is the axial logarithmic strain (=$\ln\left[(h_0 + \Delta h)/h_0\right]$)

σ' is the axial effective stress

σ'_0 is the initial axial effective stress

σ_{pc} is the pre-consolidation pressure responding to end-of-consolidation state (at zero effective creep time $t' = 0$)

σ_{p0} is the pre-consolidation pressure responding to (initial) before-consolidation state

τ_c is the intrinsic time

t' is the effective creep time

A, B and C are model parameters directly measurable from a logarithmic effective stress versus strain graph as shown in figure 3.18 below.

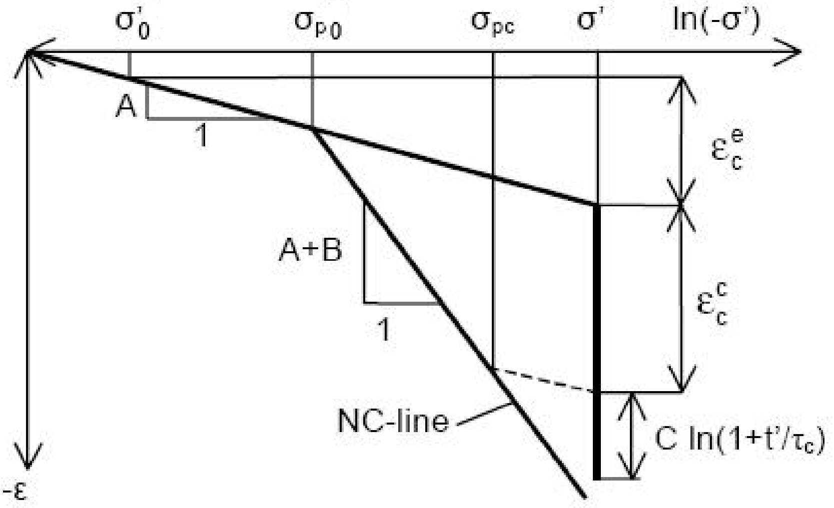

Figure 3.18: Illustration of A, B, C model parameters from a logarithmic stress-strain graph (Brinkgreve 2002 [30])

In figure 3.18 above,

ε_c^e refers to the elastic or reversible part of the strain,

ε_c^c refers to the inelastic or irreversible part of the strain (at zero effective creep time $t'=0$),

$C \cdot \ln(1+\frac{t'}{\tau_c})$ refers to the part of the strain due to creep(for $t' \geq 0$).

However, the results of the K$_0$-CRS tests performed by GeoDelft are expressed in terms of parameters κ*, λ* and μ*. κ* is the modified swelling index, λ* is the modified compression index and μ* is the modified creep index. These parameters are connected with parameters A, B and C in equation 3.1 through formulas 3.2 to 3.4 (Brinkgreve, 2002 [30]):

$$\kappa^* = \frac{3(1-v_{ur})}{(1+v_{ur})}A \qquad (3.2)$$

$$\lambda^* = \kappa^* + B \qquad (3.3)$$

$$\mu^* = C \qquad (3.4)$$

where,

v_{ur} is the Poisson's ratio for unloading-reloading

It should be noted that the resulting parameters κ*, λ* and μ* are the main stiffness parameters of the Plaxis Soft Soil Creep model that was used by GeoDelft for their analysis.

Below, in figures 3.19 till and including 3.24 (GeoDelft report 1, 2003 [35]) representative examples of the graphs resulting from a K_0-CRS test on Holland peat, Clay and Basis peat samples can be seen. Also measured and noted are the corresponding in-situ vertical effective pre-consolidation pressures Pg.

In these figures the corresponding parameters κ*, λ* and μ* fits have been omitted because in this report the Hardening Soil model will be applied, in which different stiffness parameters occur, to be illustrated in figures 4.5 and 4.6.

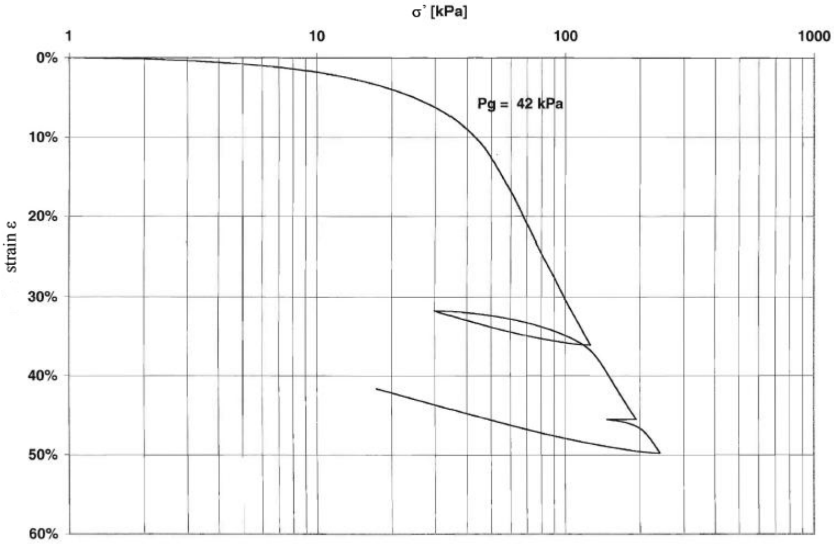

Figure 3.19: Logarithmic of vertical effective stress σ' vs vertical strain ε graph from K_0-CRS test on Holland peat (sample 114A, boring Oost-3-2BA, NAP-6.55m)

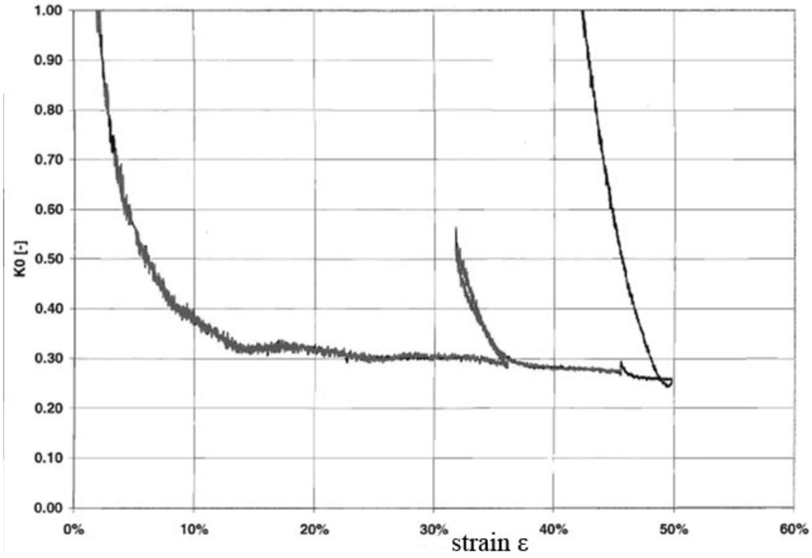

Figure 3.20: Ko value vs vertical strain ε graph from K_0-CRS test on Holland peat (sample 114A, boring Oost-3-2BA, NAP-6.55m)

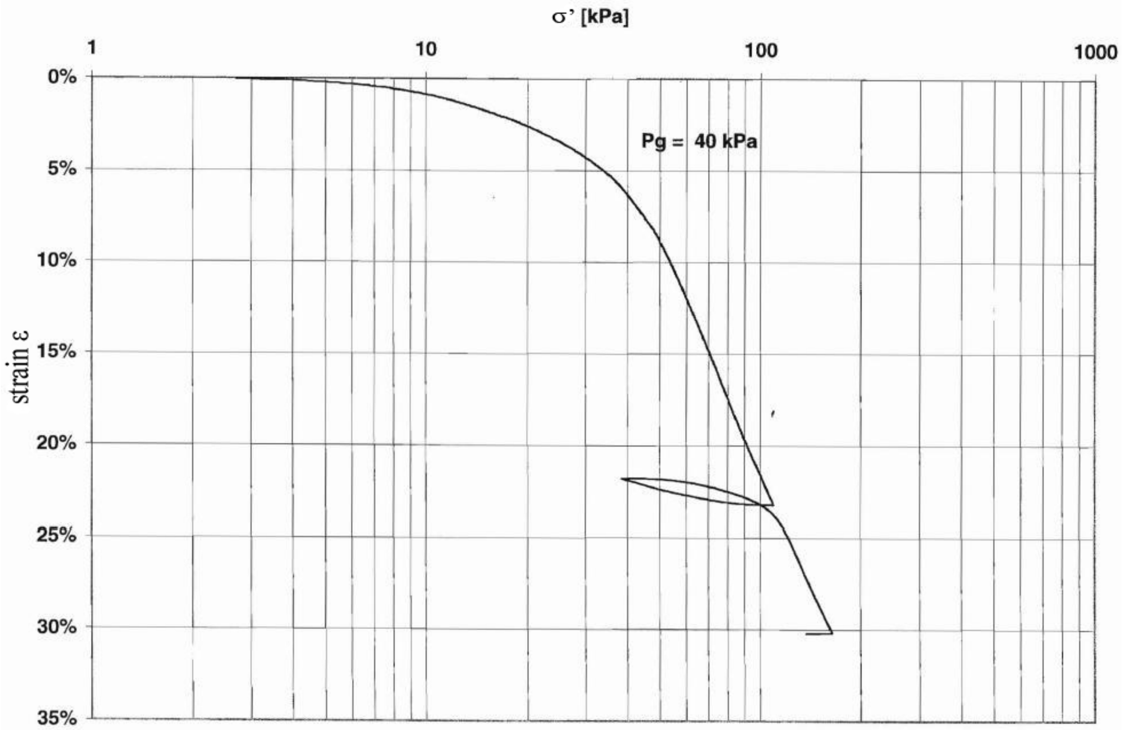

Figure 3.21: Logarithmic of vertical effective stress σ' vs vertical strain ε graph from K_0-CRS test on Clay (sample 114B, boring Oost-3-2BA, NAP-7.05m)

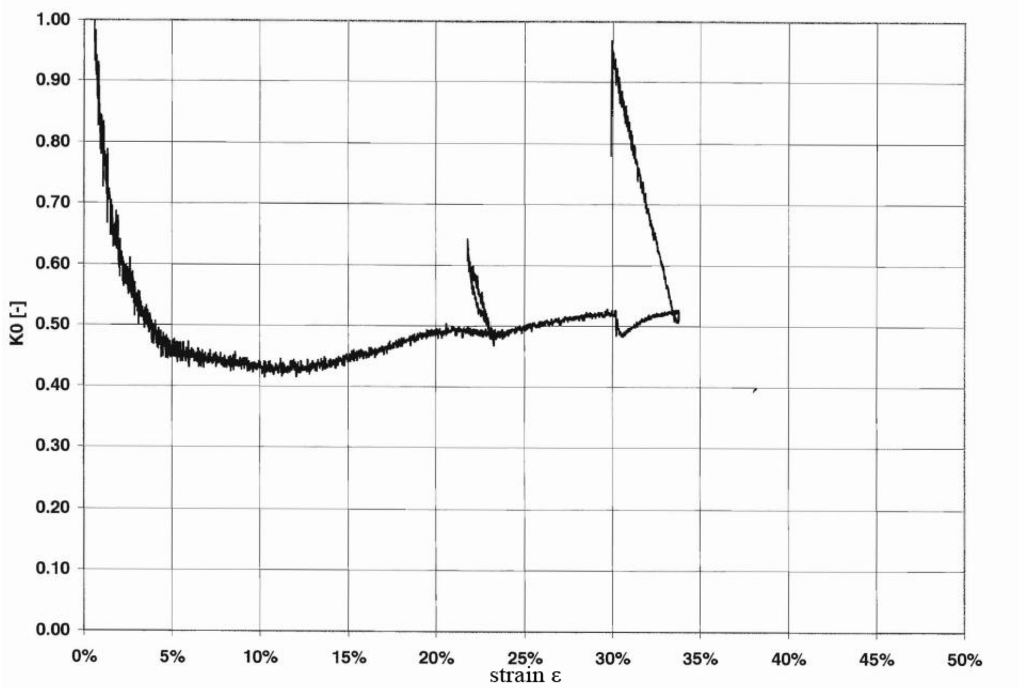

Figure 3.22: Ko value vs vertical strain ε graph from K_0-CRS test on Clay (sample 114B, boring Oost-3-2BA, NAP-7.05m)

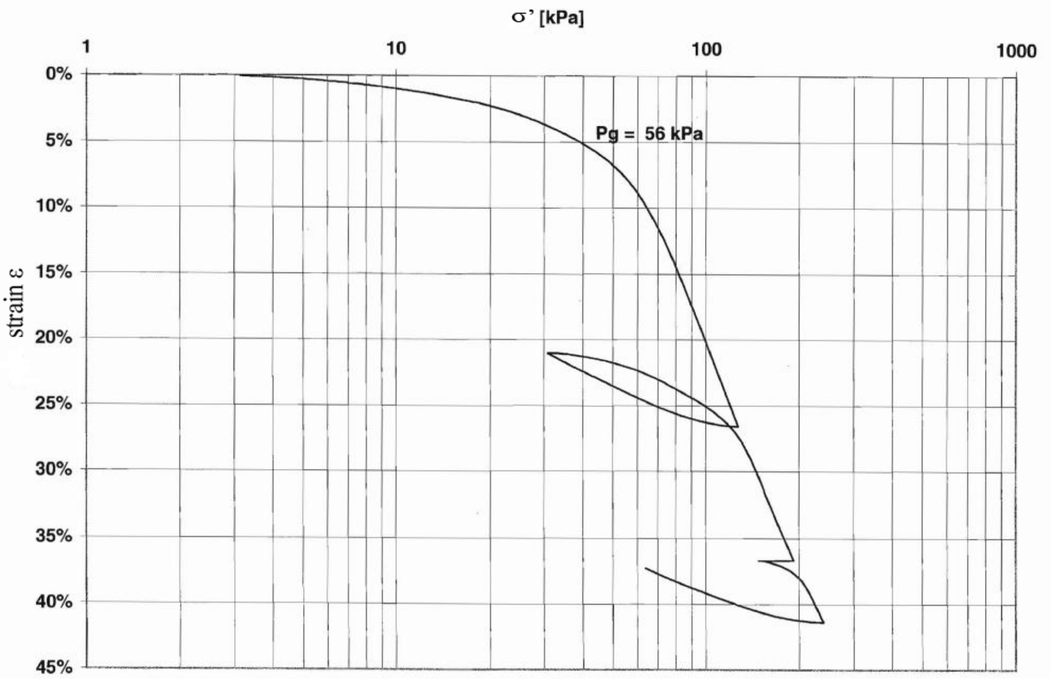

Figure 3.23: Logarithmic of vertical effective stress σ' vs vertical strain ε graph from K_0-CRS test on Basis peat (sample 115, boring Oost-3-2BA, NAP-8.20m)

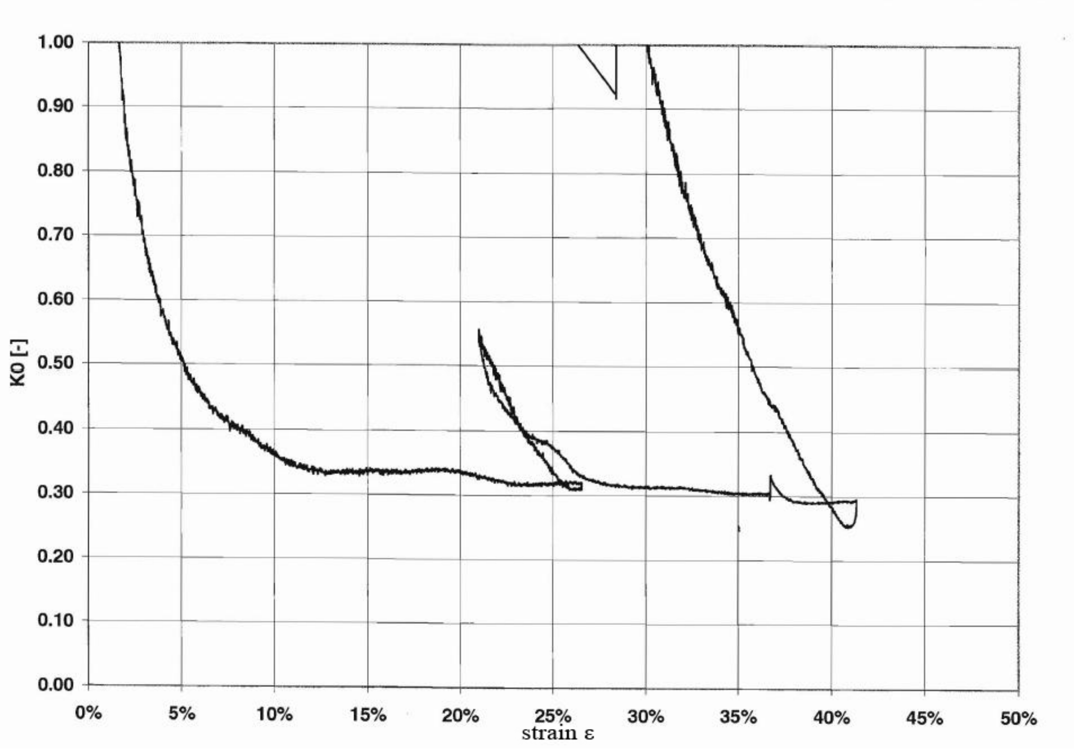

Figure 3.24: Ko value vs vertical strain ε graph from K_0-CRS test on Basis peat (sample 114A, boring Oost-3-2BA, NAP-8.20m)

3.3.3 Triaxial test

The triaxial test provides information about strength parameters, most important of which for the analysis are cohesion c and angle of internal friction φ. There were 12 tests performed in total according to norm NEN 5117. Clay and peat samples were tested in an undrained way while for sand samples drained testing was applied. For more details on the triaxial tests performed see also Appendix C.

From Holland peat only single samples were tested thus resulting in the determination of undrained strength c_u. The rest of the samples were tested in groups of 3 samples from the same point of origin and at different confining pressures in order to determine the cohesion c and angle of internal friction φ at an axial strain of 2%.

The experimental data for all soil types are depicted in the form of undrained effective stress paths, involving τ and s' according to the following definitions.

$\tau = \frac{\sigma'_1 - \sigma'_3}{2}$, is the maximum shear stress

$s' = \frac{\sigma'_1 + \sigma'_3}{2}$, is the mean effective stress measure

σ'_1, is the maximum effective principal stress

σ'_3, is the minimum effective principal stress

Furthermore the corresponding undrained peak strength circles are illustrated in terms of normal effective stress σ' and the shear stress τ.

Figure 3.25 shows an example of the stress path of an undrained triaxial compression test on a single sample of Holland peat and figure 3.26 the corresponding Mohr circle of the effective stress at the undrained peak strength c_u. In figures 3.27 till and including 3.30 (GeoDelft report 1, 2003 [35]) the resulting graphs on 3 Clay and 3 Basis peat samples and the determination of the strength parameters from the drawing of the Mohr circles and the failure envelope can be seen.

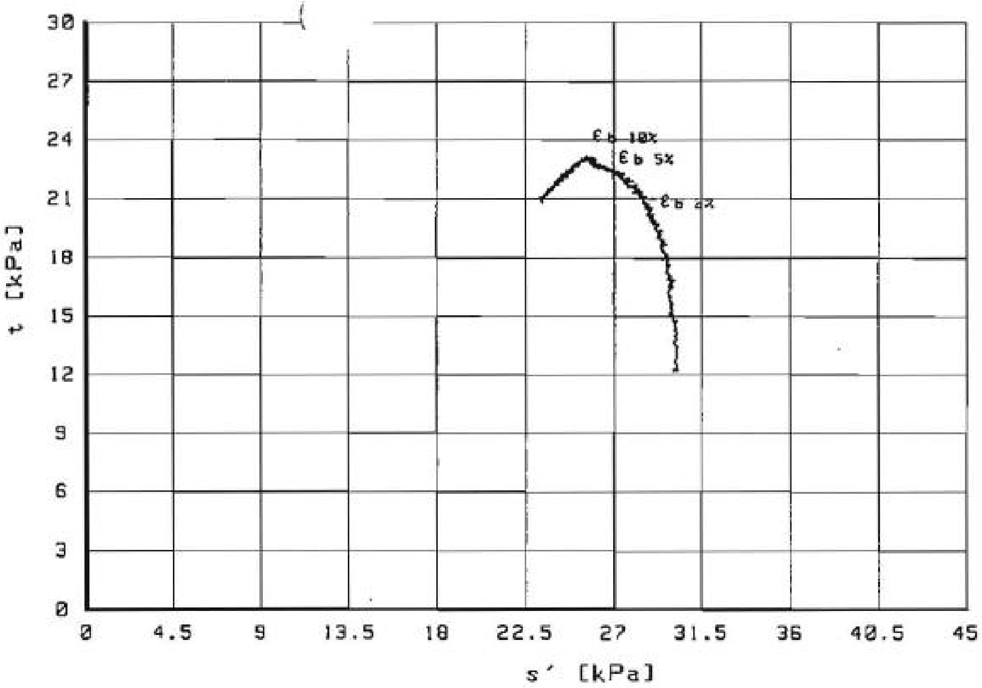

Figure 3.25: Undrained effective stress path from undrained triaxial test on Holland peat (sample 114A, boring Oost-3-2BA, NAP-6.75m)

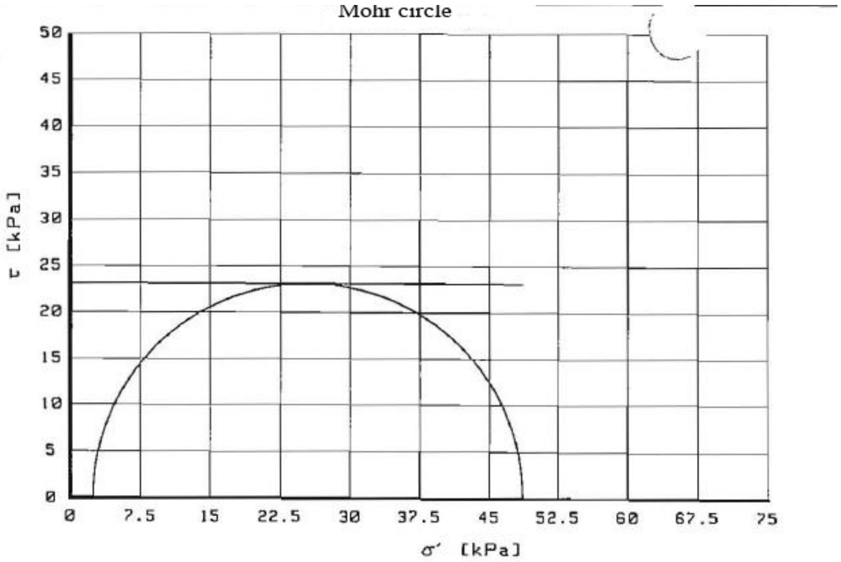

Mohr circle	
Cu value [kN/m2]	23.12

Figure 3.26: Mohr circle and undrained failure envelope from undrained triaxial test on Holland peat (sample 114A, boring Oost-3-2BA, NAP-6.75m)

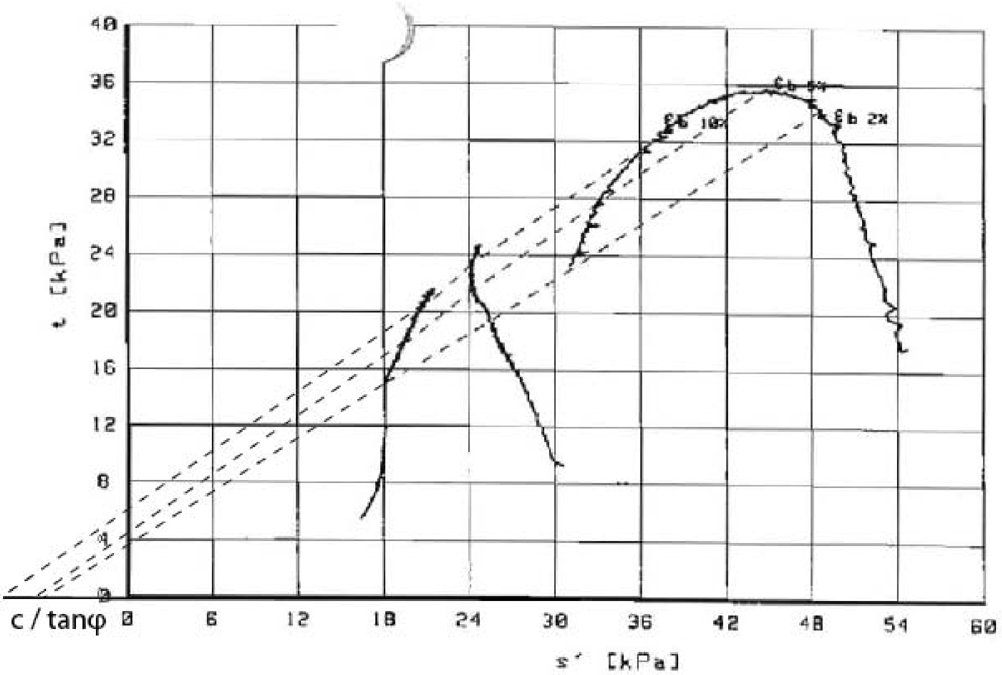

Figure 3.27: Undrained effective stress paths from undrained triaxial tests on Clay (samples 136/143/151, borings Oost-3-1BA/BB/BC, NAP-7.15m)

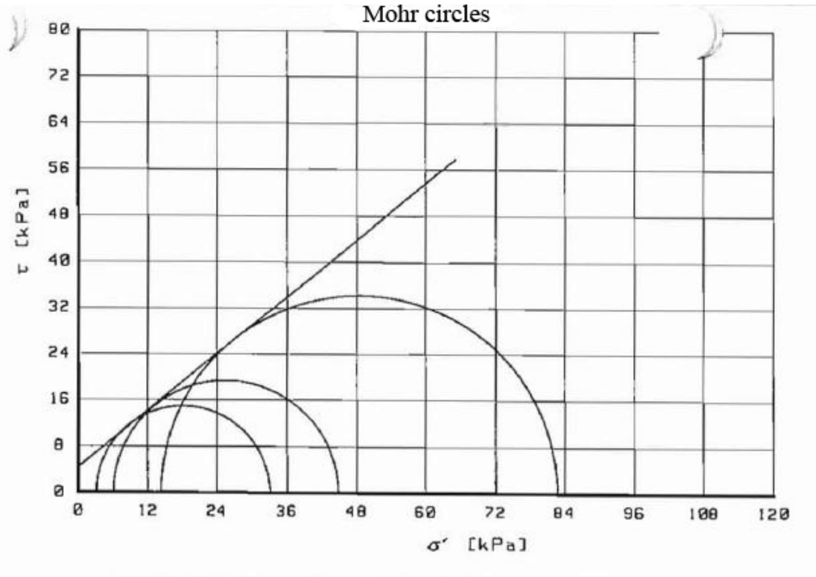

Mohr circles at 2% strain		
ø'	[°]	39.38
c'	[kN/m2]	4.39

Figure 3.28: Mohr circles and effective failure envelope at 2% axial strain from 3 undrained triaxial tests on Clay (samples 136/143/151, borings Oost-3-1BA/BB/BC, NAP-7.15m)

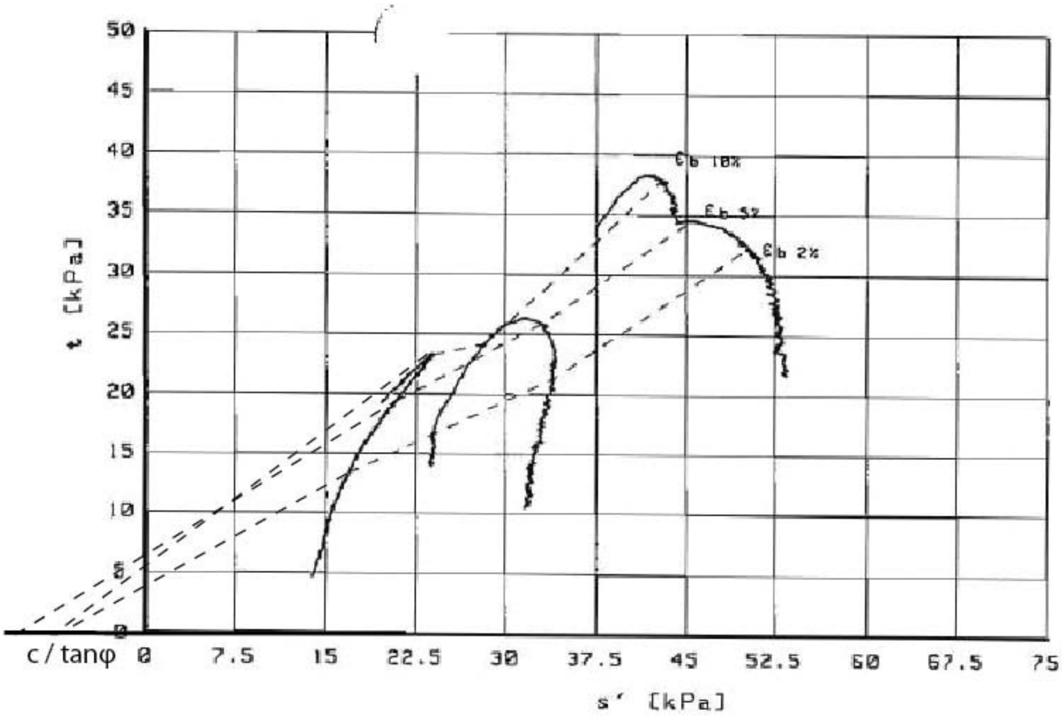

Figure 3.29: Undrained effective stress paths from undrained triaxial tests on Basis peat (samples 120/125/130, borings Oost-3-3BA/BB/BC, NAP-8.35m)

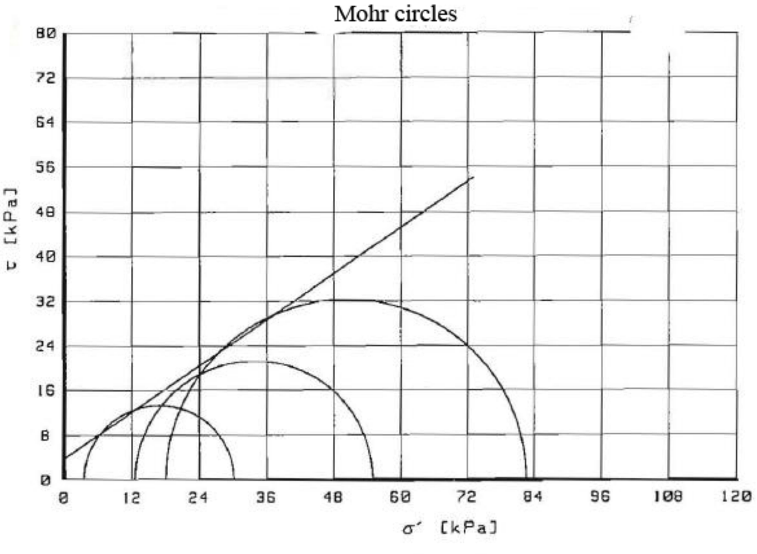

Mohr circles at 2% strain		
Ø'	[°]	34.56
c'	[kN/m2]	3.88

Figure 3.30: Mohr circles and effective failure envelope at 2% axial strain from 3 undrained triaxial tests on Basis peat (samples 120/125/130, borings Oost-3-3BA/BB/BC, NAP-8.35m)

3.3.4 Simple Shear test

In this test a flat sample is subjected to plane deformation with a linearly increasing shear strain with time, while the developing shear stress is measured. Figure 3.31 shows the deformation as seen from the side. The sides of the sample are supported by a reinforced membrane, so that the sample diameter remains more or less constant. For more details on the test setup see also Appendix C. From a total of 13 samples that were tested 3 of them were tested at constant vertical pressure while the rest 10 were tested at constant height.

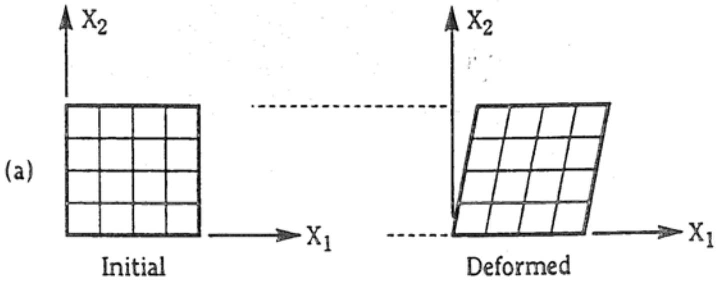

Figure 3.31: Enforced deformation for simple shear testing (GeoDelft report 1, 2003 [35])

Figures 3.32, 3.33 and 3.34 (GeoDelft report 1, 2003 [35]) below show examples of SS test results on Holland peat, Clay and Basis peat respectively. It is noted that only the shear stress τ and normal effective stress σ_v' on a horizontal shear plate have been measured. The dashed line represents the fitted failure envelope of maximum mobilized friction according to:

$$\tau_c = c_{ss} + \sigma_v' \cdot \tan \varphi_{ss}$$

In which cohesion c_{ss} and friction angle φ_{ss} are the peak strength parameters for simple shear.

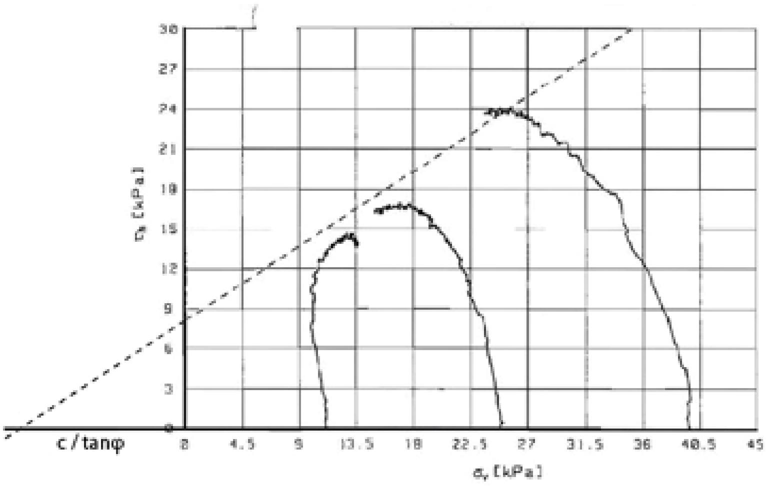

Soil type		HOLLAND PEAT
Phi	[graad]	31.91
C	[kN/m2]	8.18

Figure 3.32: Effective stress path and failure envelope from SS test on Holland peat for zero vertical strain (sample 108A, boring Oost-3-2BB, NAP-6.70m)

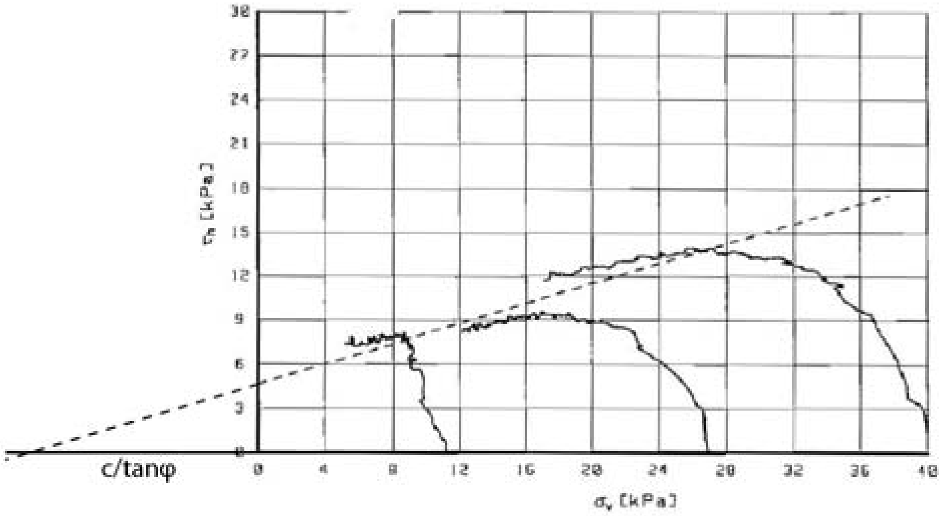

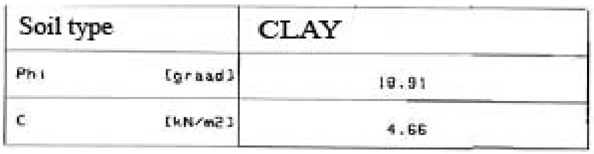

Soil type		CLAY
Phi	[graad]	18.91
C	[kN/m2]	4.66

Figure 3.33: Effective stress path and failure envelope from SS test on Clay for zero vertical strain (sample 108B, boring Oost-3-2BB, NAP-7.05m)

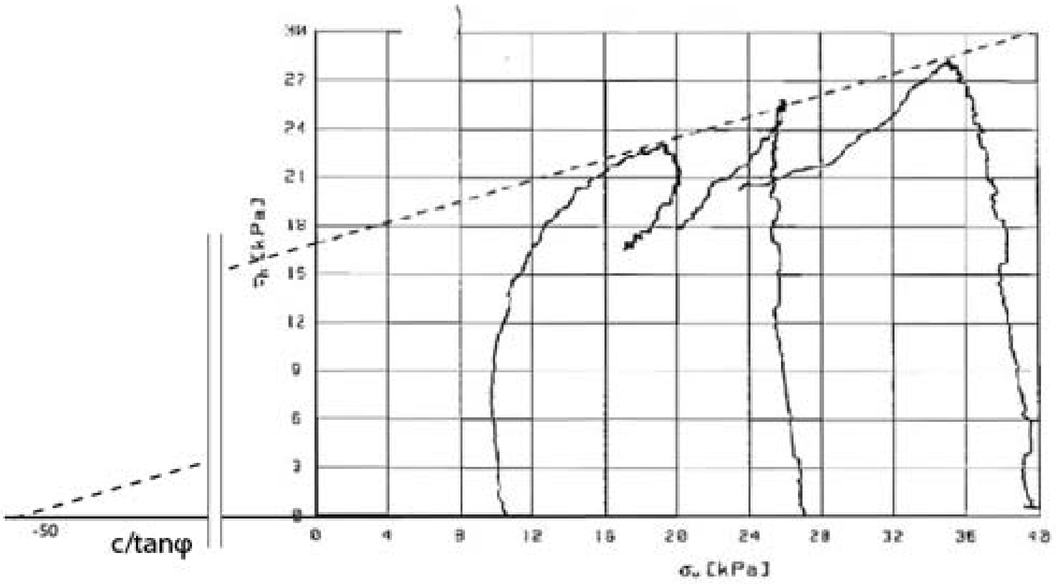

Soil type		BASIS PEAT
Phi	[graad]	18.26
C	[kN/m2]	16.90

Figure 3.34: Stress path and failure envelope from SS test on Basis peat for zero vertical strain (sample 109, boring Oost-3-2BB, NAP-8.20m)

3.3.5 Overview of test results

In the tables 3.1 to 3.4 below the accumulative test results of the laboratory tests performed by GeoDelft can be found (the data are taken from GeoDelft report 1, 2003 [35]). In tables 3.5 to 3.8 the calculated averages and standard deviations of the soil properties for each of the 4 soil types have been collected.

								Laboratory testing				Field data
Boring	Depth (m-ground)	Depth (m-NAP)	Sample number	Soil type	Test	γ_{sat} (kN/m^3)	water content (%)	κ*	λ*	μ*	K_0	cone resistance (MPa)
Oost-2-01	3.90	-5.90	36	Peat (Holland)	Ko-CRS	10.7	336	0.032	0.176	0.012	0.35	0.50
Oost-3-1BA	4.40	-6.15	135	Peat (Holland)	Ko-CRS	10.0	653	0.061	0.202	0.016	0.32	0.50
Oost-3-2BA	3.10	-6.55	114A	Peat (Holland)	Ko-CRS	9.8	638	0.057	0.271	0.019	0.30	0.38
Oost-3-3BA	1.70	-6.55	128A	Peat (Holland)	Ko-CRS	9.4	454	0.052	0.171	0.014	0.25	0.64

Boring	Depth (m-ground)	Depth (m-NAP)	Sample number	Soil type	Test	γ_{sat} (kN/m^3)	water content (%)	c_u (kPa)	cone resistance (MPa)
West-1-03	0.50	-6.05	9	Peat (Holland)	Triaxial	9.5	502	15.40	0.50
West-1-03	1.45	-7.00	10a	Peat (Holland)	Triaxial	9.9	771	13.20	0.22
West-1-03	1.95	-7.50	10b	Peat (Holland)	Triaxial	9.6	906	9.85	0.24
Oost-3-2BA	3.30	-6.75	114A	Peat (Holland)	Triaxial	9.3	685	23.12	0.41

Boring	Depth (m-ground)	Depth (m-NAP)	Sample number	Soil type	Test	γ_{sat} (kN/m^3)	water content (%)	c (kPa)	φ (^{0})	cone resistance (MPa)
West-1-03	0.90	-6.45	9	Peat (Holland)	SS	9.9	738	4.70	20.3	0.24
West-1-03	2.10	-7.65	10	Peat (Holland)	SS	9.9	887	0.94	26.9	0.33
Oost-3-2BB	3.25	-6.70	108A	Peat (Holland)	SS	9.7	673	8.10	31.9	0.48

Table 3.1: Holland peat accumulated test results

								Laboratory testing				Field data
Boring	Depth (m-ground)	Depth (m-NAP)	Sample number	Soil type	Test	γ_{sat} (kN/m^3)	water content (%)	κ*	λ*	μ*	K_0	cone resistance (MPa)
Oost-2-03	1.75	-7.10	44	Clay	Ko-CRS	11.5	207	0.027	0.212	0.015	0.38	0.97
Oost-3-1BA	5.25	-7.00	136	Clay	Ko-CRS	12.8	142	0.031	0.173	0.010	0.41	0.35
Oost-3-2BA	3.60	-7.05	114B	Clay	Ko-CRS	12.9	137	0.030	0.190	0.010	0.49	0.33
Oost-3-3BA	2.00	-6.85	128B	Clay	Ko-CRS	12.1	147	0.030	0.201	0.016	0.48	0.34

Boring	Depth (m-ground)	Depth (m-NAP)	Sample number	Soil type	Test	γ_{sat} (kN/m^3)	water content (%)	c (kPa)	φ (^{0})	c_u (kPa)	cone resistance (MPa)
West-1-03	2.70	-8.25	11	Clay	Triaxial	12.0	177	-	-	9.43	0.36
Oost-3-2BA	3.30	-6.75	114	Clay	Triaxial	11.3	196	4.10	41.0		0.5
Oost-3-2BB	3.80	-7.25	108B	Clay	Triaxial	11.1	220	4.10	41.0		0.25
Oost-3-2BC	3.75	-7.25	102	Clay	Triaxial	11.2	261	4.10	41.0		0.25
Oost-3-1BA	1.75	-7.15	136	Clay	Triaxial	11.7	179	4.40	39.4		0.16
Oost-3-1BB	1.80	-7.15	143	Clay	Triaxial	12.8	151	4.40	39.4		0.16
Oost-3-1BC	1.80	-7.15	151	Clay	Triaxial	11.9	180	4.40	39.4		0.16

Boring	Depth (m-ground)	Depth (m-NAP)	Sample number	Soil type	Test	γ_{sat} (kN/m^3)	water content (%)	c (kPa)	φ (^{0})	cone resistance (MPa)
West-1-03	2.50	-8.05	11	Clay	SS	12.1	268	9.11	8.8	0.29
Oost-3-1BB	5.55	-7.30	143	Clay	SS	11.6	204	8.30	16.0	0.18
Oost-3-2BB	3.60	-7.05	108B	Clay	SS	12.5	200	4.66	18.9	0.20
Oost-3-3BC	2.10	-6.95	119	Clay	SS	11.6	274	8.96	26.4	0.25
Oost-3-4BB	0.50	-6.15	159	Clay	SS	11.0	211	8.45	21.1	0.17

Table 3.2: Clay accumulated test results

								Laboratory testing				Field data
Boring	Depth (m-ground)	Depth (m-NAP)	Sample number	Soil type	Test	γ_{sat} (kN/m^3)	water content (%)	κ*	λ*	μ*	K_0	cone resistance (MPa)
Oost-2-03	2.75	-8.10	45	Peat (Basis)	Ko-CRS	10.1	624	0.040	0.266	0.016	0.25	0.38
Oost-2-04	1.65	-7.35	48	Peat (Basis)	Ko-CRS	9.5	379	0.028	0.241	0.019	0.38	0.16
Oost-3-1BA	6.80	-8.55	138	Peat (Basis)	Ko-CRS	10.3	450	0.089	0.228	0.011	0.18	0.54
Oost-3-2BA	4.75	-8.20	115	Peat (Basis)	Ko-CRS	10.2	455	0.073	0.264	0.024	0.32	0.45
Oost-3-3BA	3.80	-8.65	130	Peat (Basis)	Ko-CRS	10.2	511	0.067	0.242	0.014	0.34	0.16

Boring	Depth (m-ground)	Depth (m-NAP)	Sample number	Soil type	Test	γ_{sat} (kN/m^3)	water content (%)	c (kPa)	φ (^{0})	cone resistance (MPa)
Oost-3-2BA	4.95	-8.40	115	Peat (Basis)	Triaxial	10.0	515	8.10	36.2	0.51
Oost-3-2BB	4.95	-8.40	109	Peat (Basis)	Triaxial	10.0	500	8.10	36.2	0.47
Oost-3-2BC	4.80	-8.30	103	Peat (Basis)	Triaxial	10.1	479	8.10	36.2	0.52
Oost-3-3BA	3.60	-8.45	130	Peat (Basis)	Triaxial	10.2	570	3.80	34.5	0.19
Oost-3-3BB	3.60	-8.35	125	Peat (Basis)	Triaxial	10.0	573	3.80	34.5	0.15
Oost-3-3BC	3.50	-8.35	120	Peat (Basis)	Triaxial	10.1	566	3.80	34.5	0.15

Boring	Depth (m-ground)	Depth (m-NAP)	Sample number	Soil type	Test	γ_{sat} (kN/m^3)	water content (%)	c (kPa)	φ (^{0})	cone resistance (MPa)
Oost-3-2BB	4.75	-8.20	109	Peat (Basis)	SS	10.4	452	16.90	18.3	0.41
Oost-3-3BB	3.30	-8.05	125	Peat (Basis)	SS	10.5	549	5.50	24.1	0.13
Oost-3-4BB	2.35	-8.00	161	Peat (Basis)	SS	10.4	706	6.70	17.7	0.09

Table 3.3: Basis peat accumulated test results

								Laboratory testing				Field data
Boring	Depth (m-ground)	Depth (m-NAP)	Sample number	Soil type	Test	γ_{sat} (kN/m^3)	water content (%)	κ*	λ*	μ*	K_0	cone resistance (MPa)
Oost-3-3BA	4.80	9.65	131	Sand	Ko-CRS	19.7	24.3	0.0038	0.0067	-	0.40	-
Oost-3-4BC	3.70	9.40	167	Sand	Ko-CRS	18.1	19.2	0.0048	0.0065	-	0.48	2.14

Boring	Depth (m-ground)	Depth (m-NAP)	Sample number	Soil type	Test	γ_{sat} (kN/m^3)	water content (%)	c (kPa)	φ (^{0})	cone resistance (MPa)
Oost-3-1BA	7.30	-9.05	145A	Sand	Triaxial	20.8	19.4	0.85	42.9	2.33
Oost-3-1BB	7.55	-9.30	145B	Sand	Triaxial	20.1	21.4	0.85	42.9	5.95
Oost-3-1BC	7.40	-9.20	153	Sand	Triaxial	20.3	18.3	0.85	42.9	5.85
Oost-3-3BA	4.60	-9.45	131	Sand	Triaxial	20.4	19.7	0	42.3	-
Oost-3-3BB	5.05	-9.80	126	Sand	Triaxial	19.5	26.3	0	42.3	-
Oost-3-3BC	4.45	-9.30	121	Sand	Triaxial	20.7	20.6	0	42.3	-
Oost-3-4BA	3.20	-8.85	158	Sand	Triaxial	20.4	19.3	0	44.5	1.28
Oost-3-4BB	3.25	-8.90	167a	Sand	Triaxial	20.2	20.4	0	44.5	1.59
Oost-3-4BC	3.50	-9.20	167b	Sand	Triaxial	20.7	18.0	0	44.5	1.71

Boring	Depth (m-ground)	Depth (m-NAP)	Sample number	Soil type	Test	γ_{sat} (kN/m^3)	water content (%)	c (kPa)	φ (^{0})	cone resistance (MPa)
Oost-3-2BB	5.65	-9.10	110	Sand	SS	20.6	17.8	18.30	28.6	-
Oost-3-3BB	4.80	-9.55	126	Sand	SS	19.6	23.9	-14.73	33.7	-

Table 3.4: Sand accumulated test results

HOLLAND PEAT	Average	Standard deviation
γ_{sat} (kN/m^3)	9.8	0.35
water content (%)	658	166
κ^*	0.051	0.011
λ^*	0.205	0.040
μ^*	0.0153	0.003
Ko	0.305	0.04
c_u (kPa) Triaxial	15.4	7.55
c (kPa) SS	4.58	3.22
φ (^{0}) SS	26.4	12.10

Table 3.5: Statistical soil parameters of Holland peat

CLAY	Average	Standard deviation
γ_{sat} (kN/m^3)	11.9	0.6
water content (%)	197	42
κ^*	0.03	0.0015
λ^*	0.194	0.014
μ^*	0.013	0.003
Ko	0.44	0.046
c_u (kPa) Triaxial	9.43	0
c (kPa) Triaxial	4.25	1.49
φ (^{0}) Triaxial	40.2	14.10
c (kPa) SS	8.15	1.65
φ (^{0}) SS	18.2	5.82

Table 3.6: Statistical soil parameters of Clay

BASIS PEAT	Average	Standard deviation
γ_{sat} (kN/m^3)	10.1	0.23
water content (%)	523	80
κ^*	0.059	0.022
λ^*	0.248	0.015
μ^*	0.017	0.004
Ko	0.294	0.071
c (kPa) Triaxial	5.95	2.15
φ (^{0}) Triaxial	35.4	0.85
c (kPa) SS	9.70	5.11
φ (^{0}) SS	20.0	2.89

Table 3.7: Statistical soil parameters of Basis peat

SAND	Average	Standard deviation
γ_{sat} (kN/m^3)	20.1	0.69
water content (%)	20.7	2.53
κ^*	0.0043	0.0005
λ^*	0.0066	0.0001
μ^*	-	-
Ko	0.23	0.04
c (kPa) Triaxial	0.28	0.39
φ (^{0}) Triaxial	43.2	13.00
c (kPa) SS	1.79	16.52
φ (^{0}) SS	31.2	2.55

Table 3.8: Statistical soil parameters of Sand

4 Plaxis Input Parameter Determination

4.1 General

In this chapter the determination of the soil parameters that will be used for the analysis by Plaxis can be found. The material model chosen for the analysis is the Hardening Soil model of Plaxis. The main reason for this choice is that the previous analyses performed by GeoDelft were done with the Soft Soil Creep model and the research intends to have an alternative approach involving the Hardening Soil model, which is an advanced material model quite fit for modeling soft soils as well. Furthermore, time dependent behavior like creep, which is the main advantage of the Soft Soil Creep model, is not of much importance in this case since the focus of the research is on the failure of a peat dike and not on its settlement. Paragraph 4.2 below contains some general information about the Hardening Soil model as described in Plaxis Manual (Brinkgreve, 2002 [30]).

4.2 Hardening Soil model

The Hardening Soil model is an advanced material model that can be used to simulate the behavior of both soft and stiff soils. Similar to the hyperbolic Duncan & Chang model it also takes into account the decreasing stiffness and plastic strains that occur due to primary deviatoric loading. However, it is more realistic than the hyperbolic model for two reasons. First reason is that dilatancy is included in the Hardening Soil model and second is that a yield cap is introduced as well. Also, the yield surface is not fixed in stress space but is able to expand because of plastic straining. There are two types of hardening, shear hardening and compression hardening. Shear hardening is connected with deviatoric loading and compression hardening is connected with compression and isotropic loading. The Hardening Soil model uses three different moduli in order to simulate the soil behavior. These are namely the E_{50}^{ref} for plastic straining due to deviatoric loading, the E_{oed}^{ref} for plastic straining due to primary compression and the E_{ur}^{ref} for elastic unloading and reloading. Furthermore, stress dependency of the stiffness is taken into account through a power law using the parameter m since the above stiffnesses correspond to a specific reference minor principal stress p^{ref} (which can be defined by the user). The set of basic input parameters necessary for the Hardening Soil model is completed with the strength parameters connected with failure following the Mohr-Coulomb failure criterion. These parameters are namely cohesion c and angle of internal friction φ. The angle of dilatancy ψ enables to calculate the plastic volumetric strain during deviatoric loading.

One of the basic features of the Hardening Soil model is the stress dependency of the soil stiffness. The input stiffness parameters that are corresponding to a reference minor principal stress p^{ref} (defined by the user) are transformed to the actual confining pressure according to the following rules (Brinkgreve, 2002 [30]):

$$E_{50} = E_{50}^{ref} \cdot \left(\frac{c \cdot \cos\phi - \sigma_3' \cdot \sin\phi}{c \cdot \cos\phi + p^{ref} \cdot \sin\phi}\right)^m \tag{4.1}$$

$$E_{ur} = E_{ur}^{ref} \cdot \left(\frac{c \cdot \cos\phi - \sigma_3' \cdot \sin\phi}{c \cdot \cos\phi + p^{ref} \cdot \sin\phi}\right)^m \tag{4.2}$$

$$E_{oed} = E_{oed}^{ref} \cdot \left(\frac{c \cdot \cos\phi - \sigma_1' \cdot \sin\phi}{c \cdot \cos\phi + p^{ref} \cdot \sin\phi}\right)^m \tag{4.3}$$

In figure 4.1 (Brinkgreve, 2002 [30]) a deviatoric stress versus strain graph can be seen where E_{50} and E_{ur} are graphically defined and in figure 4.2 (Brinkgreve, 2002 [30]) there is a graphical definition of E_{oed} from a stress versus strain graph of an oedometer test.

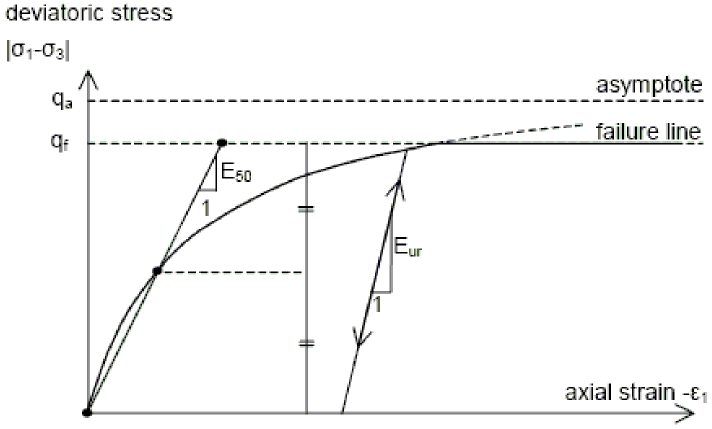

Figure 4.1: Hyperbolic stress-strain relation in primary loading for a standard drained triaxial test

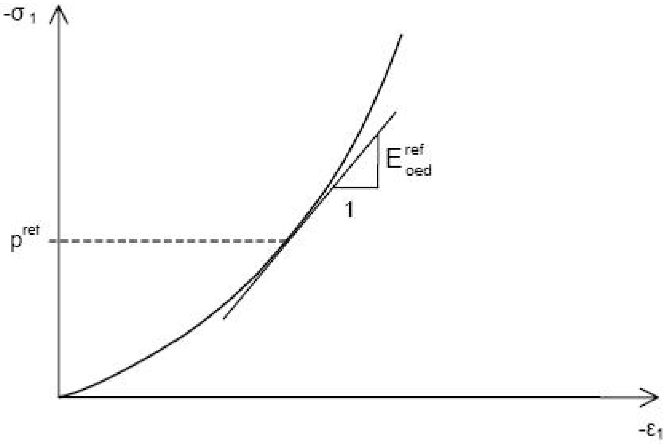

Figure 4.2: Definition of E_{oed} in stress vs strain graph from oedometer test

The shear strain yield function is (equations 4.4 till and including 4.17 by Brinkgreve, 2002 [30]):

$$f = \overline{f} - \gamma_p , \tag{4.4}$$

where $\overline{f}$ is a function of stress and γ_p is a function of plastic strains defined as:

$$\overline{f} = \frac{2}{E_i}\frac{q}{1-q/q_a} - \frac{2q}{E_{ur}} \text{ and} \tag{4.5}$$

$$\gamma_p = -(2\varepsilon_1^p - \varepsilon_v^p) \approx -2\varepsilon_1^p , \tag{4.6}$$

where E_i is the initial stiffness, equal to

$$E_i = \frac{2E_{50}}{2-R_f} \tag{4.7}$$

R_f is the failure ratio, equal to

$$R_f = \frac{q_f}{q_a} \tag{4.8}$$

q_f is the ultimate deviatoric stress, equal to

$$q_f = (c \cdot \cot\phi - \sigma_3 ')\frac{2\sin\phi}{1-\sin\phi} \tag{4.9}$$

q_a is the asymptotic value of the shear strength.

The shear hardening flow rule (i.e. the relationship between rates of plastic strain) has the linear form:

$$\varepsilon_v^p = \sin\psi_m \cdot \gamma^p \text{, where} \tag{4.10}$$

ε_v^p is the plastic volumetric strain and

ψ_m is the mobilised dilatancy angle with values:

For $\sin\phi_m < 3/4$ $\quad\psi_m = 0$

For $\sin\phi_m \geq 3/4$ and $\psi > 0$ $\quad\sin\psi_m = \max(\frac{\sin\phi_m - \sin\phi_{cv}}{1-\sin\phi_m \cdot \sin\phi_{cv}}, 0)$ (4.11)

For $\sin\phi_m \geq 3/4$ and $\psi \leq 0$ $\quad\psi_m = \psi$

If $\phi = 0$ $\quad\psi_m = 0$

Where ϕ_{cv} is the critical state friction angle and ϕ_m is the mobilised friction angle:

$$\sin\phi_m = \frac{\sigma_1' - \sigma_3'}{\sigma_1' + \sigma_3' - 2 \cdot c \cdot \cot\phi} \tag{4.12}$$

At failure, when the mobilised friction angle equals the failure angle ϕ, it is found that:

$$\sin\phi_{cv} = \frac{\sin\phi - \sin\psi}{1 - \sin\phi \cdot \sin\psi} \tag{4.13}$$

Besides the yield surfaces according to Mohr-Coulomb the Hardening Soil model also incorporates a cap yield surface. The definition of this cap yield surface is:

$f^c = \frac{\tilde{q}^2}{a^2} + p^2 - p_p^2$, where (4.14)

$p = -(\sigma_1 + \sigma_2 + \sigma_3)/3$ is the isotropic pressure (4.15)

$\tilde{q} = \sigma_1 + (\delta - 1) \cdot \sigma_2 + \delta \cdot \sigma_3$, with $\delta = \frac{3 + \sin\varphi}{3 - \sin\varphi}$, is a measure for deviatoric stress (4.16)

p_p is the isotropic pre-consolidation stress that is related to volumetric cap strain ε_v^{pc} by the law:

$$\varepsilon_v^{pc} = \frac{\beta}{1-m} \left(\frac{p_p}{p^{ref}}\right)^{1-m} \tag{4.17}$$

a and β are both cap parameters that are related to K_0^{nc} and E_{oed}^{ref} respectively

The resulting yield surfaces can be seen in principal stress space in figure 4.3.

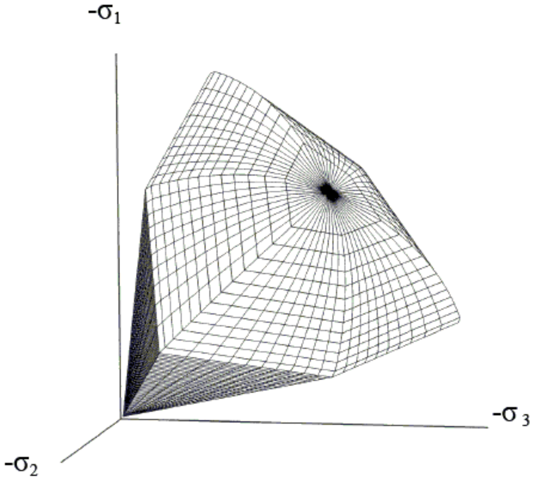

Figure 4.3: Total yield contour of the Hardening Soil model in principal stress space for cohesionless soil (Brinkgreve, 2002 [30])

4.3 Stiffness parameters determination

The main strength parameters, i.e. cohesion and angle of internal friction can be taken directly from the Triaxial tests or the SS tests performed and inserted in Plaxis. But the stiffness parameters measured from the K_0-CRS tests (κ*, λ* and μ*) are used in the Soft Soil Creep model, as mentioned before, and are not suitable for the Hardening Soil model that is used in this analysis. Therefore, a simulation of the K_0-CRS test in Plaxis is performed using the Hardening Soil model in order to find appropriate values for the stiffness parameters of the Hardening Soil model for the 2 different peat layers. The stiffness parameters are the 3 different moduli of elasticity (E_{50}^{ref}, E_{oed}^{ref}, E_{ur}^{ref}) and the power m.

4.3.1 Simulation scheme

The K_0-CRS test is similar to an oedometer test but with a constant speed of deformation applied to the sample. The test is simulated with a 2D plane strain model. The dimensions of the sample are the same as the real test, 60 mm wide and 20 mm high. The boundary conditions are:

- no horizontal displacement allowed to the sides
- no horizontal or vertical displacement allowed to the bottom
- prescribed vertical displacement of the top according to the test procedure
- water flow allowed only from the top

In figure 3.22 below the model with its boundary conditions can be seen.

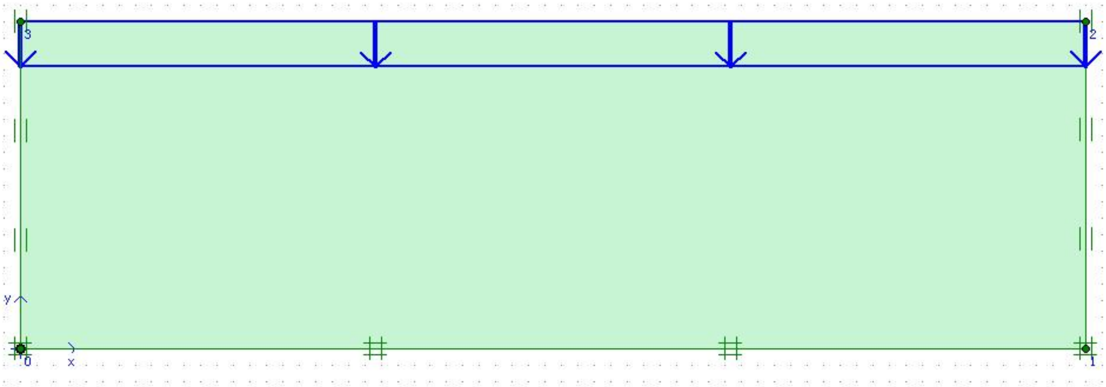

Figure 4.4: K_0-CRS test simulation model in Plaxis

The test procedure that was followed for the K_0-CRS test by GeoDelft was:

- Loading up to 130 kPa
- Unloading down to 30 kPa
- Reloading up to 200 kPa
- Relaxation (decrease of pressure at constant height) during 16 hours
- Loading up to 250 kPa
- Unloading and dismantling

The process that was actually followed in Plaxis in order to simulate the test was the following:

- The displacement was read from the stress-strain curve produced from the K_0-CRS test.
- This displacement was inserted as a prescribed displacement in Plaxis.
- With trial and error the values of the stiffness parameters were changed in order for the simulated results (i.e. stress) to be as close as possible to the real test data.

For the initial values of the stiffness parameters the following correlation formulas were used (Brinkgreve, 2002 [30]):

$$E_{oed}^{ref} = \frac{p^{ref}}{\lambda *} \tag{4.18}$$

$$E_{ur}^{ref} = \frac{3p^{ref}(1-2v_{ur})}{\kappa *} \tag{4.19}$$

where,

p^{ref} is the reference minor principal stress (the value applied is 100 kPa)

v_{ur} is the Poisson's ratio for unloading reloading (the value applied is 0.2)

It should be noted that the values coming from the above equations 3.8 and 3.9 were used as a starting point only and were therefore in many cases altered to a large degree in order to achieve a better fit of the curves.

4.3.2 Holland peat stiffness parameters

For the upper Holland peat layer the K_0-CRS test on sample 114A (see also figures 3.19 and 3.20) from boring Oost-3-2BA at a depth of NAP -6.55m was chosen to be simulated. For the strength parameters the SS test results are preferred to the triaxial ones because they are considered more conservative for soft soils like peat. As can be seen in table 3.1 from the 3 SS tests performed on Holland peat only one comes from a sample east of the breach and close to the sample location as modeled. The strength parameters were therefore taken from the results of a SS test on sample 108A from boring Oost-3-2BB at a depth of NAP -6.70m as collected in table 3.1. Below in figure 4.5 the fitting of the Plaxis simulation curve, in red, can be seen alongside with the original curve resulting from the test ,in black (GeoDelft report 1, 2003 [35]). The values of the stiffness parameters that led to this curve and will be used for the main analysis can be found in table 4.1.

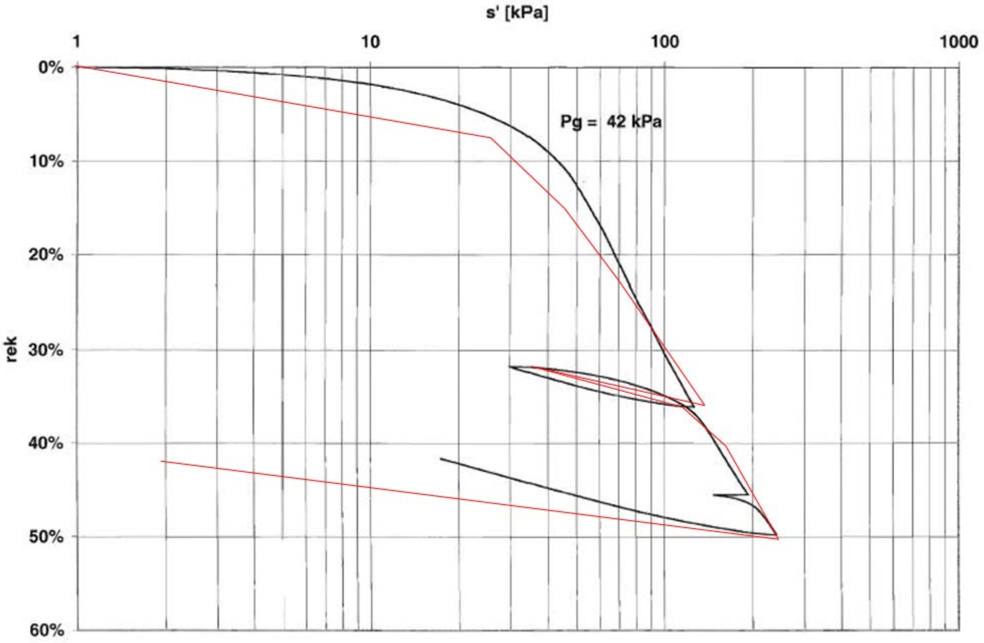

Figure 4.5: Simulation of Holland peat Ko-CRS test (red: Plaxis simulation)

Soil type	Holland peat
E_{50}^{ref} (kN/m^2)	2200
E_{oed}^{ref} (kN/m^2)	425
E_{ur}^{ref} (kN/m^2)	5000
m	1.0

Table 4.1: Holland peat stiffness parameters

4.3.3 Basis peat stiffness parameters

The K_0-CRS test on Basis peat sample 115 was chosen to be modeled. It is a representative sample as can be seen in table 3.3. It is taken from boring Oost-3-2BA at a depth of NAP -8.20m. The strength parameters were taken from a sample tested on SS in the vicinity of the first one, sample 109 from boring Oost-3-2BB at a depth of NAP -8.20m. In figure 4.6 the fitting of the Plaxis simulation curve, in red, can be seen alongside with the original curve resulting from the test ,in black (GeoDelft report 1, 2003 [35]). In table 4.2 the values of the stiffness parameters that led to this curve and will be used for the main analysis can be found.

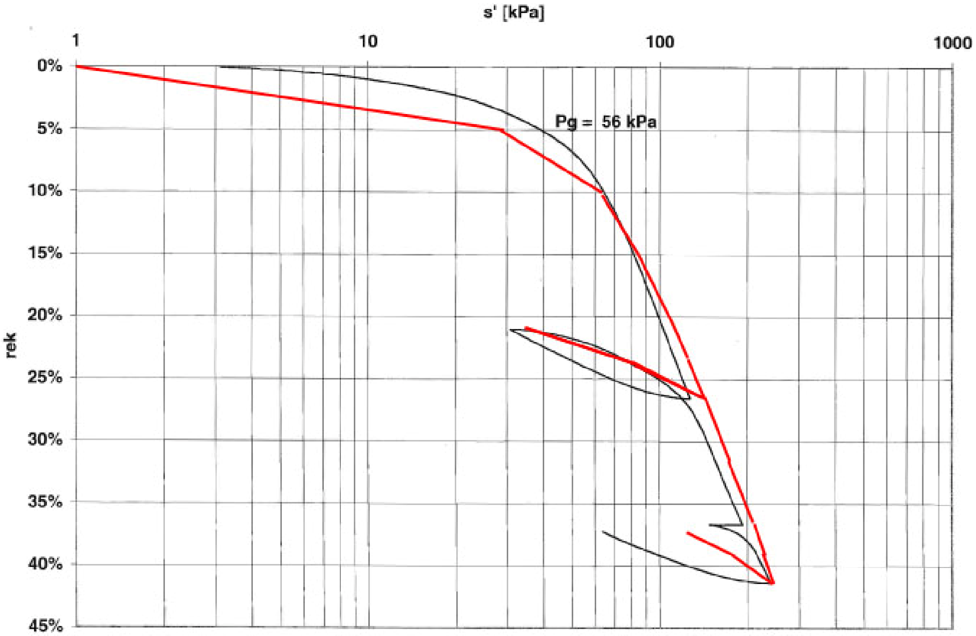

Figure 4.6: Simulation of Basis peat Ko-CRS test (red: Plaxis simulation)

Soil type	Basis peat
E_{50}^{ref} (kN/m^2)	250
E_{oed}^{ref} (kN/m^2)	340
E_{ur}^{ref} (kN/m^2)	1800
m	1.0

Table 4.2: Basis peat stiffness parameters

4.4 Determination of unsaturated weight γ_{unsat} of Holland peat

Because 2003 had a very warm and dry summer for the Netherlands it was natural to expect the groundwater table to drop. Therefore for the upper part of the soil, which consists of the Holland peat layer, it is necessary to know as accurately as possible the value of the unsaturated volumetric weight since its impact on the stability can be significant. Noting that the measurements by GeoDelft were taken after the failure, the applied unsaturated self weight was calculated based on the calculated distribution of the degree of saturation above the groundwater table at the end of a period with severe drought. The definitions of saturated gravimetric water content w_{sat} and unsaturated volumetric weight γ_{unsat} read:

$$w_{sat} = \frac{n \cdot \rho^w}{(1-n) \cdot \rho^m} \tag{4.20}$$

$$\gamma_{unsat} = \left[(1-n) \cdot \rho^m + S^w \cdot n \cdot \rho^w\right] \cdot g \tag{4.21}$$

where,

n is the porosity

ρ^w is the density of water (approximately equal to 1000 Kg/m^3)

ρ^m is the density of the soil material

S^w is the degree of saturation (for fully saturated soil equal to 1)

g is the acceleration of gravity (approximately equal to 9.81 m/s^2)

From equations 4.20 and 4.21 follows for saturated soils:

$$n = \frac{w_{sat} \cdot \gamma_{sat}}{\rho^w \cdot g \cdot (1 + w_{sat})} \tag{4.22}$$

$$\rho^m = \frac{\gamma_{sat} \cdot \rho^w}{\rho^w \cdot g \cdot (1 + w_{sat}) - \gamma_{sat} \cdot w_{sat}} \tag{4.23}$$

According to table 3.5 the average saturated weight $\gamma_{sat} \approx 9.8$ kN/m^3 and the gravitational water content $w_{sat} \approx 6.58$, while their standard deviations read $\sigma_{\gamma sat} \approx 0.35$ kN/m^3 and $\sigma_{wsat} \approx 1.66$. Substituting these values in (4.22) and (4.23) leads to the porosities n and material densities ρ^m as collected in the following table 4.3.

Parameters	mean − σ	mean	mean + σ
n	0.801	0.867	0.923
ρ^m $\left[\text{kg}/m^3\right]$	815	992	1180

Table 4.3: Estimated porosity n and material density ρ^m for both mean values and at mean plus / minus standard deviations of saturated self-weight $\sigma_{\gamma sat}$ and gravimetric water content σ_{wsat}

The unsaturated weight γ_{unsat} can be calculated from formula 4.21 with a value lower than 1 for the degree of saturation S^w since it is unsaturated soil (the weight of air is neglected). According to GeoDelft report 3 (2004, [37]) the mean degree of saturation of the upper part of the Holland peat layer, which was above the groundwater table, was measured after the failure at around 60%. Therefore different values of saturation are used and the corresponding magnitudes of the unsaturated self-weight γ_{unsat} for various degrees of saturation S^w are indicated in table 4.4 below.

S^w	γ_{unsat} in kN/m^3		
	mean $-\ \sigma$	mean	mean $+\ \sigma$
0.8	7.88	8.10	8.34
0.7	7.09	7.25	7.43
0.6	6.31	6.40	6.53
0.5	5.52	5.55	5.62

Table 4.4: Unsaturated self-weight of Holland peat for various degrees of saturation S^w for both mean values and at mean plus / minus standard deviations of porosity σ_n and material density $\sigma_{\rho m}$

For the other soil layers the precise determination of the unsaturated volumetric weight is not of importance since they are below the groundwater table in all cases.

4.5 Plaxis input parameters

The applied parameter sets for the Hardening Soil model and the 4 soil types occurring in the peat dike as illustrated in figure 3.17 have been collected in table 4.4. Both the mean value and the estimated standard deviation (as percentage) are indicated. Several parameters have been measured by GeoDelft and have been indicated in tables 3.5 to 3.8, while this author determined the parameters as indicated in tables 4.1 and 4.2. Also the equation numbers in which the parameters have been defined are indicated.

The remaining parameters have been estimated based on information from the literature. These parameters are the permeability in both directions k_x and k_y, dilation angle ψ, Poisson’s ratio for unloading-reloading v_{ur} and reference pressure $p_{ref.}$

For the permeability k_x and k_y assumed values are used. Dilation angle ψ is considered equal to zero. Poisson’s ratio for unloading-reloading v_{ur} is considered to be 0.2 and the reference pressure p_{ref} equal to 100 kPa.

Name				**Holland Peat**		**Clay**		**Basis Peat**		**Sand**	
	Equation number	Units	Reference table	Average	s.d.(%)	Average	s.d.(%)	Average	s.d.(%)	Average	s.d.(%)
Plaxis parameter type				Undrained		Undrained		Undrained		Drained	
γ_{unsat}	4.22	kN/m^3	§ 4.4	6.4	-	9	-	7.5	-	17	-
γ_{sat}	4.21	kN/m^3	3.5, 3.6, 3.7, 3.8	9.8	3.6	11.9	5.0	10.1	2.3	20.1	3.4
k_x	-	m/day	-	0.04	-	0.0005	-	0.004	-	5	-
k_y	-	m/day	-	0.04	-	0.0005	-	0.004	-	5	-
E_{50}^{ref}	4.1	kN/m^2	4.1, 4.2	2200	-	2000	-	250	-	12000	-
E_{oed}^{ref}	4.3	kN/m^2	4.1, 4.2	425	-	600	-	340	-	8000	-
E_{ur}^{ref}	4.2	kN/m^2	4.1, 4.2	5000	-	6000	-	1800	-	50000	-
Power m	4.1	-	4.1, 4.2	1	-	1	-	1	-	0.5	-
c_{ref}	4.9	kN/m^2	3.5, 3.6, 3.7, 3.8	4.58	70.3	8.15	20.2	9.7	52.7	1.79	922.9
φ	4.9	^{0}	3.5, 3.6, 3.7, 3.8	26.4	45.8	18.2	32.0	20	14.5	31.2	8.2
ψ	4.10	^{0}	-	0	-	0	-	0	-	0	-
ν_{ur}	-	-	-	0.2	-	0.2	-	0.2	-	0.2	-
p_{ref}	4.1	kN/m^2	-	100	-	100	-	100	-	100	-
K_0^{nc}	-	-	3.5, 3.6, 3.7, 3.8	0.305	13.1	0.440	10.5	0.294	24.1	0.230	17.4

Table 4.4: Plaxis input parameters

5 Plaxis and PlaxFlow Analyses

5.1 General information about Plaxis

Plaxis is a software package, based on the finite element method, which performs deformation and stability analyses in geotechnical engineering. It features a graphic environment both for input and output. This way it is relatively easy to create a finite element model, run the calculations and inspect the results. Plaxis has a two-dimensional version where the real situation is modeled as a cross-section either in plane strain or in axisymmetry. The user interface consists of four subprograms. These subprograms are namely Input, Calculations, Output and Curves.

As input the program requires a number of parameters. First the geometry of the geo-hydrological mechanical structure and the loads have to be defined with the help of CAD procedures implemented in the graphic environment of the program. Then a mesh with user-defined coarseness can be automatically created with the push of a button. The mesh consists of either quadratic 6-node or 4th order 15-node triangular elements. Apart from the soil itself various structural elements that are used in reality are also included in Plaxis. Retaining walls and other slender structures can be modeled as “Plates”. The structural behavior of these elements is defined through their rigidity, stiffness and ultimate bending moment. In the case of an elastoplastic plate a plastic hinge may form if the ultimate bending moment is reached. Anchors and struts are modeled as spring elements with stiffness and maximum force defined by the user. There is a special option if prestressed anchors are to be used. Geogrids or geotextiles can also be modeled using Plaxis’ tension elements. When using these structural elements (plates, geogrids) it is usually needed to implement the so-called “Interface” elements. These elements are used to model the shearing zone between the soil and the structural elements mentioned above. In this way it is possible to define a different friction angle in this area than in the rest of the soil body as it is the case in reality.

Tunnels with circular or non-circular cross section can also be modeled in Plaxis with fully isoparametric elements for the curvature. Plates and interfaces are useful in the case of a tunnel as well, in order to simulate the tunnel lining and the interaction with the surrounding soil. Various methods of tunnel construction (e.g. bored tunnel, NATM tunnel) along with corresponding methods for calculation of deformations are at the user’s disposal.

The soil is a material with a non-linear, anisotropic and time-dependent behavior.

There are always uncertainties involved when dealing with soil and it is, naturally, of great importance for the quality of the analysis that the modeling of the soil itself is appropriate. Plaxis includes a number of material models, for the user to choose, that simulate the soil behavior with varying degrees of accuracy.

The most elementary model is Mohr-Coulomb. This is a linear-elastic-perfectly plastic model that is based on parameters widely used in engineering practice. Five parameters are necessary for this model, E and v for the stiffness, φ and c for plasticity and ψ as the angle of dilatancy. This model is the first approximation of the soil behavior. Each layer has its own average stiffness that remains constant.

Because of this, calculations are fast but not as reliable as when applying the more advanced models.

The Hardening Soil model is an advanced material model. The limit state is described in the same way as the Mohr-Coulomb model but the stiffness is defined with three different moduli of elasticity, the triaxial loading stiffness, E_{50}, the unloading-reloading stiffness, E_{ur} and the oedometer stiffness, E_{oed}. Furthermore stress dependency is taken into account meaning that the three input stiffnesses correspond to a specific reference stress (100 kPa) and that they change depending on the pressure. It can, however, not model cyclic loading or anisotropic behavior.

The Soft Soil Creep model is another advanced material model. It is more appropriate for modeling soft soils where creep is a dominant factor as well as for consolidation analyses.

Other material models included are the Hardening Soil with small-strain stiffness model (similar to Hardening Soil model but small-strain stiffness is incorporated here), the Soft Soil model (this is an old model superseded by the HS model and kept for user comfort), the Jointed Rock model (an anisotropic material model for modeling rock, it involves stratification and prescribed shear planes) and the Modified Cam-Clay model (for normally consolidated clays). There is even the possibility for user-defined material models to be used in the calculations. This special feature is mostly of interest to researchers.

It should be noted that the initial soil conditions play an essential role in most deformation problems no matter which material model is used. The initial stresses can be generated based on the K_0-value or in the case of non horizontal soil surface with the procedure of “gravity loading”.

Pore pressures can be easily created by defining a phreatic line. Different phreatic lines can be defined for different soil clusters in Plaxis. Also a more advanced groundwater flow calculation can be conducted in the case of a steady-flow or seepage situation using sub-program PlaxFlow. This flow calculation is naturally more time consuming than the calculation based on phreatic lines. Furthermore, soils can be distinguished between drained and undrained. In undrained soils no pore water flow is allowed and excess pore pressures are generated in the case of loading.

After everything has been defined in the Input program and pore water pressures (e.g. by means of PlaxFlow) as well as initial soil pressures are generated then the Plaxis Calculations program begins. Here a construction or excavation stage can be simulated by activation and deactivation of soil clusters, loads etc. This way the stresses and displacements due to the soil history are modeled in a realistic way.

Consolidation, a process observed in soils of low permeability, can also be calculated (in this version for saturated soil mechanics). For this reason the permeability coefficients of each soil type in two directions has to be defined. The time stepping procedure is done automatically by Plaxis so the analysis is more robust.

The “phi-c reduction” procedure included in the program can be used to determine the safety factor (the ratio of the available shear strength to the minimum shear strength required for equilibrium).

After the calculation has finished the results can be seen in the Output program. The deformed shape is drawn with a user-defined scale in order to make it understandable. Stresses, strains and displacements are presented in a graphic environment with color maps, vectors or contour plots. Output tables with all these values are created and can be exported. Plastic points can be drawn on the model to give a clearer view of where the failure begins or which part of the model is the weakest.

In the Curves program stress and strain paths, stress-strain diagrams and time-settlement curves are automatically created for any point of the model. These provide useful insight into the local soil behavior and allow a detailed analysis of the results of Plaxis.

5.2 General information about PlaxFlow

PlaxFlow is a finite element program capable of analysing two-dimensional transient saturated and unsaturated groundwater flow for geotechnical problems and hydrology. One of the most powerful features of PlaxFlow is that time-dependent conditions can be dealt with. These conditions can change following a linear or harmonic function or they can be directly defined through a table. It can work together with Plaxis 2D. Similar to Plaxis it features a graphical environment for input as well as output. The interface consists of two sub-programs, the Input where input of data and calculations are performed and the Output for viewing the results and generating curves.

The finite element model is created automatically once the geometry of the geo-hydrological mechanical structure is drawn with the help of CAD procedures as a two dimensional cross section of the problem. The mesh consists of 3-node elements which can be refined both globally and locally. In order to work with Plaxis also 6-node and 15-node elements can be used. There are a number of different elements in PlaxFlow that can be used in order to model the flow situation of the problem. Impermeable elements are simulated with the use of screens which, when activated, do not allow any water flow. Wells are used to model specific points in the model where there is either a discharge or inflow of a specific amount of water. With drains, points of zero pore pressure can be defined in the model. Groundwater heads can be created through water levels that can be drawn on the model. The boundaries of the model can be defined as closed flow boundaries meaning that there is no inflow or outflow from these boundaries. Also specific hydraulic heads or specific discharge/infiltration can be defined on the boundaries. Weather conditions can be simulated by prescribed infiltration and exfiltration of water at the boundary lines.

Naturally, similar to Plaxis, material sets are used for the parameters of each soil layer. The basic permeability model used to simulate unsaturated pore water flow behaviour is the well-known Van Genuchten model. There is also the alternative of using a more simplified linear version of Van Genuchten which is considered numerically more robust and is called approximate Van Genuchten model. Predefined data sets for both these models exist for each soil type and also the option to input the parameters manually. Also, calculation phases can be defined in the program when the conditions of the problem change in time such as a change in external water level, introduction of a well at a specific time, the building of an embankment etc. As soon as all the calculation phases are defined the calculation can begin.

The results of the calculation are displayed in the sub-program Output. Distributions of groundwater head, pore pressure, degree of saturation and Darcy flux can be graphically displayed on the model. Also, tables containing the above values can be automatically generated and exported to other programs. Graphs can also be drawn for specific cross-sections of the user's preference where heads, pressures and flow velocities can be seen. Curves that display the development of groundwater head, pore pressure, degree of saturation and Darcy flux with time can be created for any point of the model for further study of the groundwater flow procedure.

5.3 Geometry model

The two dimensional model was created in Plaxis Input program according to the layering of the subsoil resulting from the soil interpretation (mainly from in-situ tests like CPTs and boreholes, see also paragraph 3.2) and can be seen in figure 3.17. The geometry of the ground surface was taken from the report of GeoDelft since shortly after the breach remedial works were carried out in order to repair and strengthen the dike thus altering the ground surface.

The model in its initial form includes a flat surface at NAP -1.50m which is the dike crest level. This is done mainly in order to simulate more accurately the actual way the dike was created which was through excavation of peat and not by adding soil to construct the dike. Furthermore, with an initial flat surface the use of the "K_0 procedure" of Plaxis, in order to calculate the initial stresses in the soil, becomes possible. Otherwise, in the case of an uneven surface, initial stresses must be calculated with the more complicated procedure of "Gravity loading".

The model extends 20m beyond the important elements of the structure (i.e. the canal on the left and the small ditch on the right) on both sides. The entire canal is included in the model and not just the north shore, which was the one that failed first. This was because the south shore of the canal may also have an influence on the failure mechanism and not including it, although that would lead to a simpler model, could in the end give less reliable results. The dimensions of the model are therefore 100m wide and 23.5m deep. This size is considered adequate in order to include all the possible failure mechanisms so as not to cause any alteration to the calculation results.

The bottom boundary of the model is fixed into place with prescribed zero displacements in both directions (total fixity). The left and right boundaries are free to move vertically but not horizontally (horizontal fixity). All boundaries are set as impermeable by water except the right boundary of the sand layer because a constant hydraulic head of NAP -6.00m (with a standard deviation of about 4cm) is applied to that border. The geometry of the model in Plaxis can be seen in figure 5.1 below. For more details about the ground levels refer also to figure 3.17.

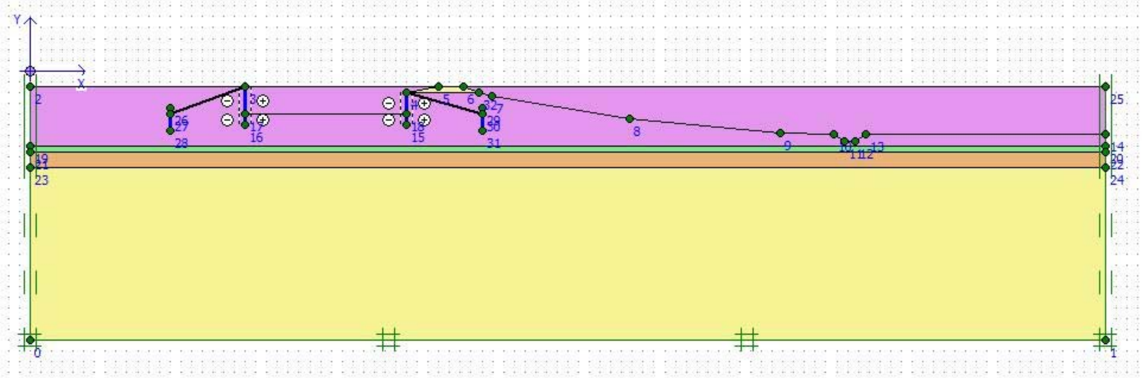

Figure 5.1: Geometry of model in Plaxis

Plaxis requires the formation of a mesh for the calculations to take place. This mesh is generated automatically by the program with the option to choose the coarseness of it. In this case the coarseness was set to very fine, the most detailed mesh option. The 3 top layers (Holland peat, Clay and Basis peat) were further refined by using the "Refine Cluster" button one time. In addition, the "Refine around point" option was used 3 times for 2 points, the bottom point of the right sheet pile and the left bottom point of the ditch, in order to have a more detailed mesh around these points since it is believed that the failure plane was probably in their vicinity. The mesh of the model created by Plaxis can be seen in figure 5.2 below.

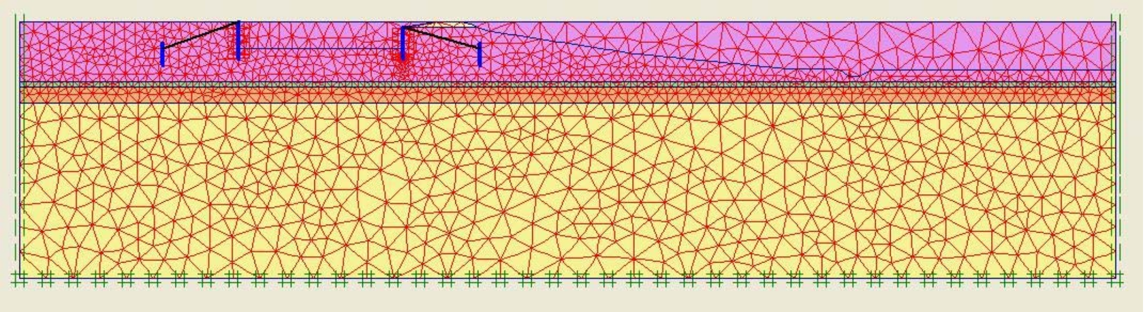

Figure 5.2: Generated mesh of Plaxis model

The sheet piling is a light construction made of wooden planks about 3.0m long as can be seen from photographs taken directly after the breach (Figure 2.6). The thickness is set to 5cm and the modulus of elasticity of wood to 10000MPa (Young's modulus article of Wikipedia). The anchor rods consist of steel with an assumed diameter of 2cm and a modulus of elasticity of 200000MPa (Young's modulus article of Wikipedia). Around the sheet piling an "Interface" has been applied in order to better simulate the soil-sheet pile interaction. The sheet piling is set as completely impermeable by water. A detail of the sheet piling can be seen in figure 5.3 below where also the numbering of nodes and elements is visible.

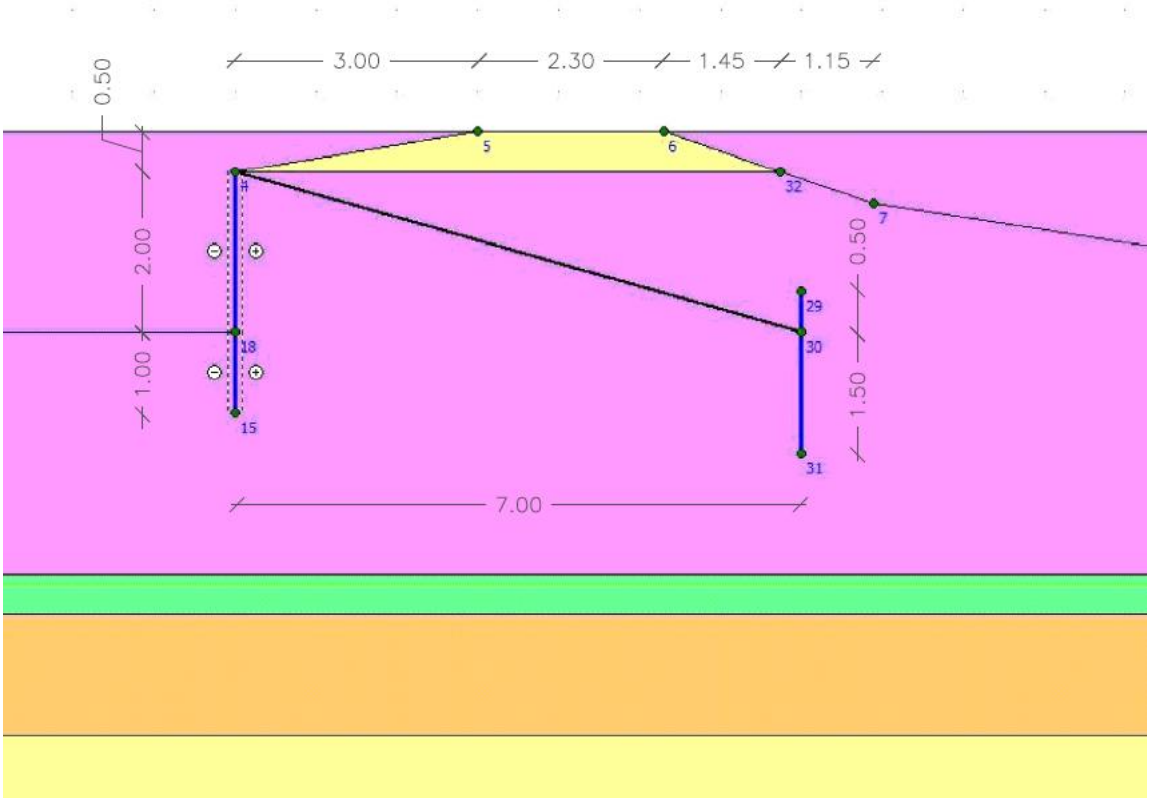

Figure 5.3: Detail of sheet piling and anchor

Before exiting the Input program to continue to the Calculations program initial stresses and pore pressures have to be calculated. The initial stresses are calculated according to the K_0 value of each soil type. For the pore pressure calculation a simple phreatic level calculation is conducted with a groundwater level of NAP -2.15m, the eventual water level of the canal, for the upper cohesive layers (Holland peat, clay and basis peat) and a phreatic level of NAP -6.00m (with a standard deviation of about 4cm) for the deeper sand layer. This hydraulic head has been measured by observation wells (GeoDelft report 4, 2004 [38]). After the geometry has been defined and the initial stresses have been calculated in the Plaxis Input program the next step is the Plaxis Calculations program. There the calculation phases are defined and the actual calculations are performed.

5.4 Calculation phases

In this paragraph a detailed example of the Plaxis and PlaxFlow calculation analysis is given. The procedure described here is followed for all the analyses that have been performed in this research.

PlaxFlow and Plaxis implement calculation phases which respond to the actual construction phases or changes that occurred in reality. The phases are calculated individually and serially, meaning that the calculation of each phase has as input the results of the previous phase plus the changes that are made by the user. In each phase first the water related aspects (flow field, hydraulic head, excess pore pressures etc.) are calculated by means of a PlaxFlow calculation (either steady-state or transient). It should be noted that in PlaxFlow for all the types of soil the data set used was the “Hypres” one and the permeability model used was the “Van Genuchten” model. The soil type was set as “organic” for Holland and basis peat, as “very fine” for clay and as “coarse” for sand. After the PlaxFlow calculation is successfully finished the Plaxis deformation and stability calculation takes place (taking into account the PlaxFlow calculation results). Both these calculations have to be successful for the next calculation phase to begin.

In the case of Wilnis, which is examined in this text, 3 calculation phases are defined. Phase 1 contains the final geometry of the dike with a uniform water level at NAP-2.15m. A PlaxFlow steady-state groundwater calculation is performed. In phase 2 the water level is dropped to the actual level before failure. The groundwater calculation is steady-state again. In phase 3 a transient PlaxFlow calculation is conducted in order to take into account the evaporation that happened due to the dry summer of 2003.

It should be noted that the first 2 calculation phases are performed in order to simulate the history of the soil and how the dike was created through excavation on the north side rather than by adding soil material on top of the existing ground surface. These changes happened many years ago when available construction methods were limited and therefore happened quite slowly. It is safe to assume that for that reason no excess pore pressures were developed in reality. This leads to the use of the “Ignore undrained behaviour” option of Plaxis for the first 2 phases. The use of this option does not allow any excess pore pressures to develop. So, the end of phase 2 is simulating the situation at the beginning of the summer of 2003 and for many years before that. Phase 3 simulates the effect of drought that eventually led to the failure of the dike.

Next the above mentioned 3 calculation phases are performed consecutively, each phase starting with a PlaxFlow groundwater flow analysis and followed by the corresponding Plaxis deformation and stability analysis. The calculations are performed while using the average parameters as collected in table 4.4.

● Phase 1 – Removing the soil

In this phase clusters of soil are removed in order to lead to the actual geometry of the situation with the canal and the dike. Also the sheet piling and anchors are activated. The groundwater levels remain the same as in the initial phase thus leading to almost the entire model being submerged under water (see Figure 5.4 below). In the right hand boundary of the deep sand layer a constant hydraulic head of NAP-6.00m is applied. A steady state groundwater flow calculation is performed in this phase.

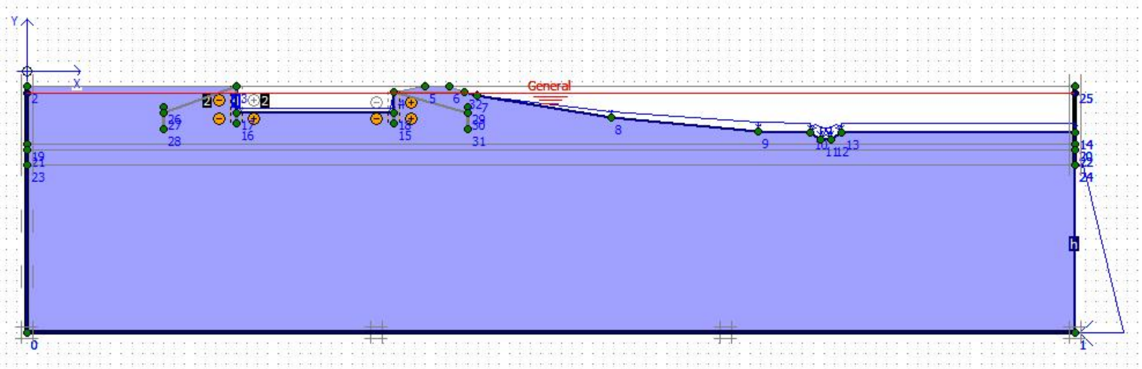

Figure 5.4: Input for phase 1 (red line shows the water level at NAP-2.15m)

Phase 1a – Steady state PlaxFlow groundwater flow analysis

The results of the steady-state PlaxFlow analysis can be seen in figures 5.5 to 5.7 below. Figure 5.5 shows the flow field, figure 5.6 the groundwater head and figure 5.7 the degree of saturation in the dike.

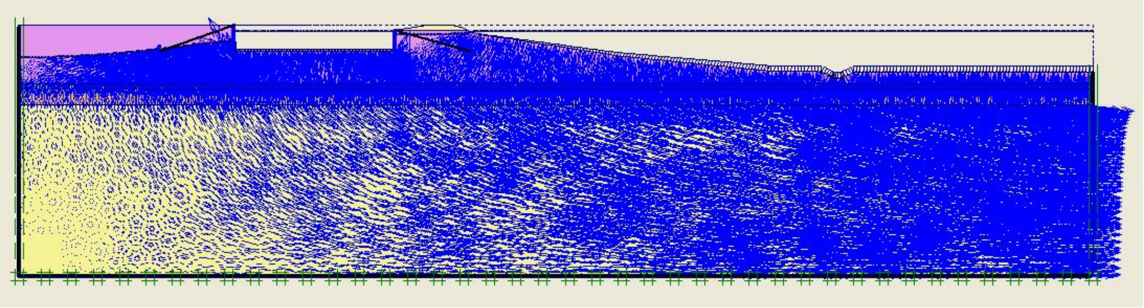

Figure 5.5: Flow field of phase 1

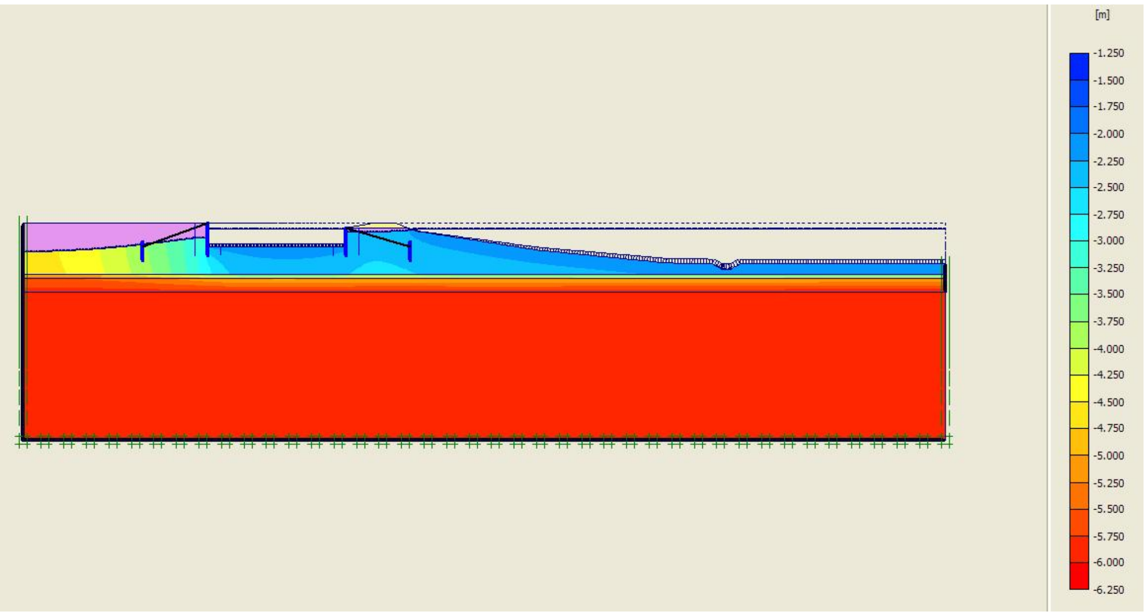

Figure 5.6: Groundwater head of phase 1

Figure 5.5 shows the calculated lowering of the phreatic surface left of the canal as affected by both the impermeability of the sheet pile wall and the downward seepage towards the deep sand layer.
The calculated distribution of the groundwater head in figure 5.6 demonstrates the uniform hydraulic head in the deeper sand layer at NAP-6.00m.
In figure 5.7 the calculated partial saturation above the phreatic surface left of the canal is shown.

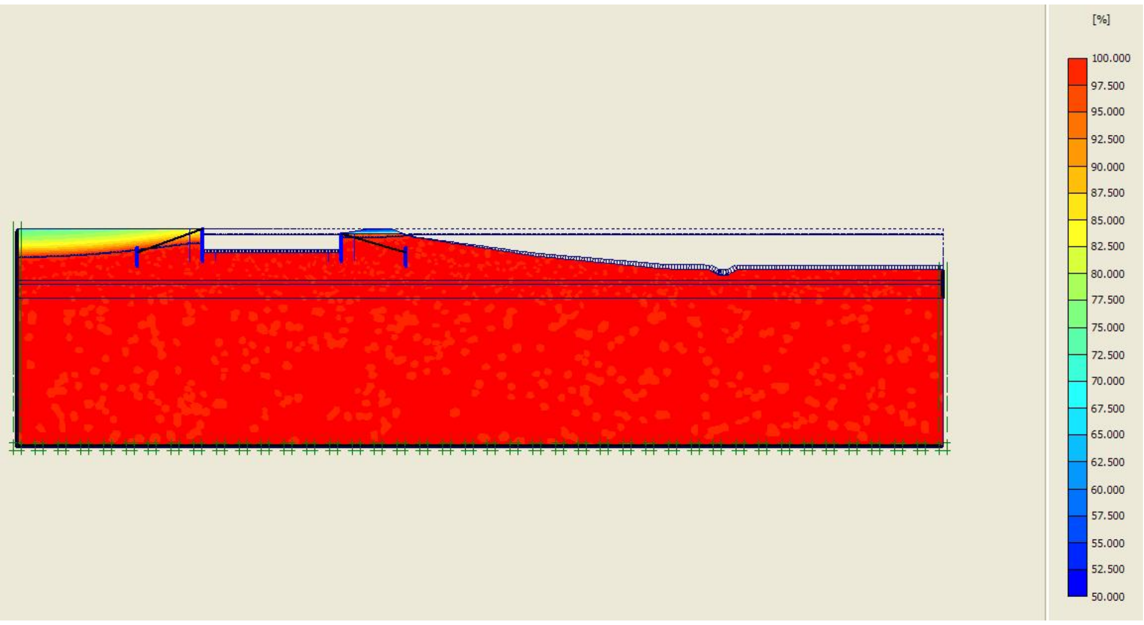

Figure 5.7: Degree of saturation of phase 1

Phase 1b – Plaxis deformation and stability analysis

After the PlaxFlow calculation is successfully finished the Plaxis deformation and stability calculation is performed. Below are the results of the Plaxis deformation and stability analysis. Figure 5.8 shows the displacements and figure 5.9 the strain.

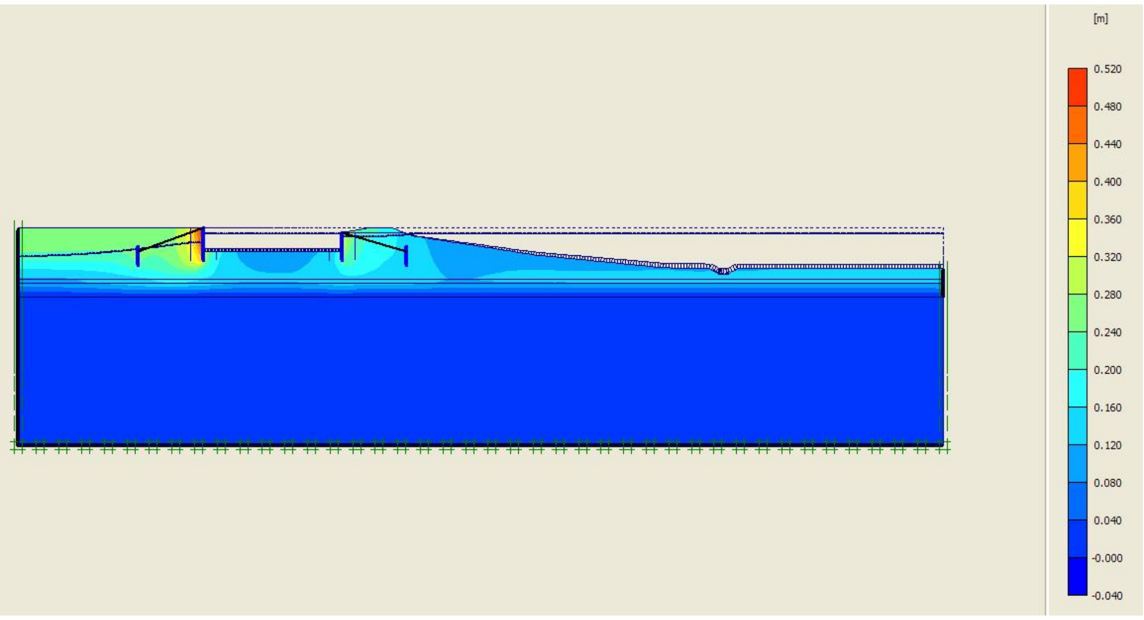

Figure 5.8: Displacements at the end of phase 1

The calculated maximum displacement as shown in figure 5.8 concerns the lateral displacement of the left sheet pile wall into the partially saturated soil left of the canal.

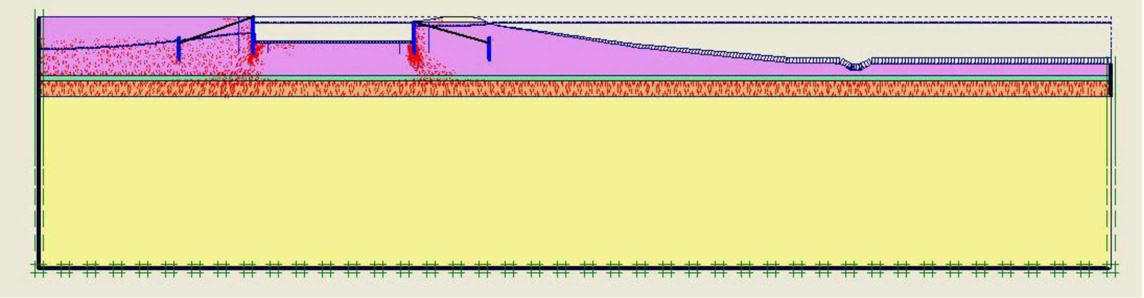

Figure 5.9: Total strains at the end of phase 1

The calculated strains occur in both the Holland peat left of the canal and the mainly vertical strains in the basis peat layer due to the difference in hydraulic head above and below the low-permeable clay layer, as illustrated in figure 5.9.

• Phase 2 – Lowering the groundwater table

The groundwater level of the upper cohesive layers (Holland peat, clay and basis peat) is set just below the ground surface while the hydraulic head of NAP-6.00m is maintained at the right boundary of the sand layer (see figure 5.10). A steady state flow analysis is performed in order to find the actual groundwater table.

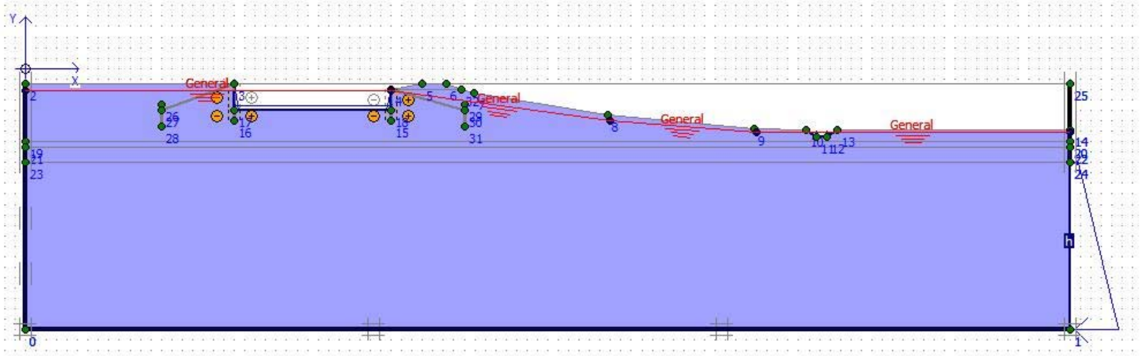

Figure 5.10: Input of phase 2 (red line shows the input water table)

<u>Phase 2a – Steady state PlaxFlow groundwater flow analysis</u>

The results of the steady-state PlaxFlow analysis can be seen in figures 5.11 to 5.13 below. Figure 5.11 shows the flow field, figure 5.12 the groundwater head and figure 5.13 the degree of saturation in the dike.

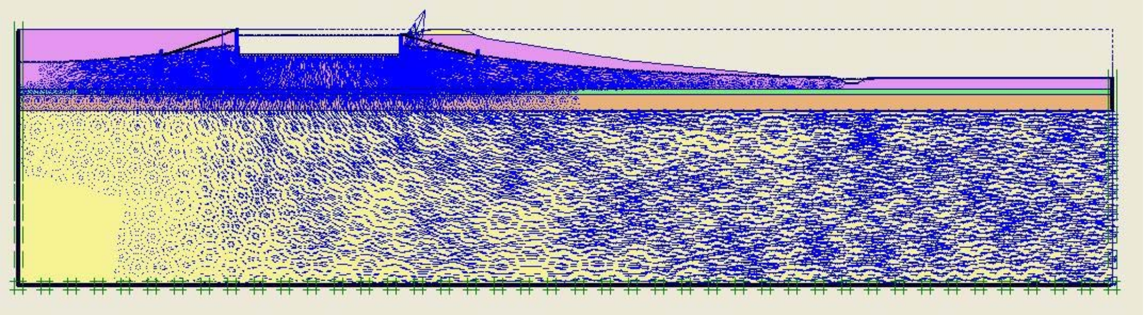

Figure 5.11: Flow field of phase 2

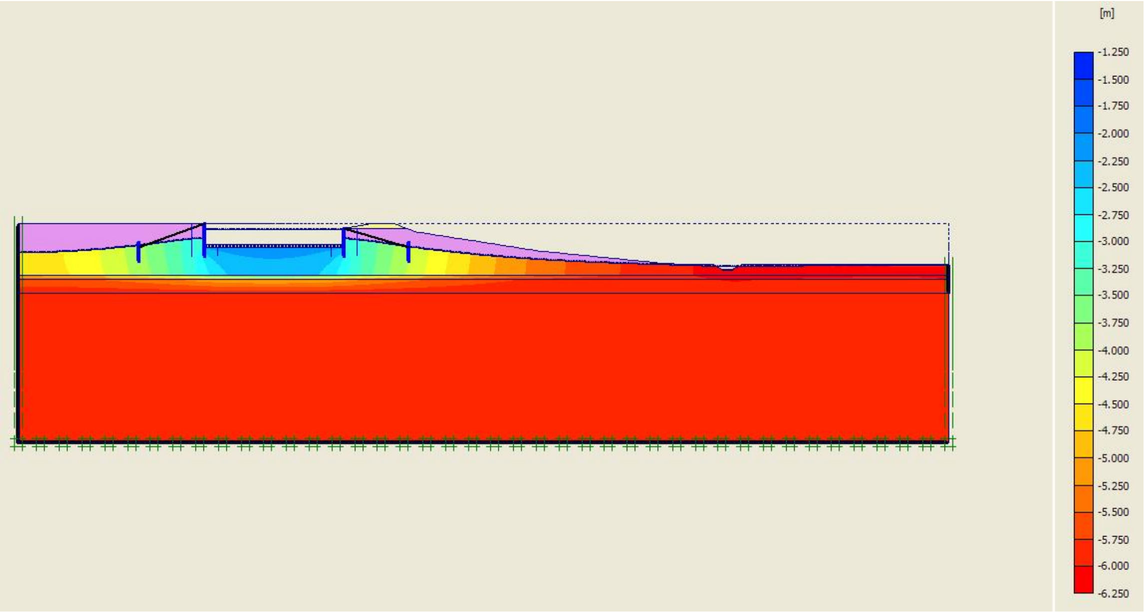

Figure 5.12: Groundwater head of phase 2

In figure 5.11 the calculated lowering of the phreatic level in the right (north) slope of the dike together with the mainly horizontal groundwater flow from the canal towards the ditch through the Holland peat layer are shown. In addition the calculated mainly downward seepage from the canal towards the deep sand layer can be observed.

Figure 5.12 shows the homogeneous hydraulic head distribution below the clay layer and the decreasing hydraulic head away from the bottom of the canal above the clay layer.

In figure 5.13 the degree of saturation above the phreatic level is shown, in this phase also in the upper part of the slope.

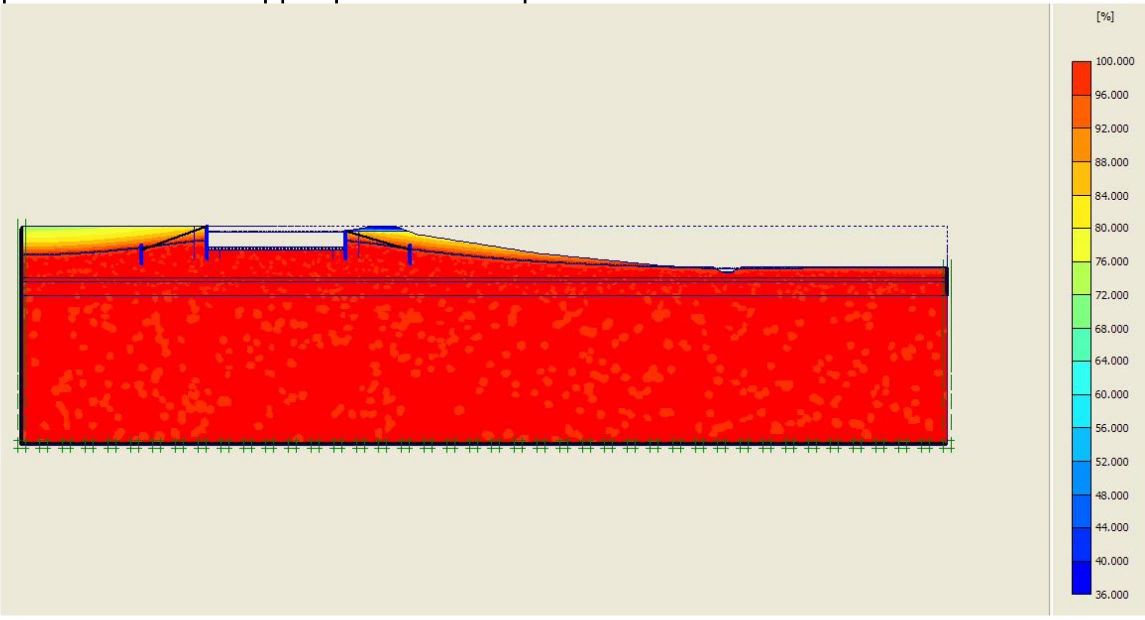

Figure 5.13: Degree of saturation of phase 2

Phase 2b – Plaxis deformation and stability analysis

Below are the results of the Plaxis deformation and stability analysis. Figure 5.14 shows the displacements and figure 5.15 the strain.

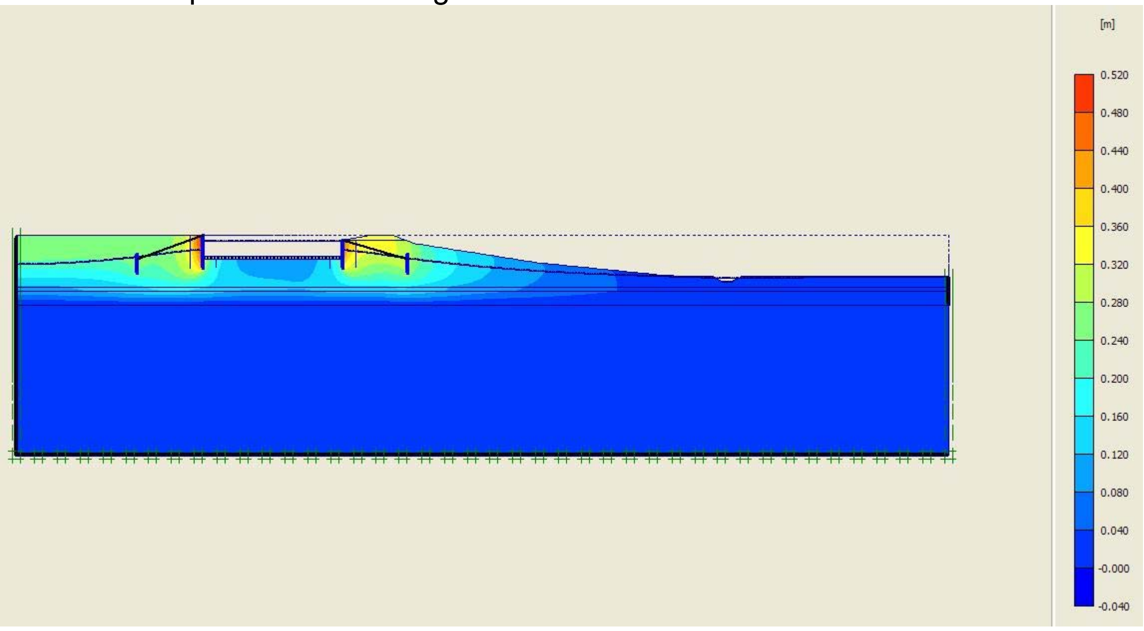

Figure 5.14: Displacements at the end of phase 2

The major displacements as calculated and illustrated in figure 5.14 occur near both sheet pile walls.

The calculated total strains as illustrated in figure 5.15 occur below and behind both the tips of both sheet pile walls and in the basis peat layer in the region below the canal. It is also noted that some strain has been calculated in the clay layer near the tip of the sheet pile wall on the side of the dike

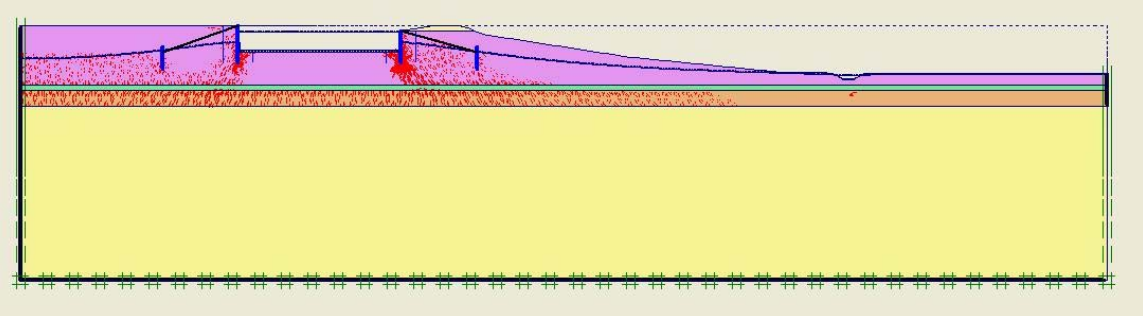

Figure 5.15: Total strains at the end of phase 2

Phase 2c – Plaxis failure analysis

The safety factor is calculated for the end of phase 2 using the Plaxis “phi-c reduction” analysis. With this analysis type the model is subjected to failure by reducing the strength parameters of the soil, in order to determine the safety factor (the ratio of the available shear strength to the minimum shear strength required for equilibrium).

Figure 5.16 contains the failure mechanism following phase 2, figure 5.17 the effective stresses before failure, figure 5.18 the incremental displacements and figure 5.19 the distribution of incremental deviatoric strain.

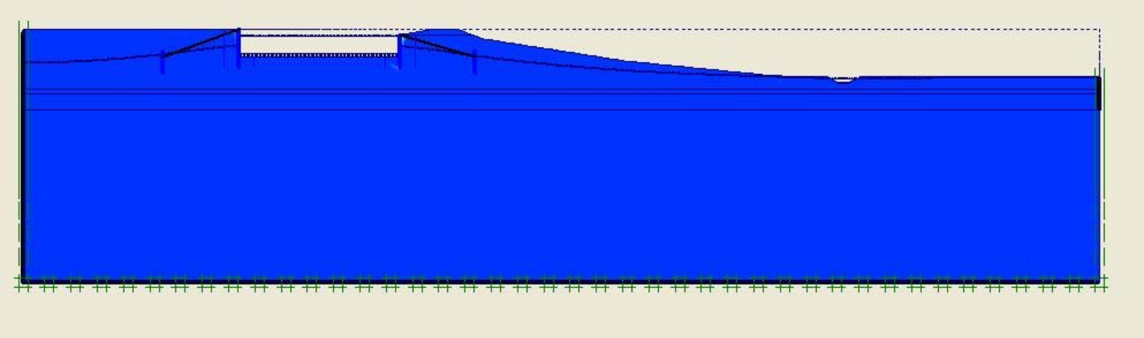

Figure 5.16: Failure mechanism following phase 2

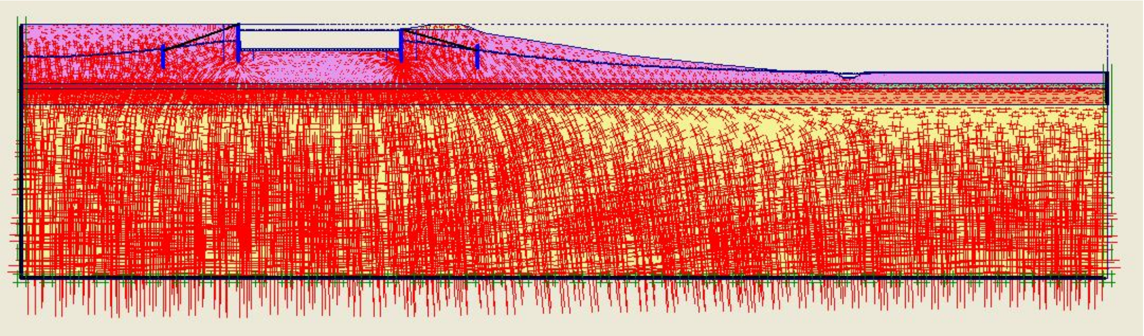

Figure 5.17: Effective stresses before failure of phase 2

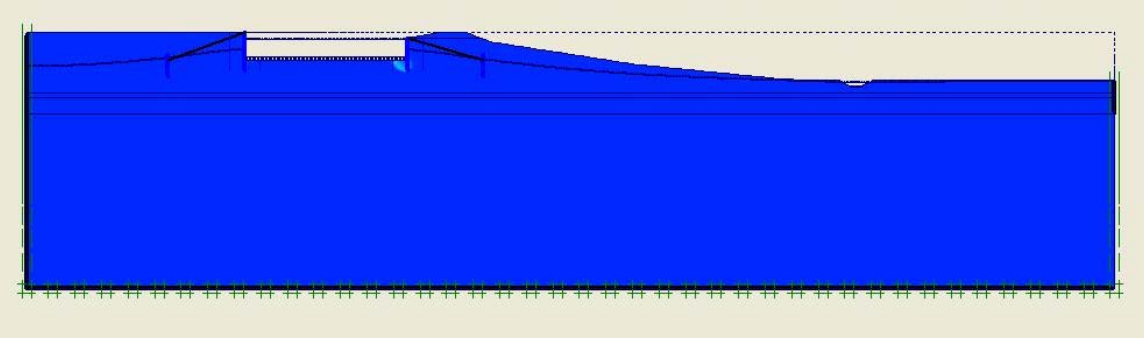

Figure 5.18: Incremental displacements following phase 2

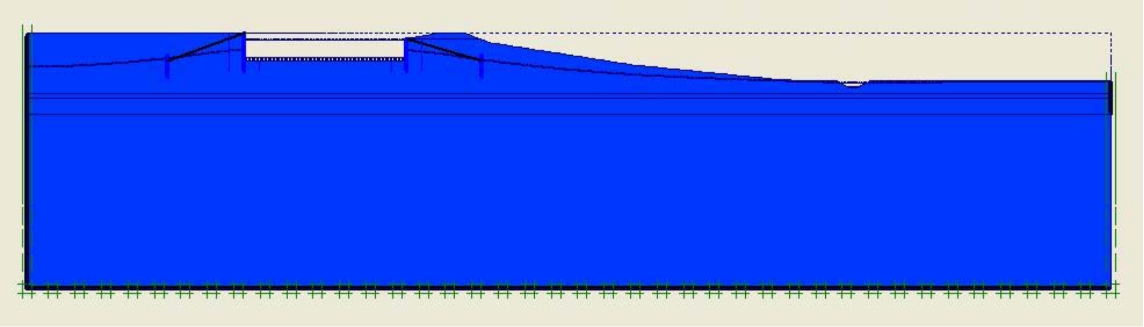

Figure 5.19: Incremental deviatoric strain following phase 2

In figures 5.16 to 5.19 above it can be seen that the point of maximum displacement as well as maximum deviatoric strain is located at the toe of the right sheet pile wall. The fact that there is no clear failure mechanism in figure 5.16 along with the fact that the calculated safety factor for phase 2 is 0.95 (although phase 2 is stable) leads to doubt regarding the reliability of the results of the failure calculation. It should be noted that the magnitude of the resulting displacements of the “phi-c reduction” calculation are totally unrealistic and therefore not relevant in any case. For this reason no legend is included in the figures resulting from such a calculation.

● Phase 3 – Drought

The previous phase, phase 2, is actually the initial situation in regard to the failure. It depicts the conditions (geometry, groundwater table etc.) as they are believed to have been at the beginning of the summer of 2003 and also for many years before. In this phase the "Reset displacements to zero" option of Plaxis is checked thus discarding any displacements that have been calculated in the previous 2 phases but keeping the stress history. Therefore the geometry of the dike is accurate and the stress history is taken into account in the calculation as well. The only change that is implemented in this phase is drought which is performed through a PlaxFlow transient groundwater flow analysis.

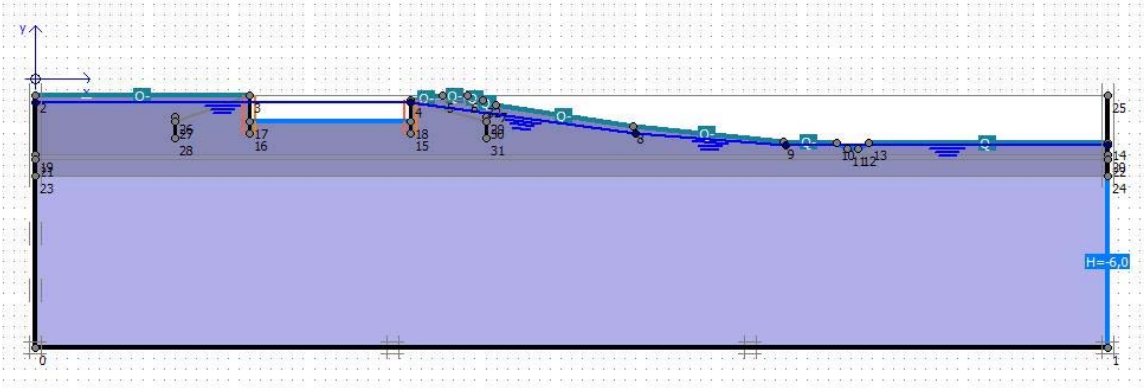

Figure 5.20: Input of phase 3

Phase 3a – Transient PlaxFlow groundwater flow analysis

The transient analysis time interval is set to 60 days. Drought is simulated by outflow of water from the entire ground surface. The amount of outflow is set to 5mm/day which is a realistic value for a dry summer.

Below in figures 5.21 to 5.23 the results of the transient PlaxFlow calculation can be found. Figure 5.21 shows the flow field, figure 5.22 the groundwater head and figure 5.23 the degree of saturation.

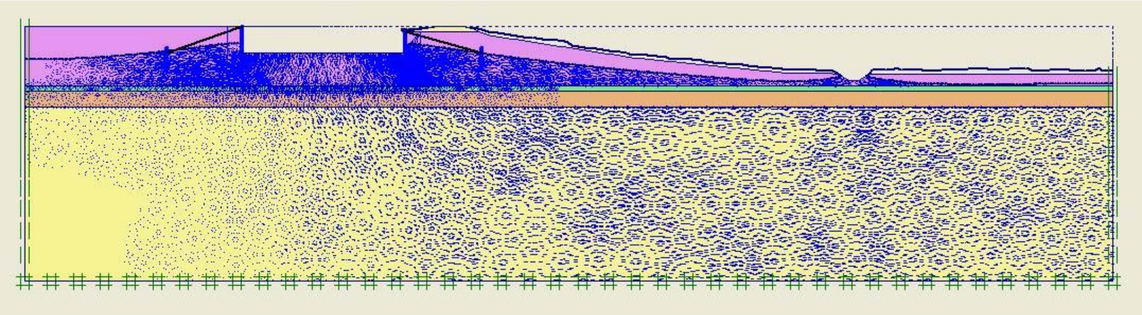

Figure 5.21: Flow field of phase 3

Figure 5.21 shows the lowering of the phreatic surface in both the slope of the peat dike and in the polder above the clay layer. It may also be noted that the ditch supplies infiltrating groundwater for both the toe of the slope and the polder. In addition the calculated downward seepage from the canal towards the deeper sand layer is illustrated.

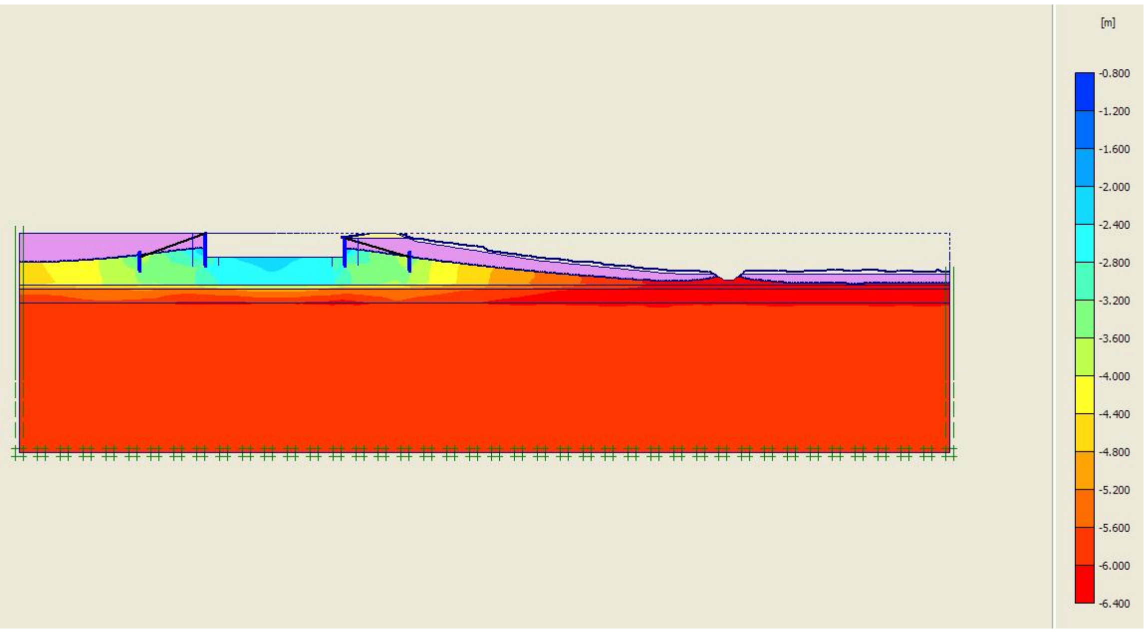

Figure 5.22: Groundwater head of phase 3

Figure 5.22 shows that the calculated region with significantly larger hydraulic head in the deeper sand layer is limited to the vicinity of the bottom of the canal above the clay layer.

Figure 5.23 shows the calculated significant reduction of the degree of saturation along the ground surface, including the surface of the slope.

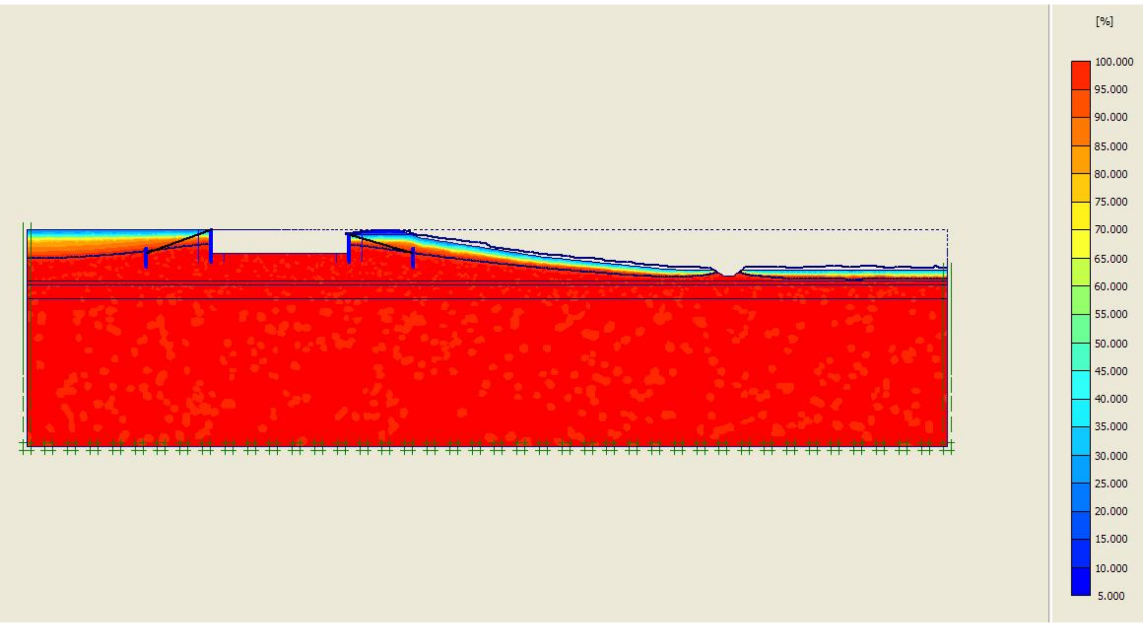

Figure 5.23: Degree of saturation of phase 3

Phase 3b – Plaxis deformation and stability analysis

The results of the Plaxis stability calculation can be found in figures 5.24 to 5.26 below. Figure 5.24 contains the displacements at the end of phase 3 (therefore after 60 days of drought) and figure 5.25 the total strains at the same time. Figure 5.26 contains the deviatoric strain invariants during phase 3.

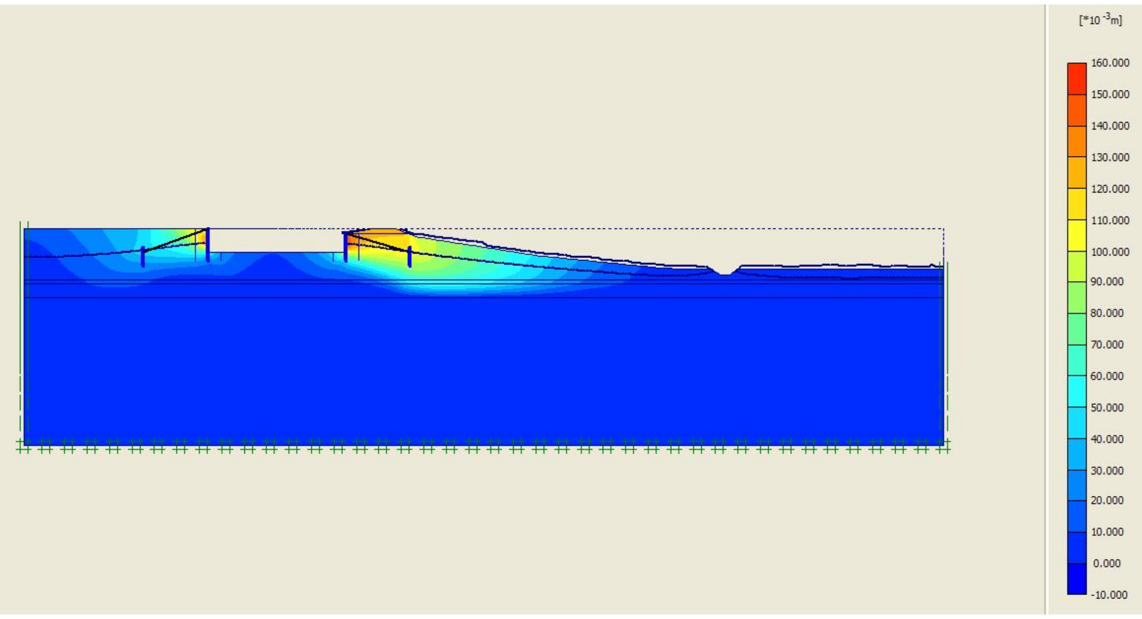

Figure 5.24: Displacement increments during phase 3

Figure 5.24 depicts the displacement increments due to 60 days of drought. The calculated lateral displacement increment of the sheet pile wall against the peat dike is of the order of 15 cm.

The calculated incremental strain as shown in figure 5.25 shows a somewhat concentrated band starting from the tip of the sheet pile wall and propagating under about 45^0 downwards through the Holland peat and clay layers and becoming more or less horizontal in the basis peat layer, where it decreases in magnitude towards the toe of the peat dike.

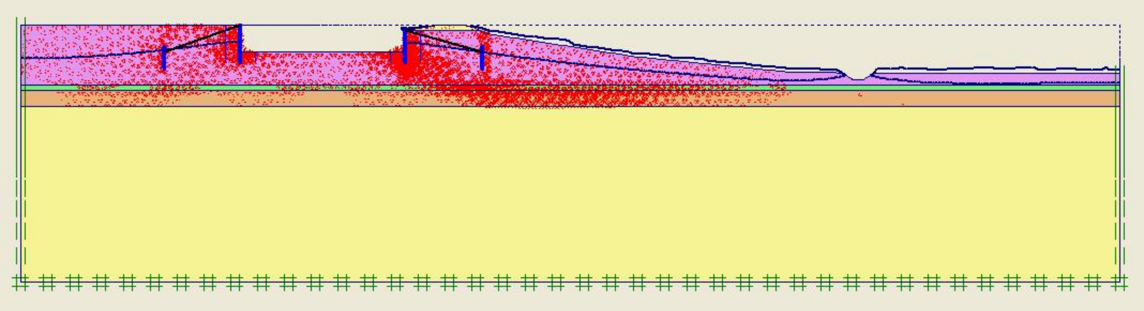

Figure 5.25: Strain increments during phase 3

Figure 5.26 shows some thin zones with relatively, large deviatoric strain invariants both in the slope and in the basis peat. However, these zones are not interconnected and consequently do not form a clear failure mechanism.

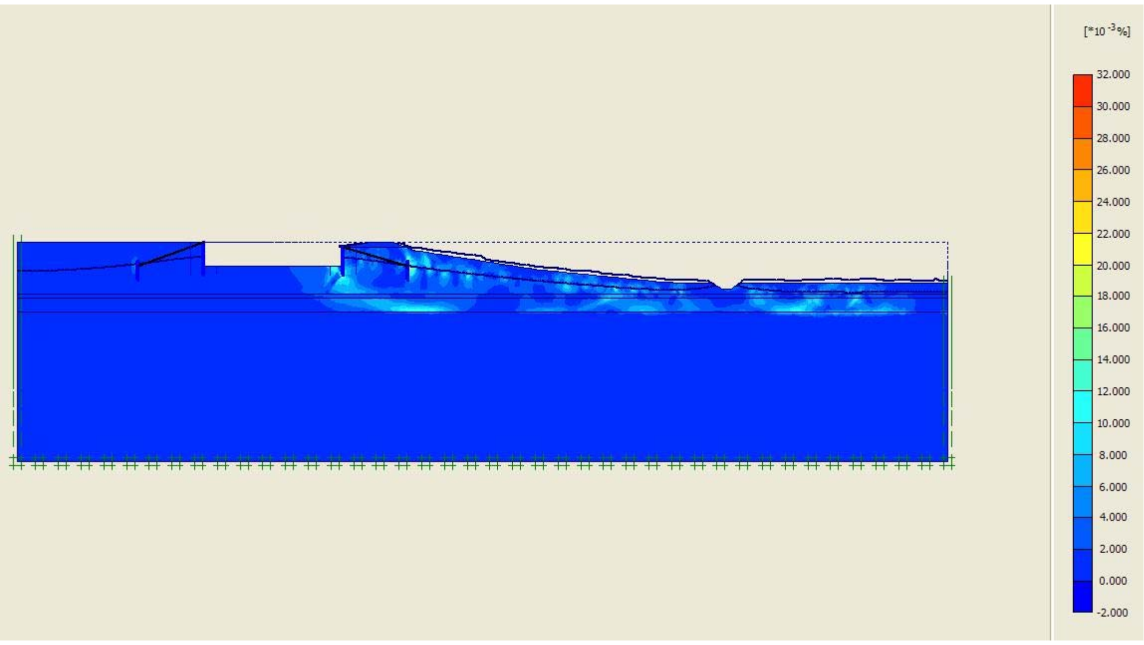

Figure 5.26: Distribution of deviatoric strain invariants during phase 3

<u>Phase 3c – Plaxis failure analysis</u>

The safety factor is calculated in the same way as for phase 2, using the "phi-c reduction" analysis of Plaxis. The results are depicted in figures 5.27 to 5.29. Figure 5.27 shows the displacements, figure 5.28 the strain distribution to failure and figure 5.29 the distribution of incremental deviatoric strains.

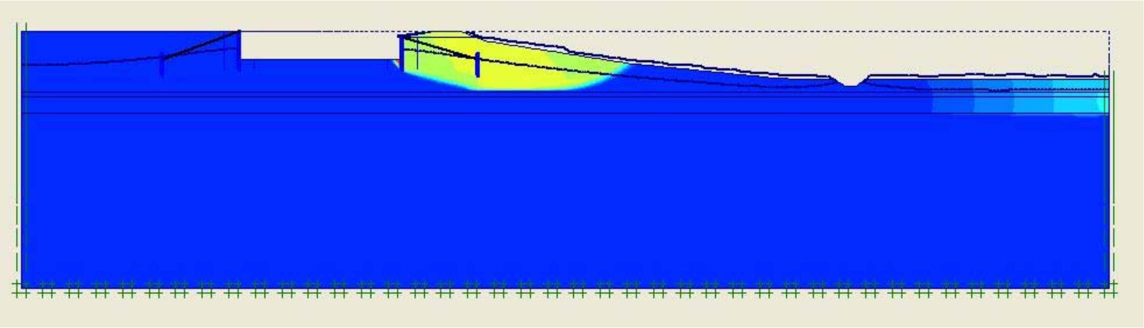

Figure 5.27: Incremental displacements at failure of phase 3

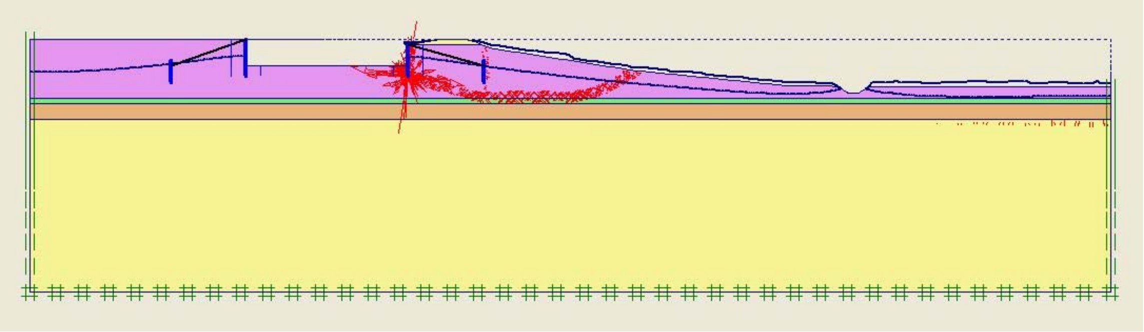

Figure 5.28: Strain increments at failure of phase 3

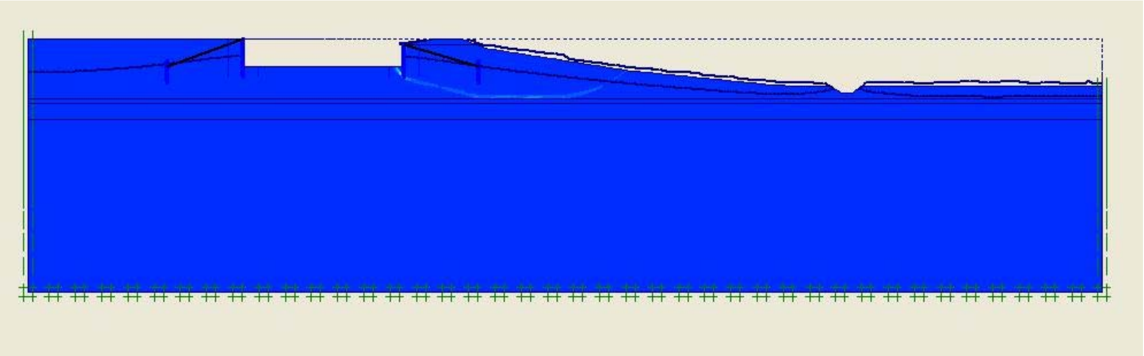

Figure 5.29: Incremental deviatoric strains at failure of phase 3

In figures 5.27 to 5.29 above the failure mechanism can be clearly viewed starting from the toe of the right sheet pile wall, going downwards at an angle of approximately 20^0 to the horizontal, continuing straight just above the clay layer and in the end going upwards towards the ground surface at the middle of the slope of the dike. In figures 5.27 and 5.28 there is also some vertical upward displacement and strain visible in the right hand side of the model at the polder. The safety factor calculated is 1.22.

5.5 Parametric study of Groundwater flow

A parametric study of the ground water flow by means of Plaxflow has been performed by considering three parameter values of the horizontal permeabilities of the Holland peat as indicated in table 5.1 below. Also the permeabilities (both horizontal and vertical) of the other cohesive soil types (clay and basis peat) are changed in accordance to the change of the horizontal permeability of Holland peat, i.e. for the dry case the permeabilities are 1/10 of the intermediate value (as can be found in table 4.4) and for the wet case 10 times the intermediate value. The result is 3 identical models with the only difference that in the dry case all the cohesive soil materials have a low permeability and in the wet case a high permeability when compared to the intermediate case (table 4.4). For reasons of simplicity in the following text emphasis is given on the horizontal permeability of the Holland peat since most of the dike consists of that material and this specific permeability is governing the flow situation.

Parameter	Dry case	Intermediate case	Wet case
k_x [m/day]	0.004	0.04	0.4

Table 5.1: Magnitudes of horizontal permeability k_x of saturated Holland peat as used in parametric study of ground water flow

First for each of the three cases of this parametric study the state of steady ground water flow without any evaporation was calculated. Subsequently in order to account for the effect of drought, for each case of the three cases of horizontal permeability of Holland peat (see table 5.1) the effect of an evaporation of 5 mm/day during 60 days was considered.

5.5.1 Steady groundwater flow at the end of phase 2

The results of the steady ground water flow at the end of phase 2 for the dry, intermediate and wet cases are shown in figures 5.30-5.32, 5.33-5.35 and 5.36-5.38 respectively. For the dry case figures 5.30, 5.31 and 5.32 concern the hydraulic head, the ground water flow vectors and the degree of saturation of the soil above the calculated phreatic surface respectively. For the intermediate case the same type of results are shown in figures 5.33, 5.34 and 5.35, while those for the wet case are shown in figures 5.36, 5.37 and 5.38.

From these results can be observed that the groundwater table is getting higher when permeability increases (wet case). The degree of saturation is relatively similar in all cases with a slight increase of saturation above the phreatic line in the wet case. The groundwater head is also similar in all cases.

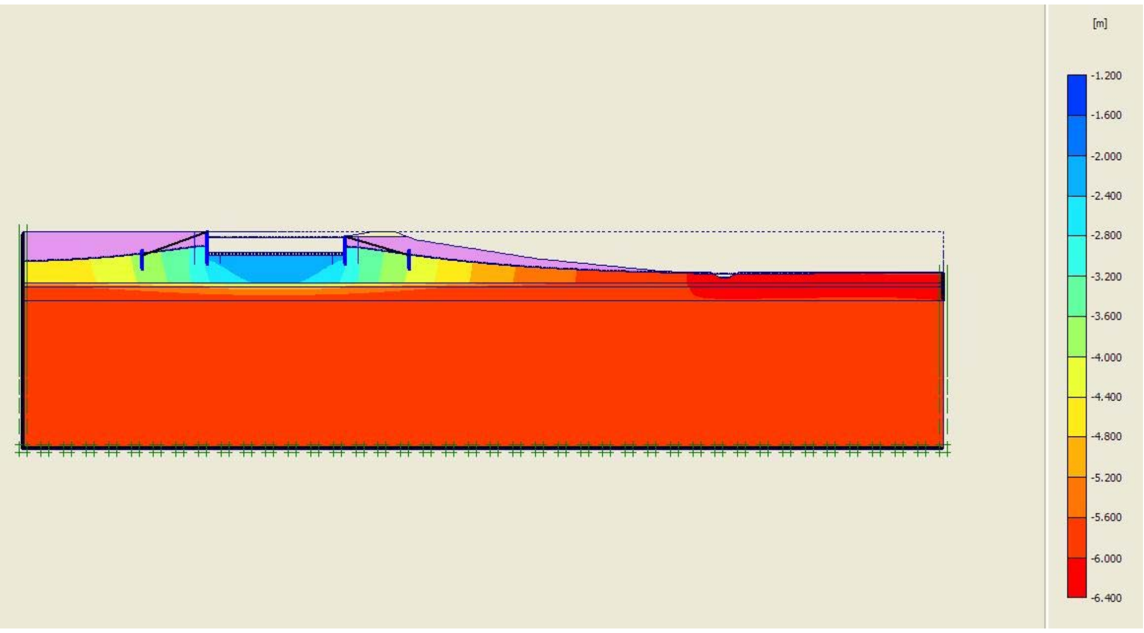

Figure 5.30: Calculated distribution of hydraulic head for steady ground water flow without any evaporation for the dry case with horizontal permeability $k_x = 0.004$ m/day of the Holland peat

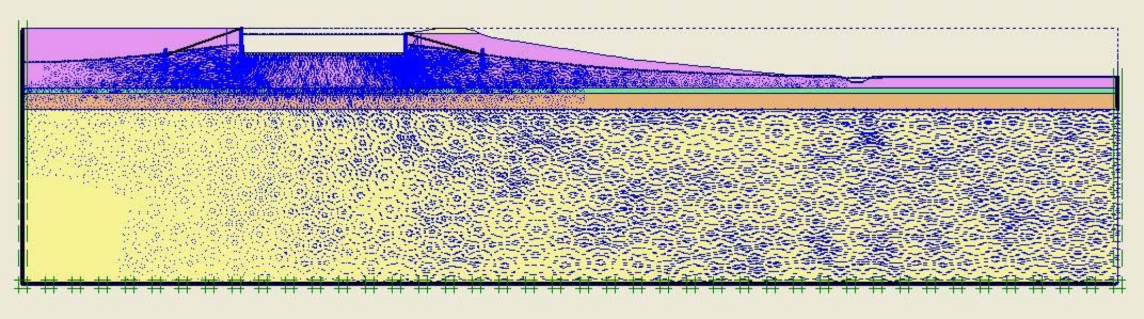

Figure 5.31: Calculated ground water flow vectors for steady ground water flow without any evaporation for the dry case with horizontal permeability $k_x = 0.004$ m/day of the Holland peat

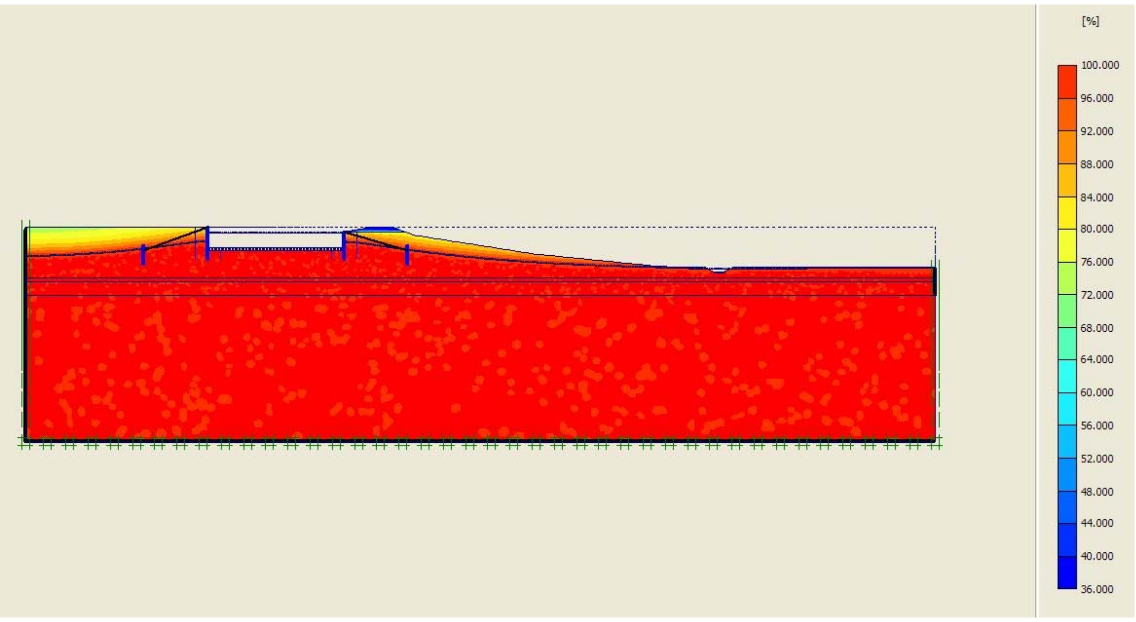

Figure 5.32: Calculated distribution of degree of saturation above the calculated phreatic surface for steady ground water flow without any evaporation for the dry case with horizontal permeability $k_x = 0.004$ m/day of the Holland peat

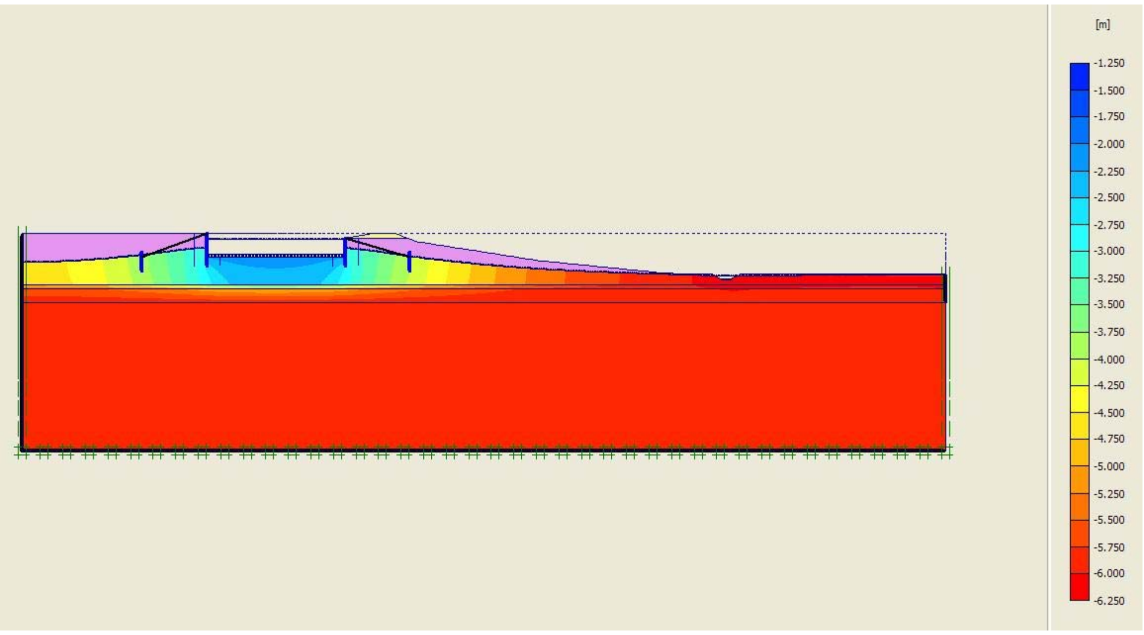

Figure 5.33: Calculated distribution of hydraulic head for steady ground water flow without any evaporation for the intermediate case with horizontal permeability $k_x = 0.04$ m/day of the Holland peat

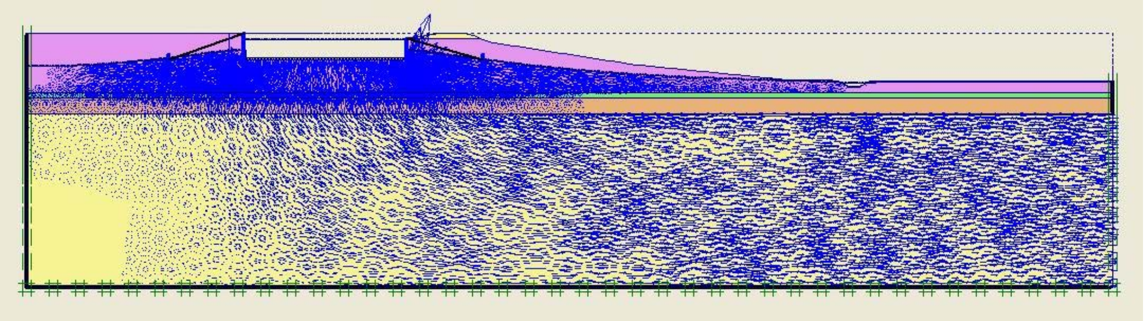

Figure 5.34: Calculated ground water flow vectors for steady ground water flow without any evaporation for the intermediate case with horizontal permeability $k_x = 0.04$ m/day of the Holland peat

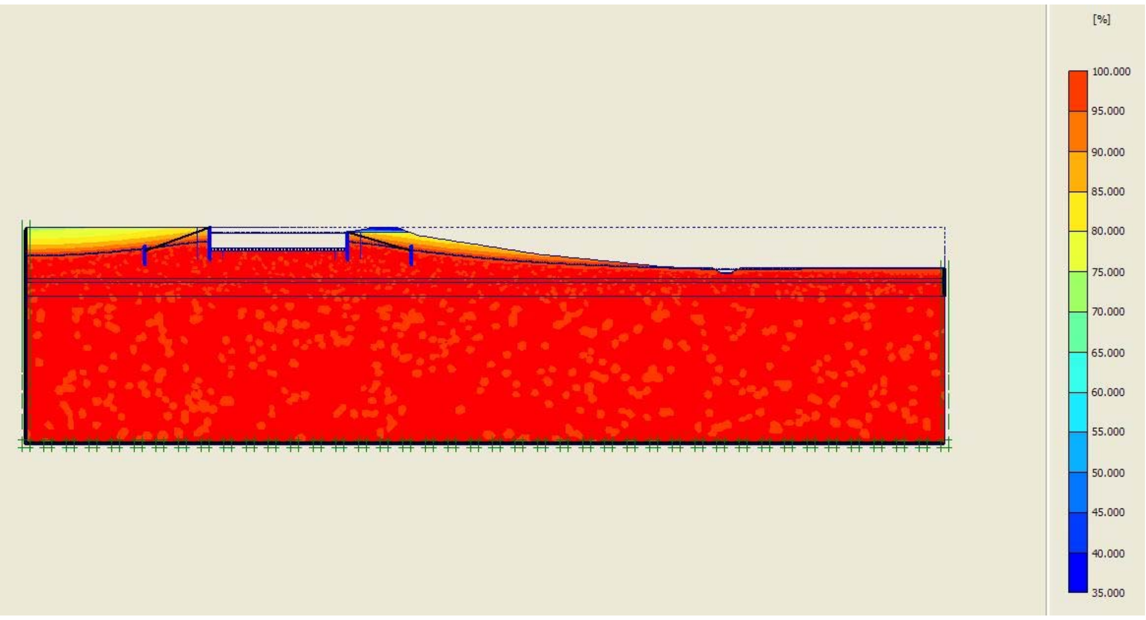

Figure 5.35: Calculated distribution of degree of saturation above the calculated phreatic surface for steady ground water flow without any evaporation for the intermediate case with horizontal permeability $k_x = 0.04$ m/day of the Holland peat

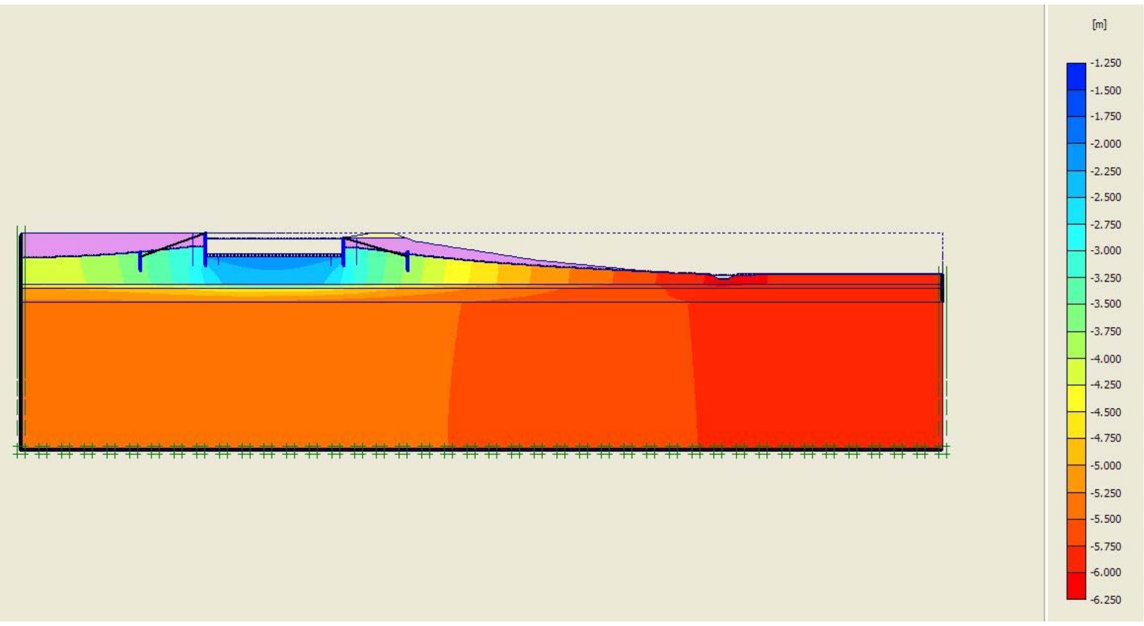

Figure 5.36: Calculated distribution of hydraulic head for steady ground water flow without any evaporation for the wet case with horizontal permeability $k_x = 0.4$ m/day of the Holland peat

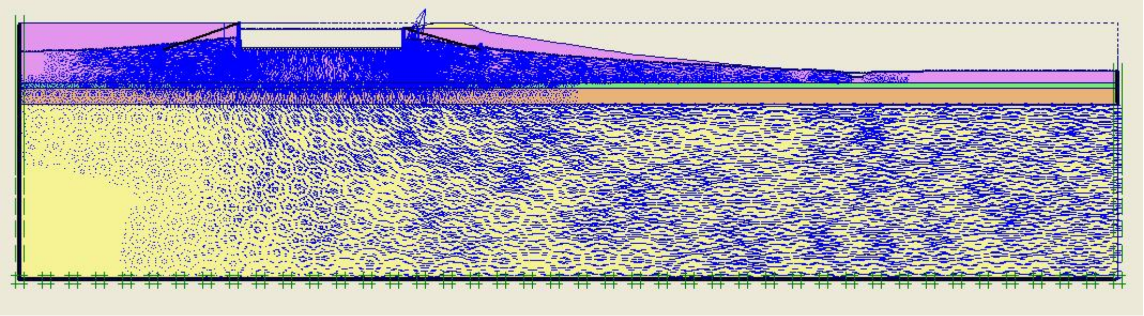

Figure 5.37: Calculated ground water flow vectors for steady ground water flow without any evaporation for the wet case with horizontal permeability $k_x = 0.4$ m/day of the Holland peat

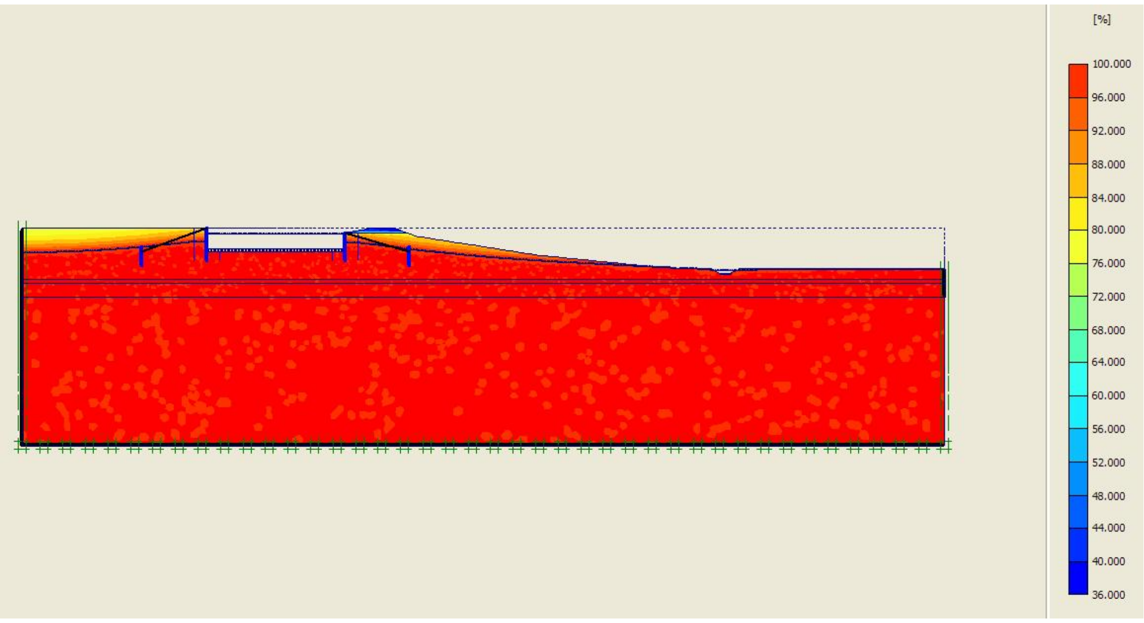

Figure 5.38: Calculated distribution of degree of saturation above the calculated phreatic surface for steady ground water flow without any evaporation for the wet case with horizontal permeability $k_x = 0.4$ m/day of the Holland peat

Comparisons of the calculated results for each of the three classes of permeabilities show that all results are practically equal, as could be expected.

5.5.2 Groundwater flow due to drought at the end of phase 3

The effect of drought on the ground water flow and the degree of saturation S^w above the phreatic surface was investigated in a parametric study. For each of the above mentioned dry, intermediate and wet cases the effect of drought was accounted for enforcing an evaporation of 5 mm/day during 60 days along the whole ground surface without prescribed water level.

The calculated results are of the same kind as considered for the earlier three cases of steady ground water flow without any evaporation as shown in figures 5.39-5.41, 5.42-5.44 and 5.45-5.47 for the dry, intermediate and wet cases respectively.

The results of the dry case are shown in figures 5.39, 5.40 and 5.41, concerning the hydraulic head, the ground water flow vectors and the degree of saturation of the soil above the calculated phreatic surface respectively. For the intermediate case the same type of results are shown in figures 5.42, 5.43 and 5.44, while those for the wet case are shown in figures 5.45, 5.46 and 5.47.

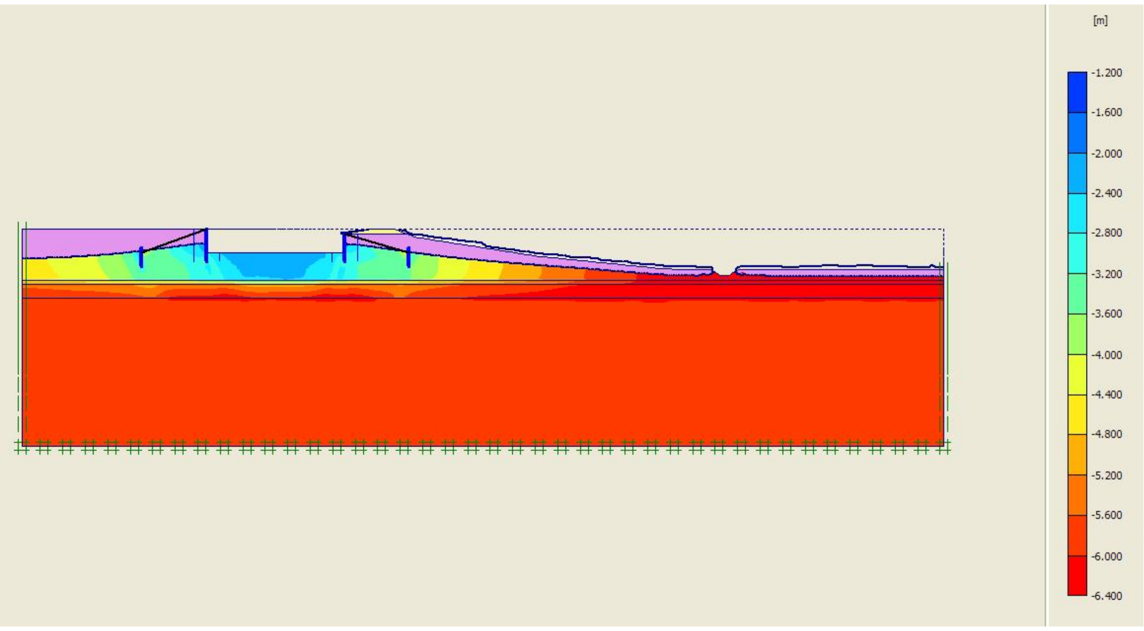

Figure 5.39: Calculated distribution of hydraulic head after 60 days of evaporation of 5 mm/day for the dry case with horizontal permeability $k_x = 0.004$ m/day of the Holland peat

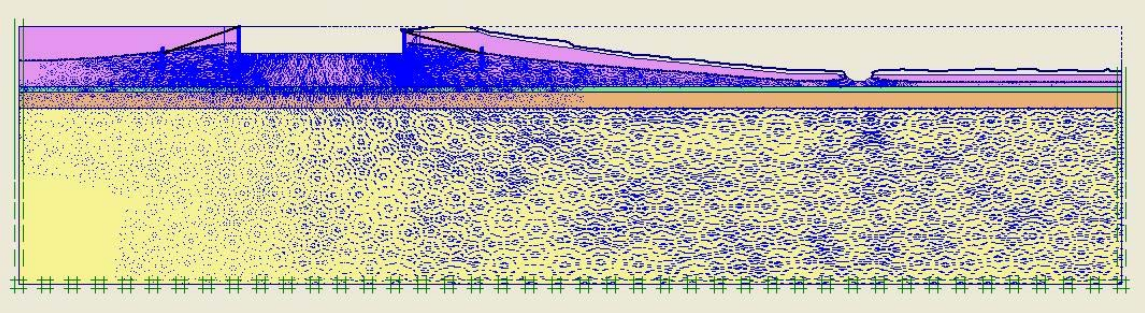

Figure 5.40: Calculated ground water flow vectors after 60 days of evaporation of 5 mm/day for the dry case with horizontal permeability $k_x = 0.004$ m/day of the Holland peat

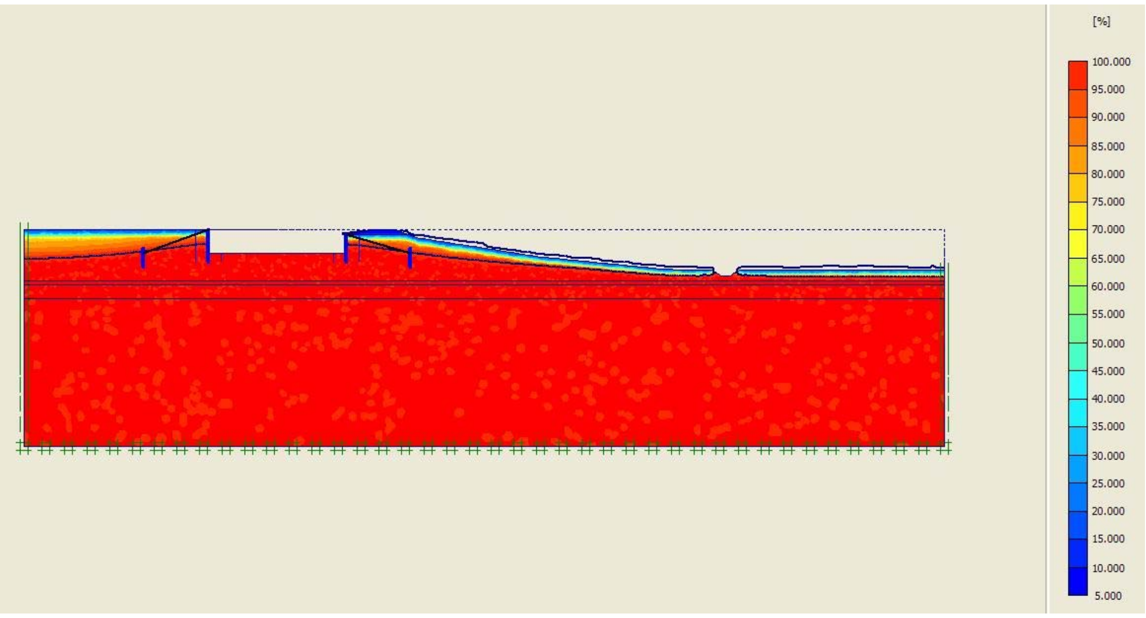

Figure 5.41: Calculated distribution of degree of saturation after 60 days of evaporation of 5 mm/day for the dry case with horizontal permeability $k_x = 0.004$ m/day of the Holland peat

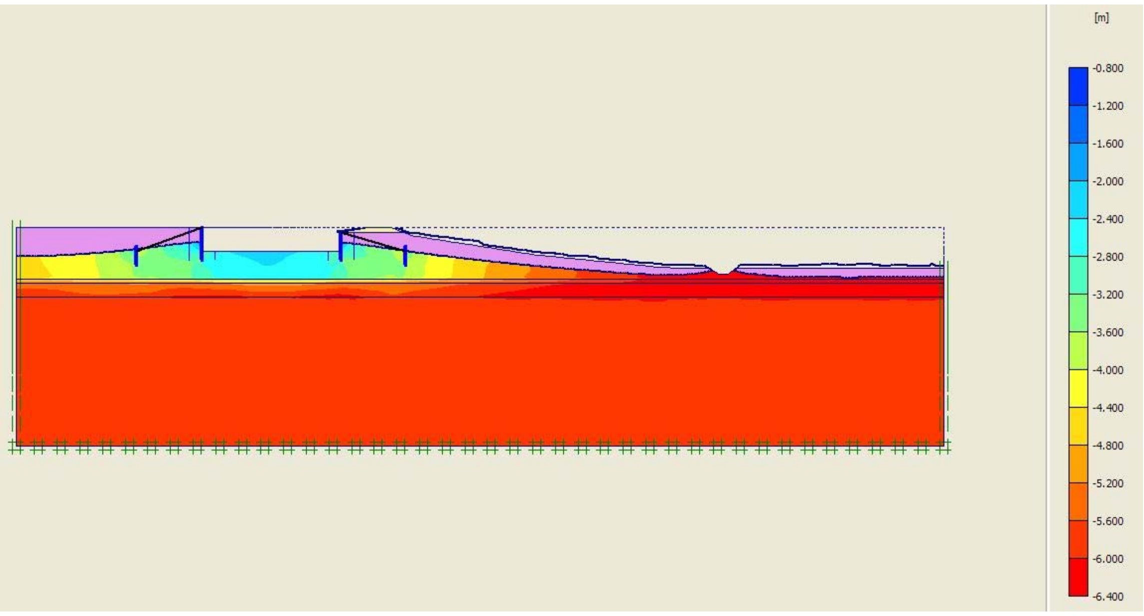

Figure 5.42: Calculated distribution of hydraulic head after 60 days of evaporation of 5 mm/day for the intermediate case with horizontal permeability $k_x = 0.04$ m/day of the Holland peat

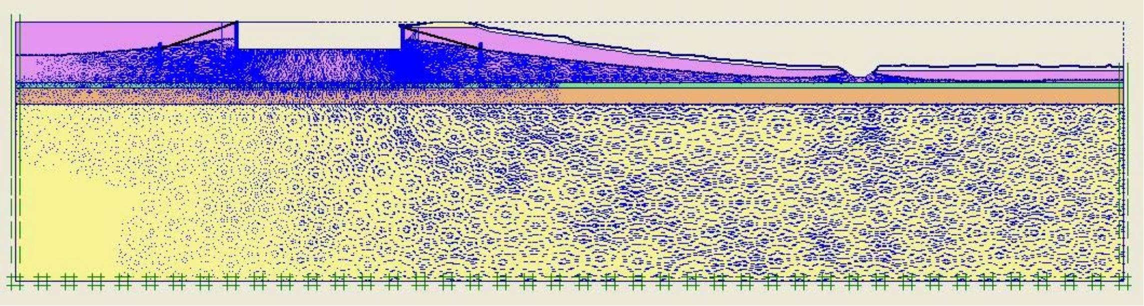

Figure 5.43: Calculated ground water flow vectors after 60 days of evaporation of 5 mm/day for the intermediate case with horizontal permeability $k_x = 0.04$ m/day of the Holland peat

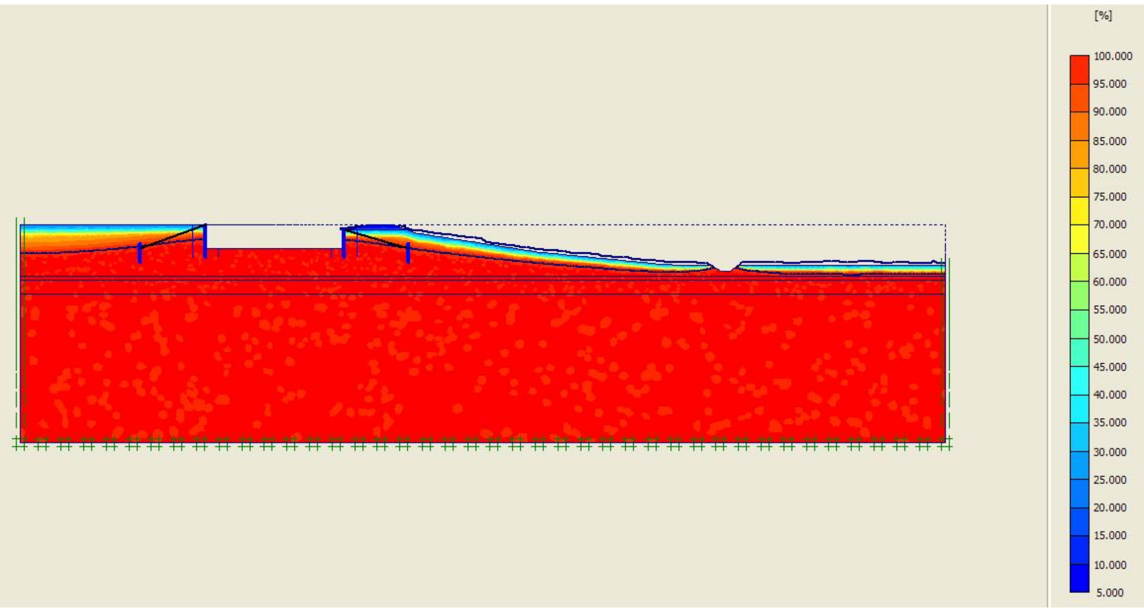

Figure 5.44: Calculated distribution of degree of saturation after 60 days of evaporation of 5 mm/day for the intermediate case with horizontal permeability $k_x = 0.04$ m/day of the Holland peat

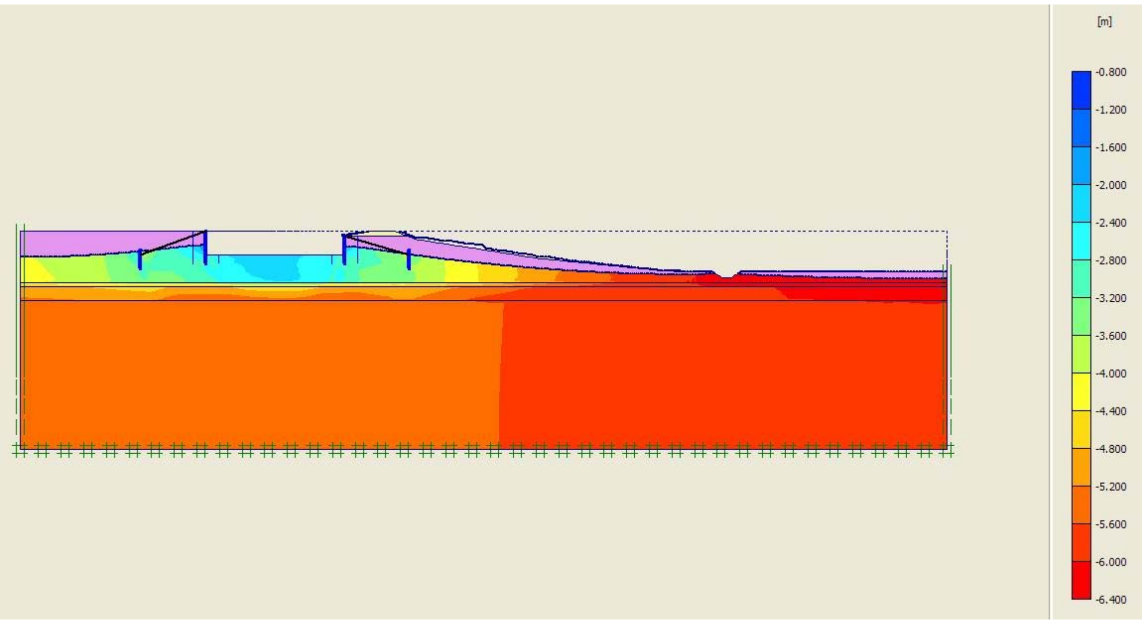

Figure 5.45: Calculated distribution of hydraulic head after 60 days of evaporation of 5 mm/day for the wet case with horizontal permeability $k_x = 0.4$ m/day of the Holland peat

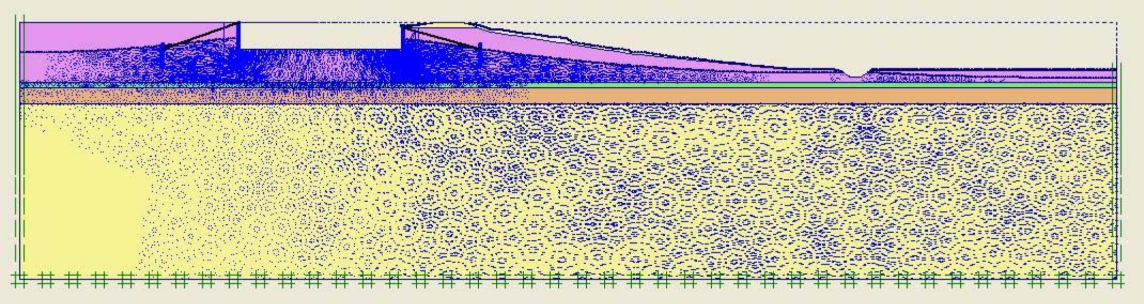

Figure 5.46: Calculated ground water flow vectors after 60 days of evaporation of 5 mm/day for the wet case with horizontal permeability $k_x = 0.4$ m/day of the Holland peat

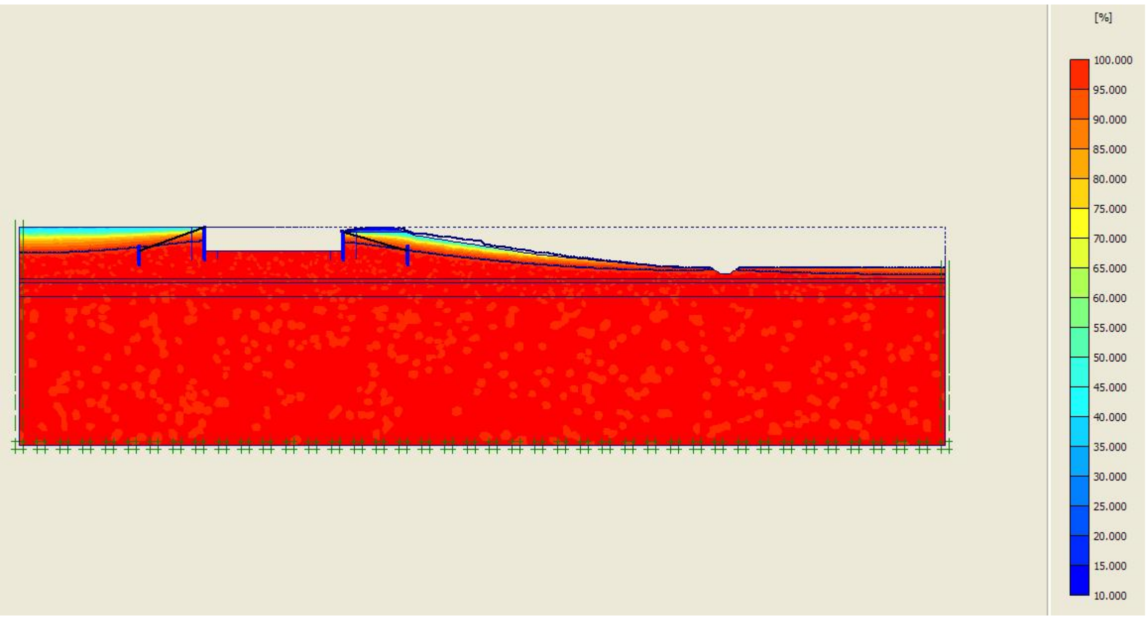

Figure 5.47: Calculated distribution of degree of saturation after 60 days of evaporation of 5 mm/day for the wet case with horizontal permeability $k_x = 0.4$ m/day of the Holland peat

Comparison of figures 5.41, 5.44 and 5.47 shows that the thickness of the unsaturated soil layer above the phreatic surface increases with decreases permeability of the Holland peat, from the wet case (figure 5.47) via the intermediate case (figure 5.44) to the dry case (figure 5.41). This is consistent with the results of the groundwater flow vectors in figures 5.40, 5.43 and 5.46, showing that for the wet case (figure 5.46) hardly any water infiltrates the ground from the ditch, while in the intermediate case (figure 5.43) already significant infiltration can be observed. In the dry case (figure 5.40) both the thickness of the unsaturated Holland peat layer and the infiltration of water from the ditch are even more significant.

When comparing the calculated results of the earlier steady states with the corresponding states after 60 days of drought, it is noted that in particular in the lower half of the slope for both the intermediate and dry cases the degree of saturation above the phreatic surface has decreased significantly. To quantify these changes for both the lower half of the slope and the remainder of the embankment both the level of the phreatic surface and the mean degree of saturation have been extracted from the calculated results for three locations along the slope, namely at about ¼, ½ and ¾ width down the slope as can be seen in figure 5.48 below.

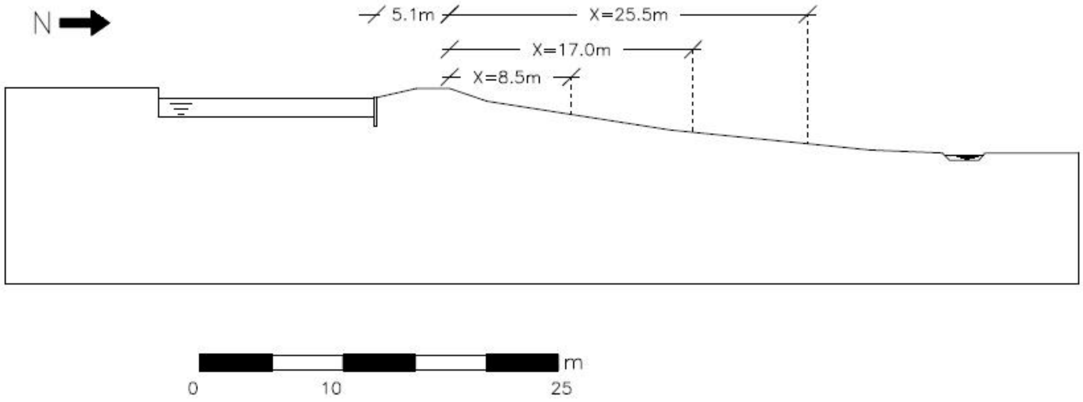

Figure 5.48: Sketch of locations X from the crest of the embankment where water levels (GW) Z and the calculated average degrees of saturation S^w have been determined

The results have been collected in table 5.2.

Case	State	X=8.5 [m]		X=17.0 [m]		X=25.5 [m]	
		Z-GW [m]	Mean S^w	Z- GW [m]	Mean S^w	Z-GW [m]	Mean S^w
Dry	Steady state	-4.79	0.91	-5.45	0.94	-5.82	0.97
Dry	After drought	-4.95*	0.63	-5.92*	0.61	-6.80*	0.50
Intermediate	Steady state	-4.77	0.91	-5.42	0.94	-5.79	0.97
Intermediate	After drought	-4.90	0.68	-5.77	0.68	-6.44	0.64
Wet	Steady state	-4.49	0.92	-5.13	0.96	-5.57	0.99
Wet	After drought	-4.85	0.76	-5.62	0.86	-6.08	0.94

Table 5.2: Calculated ground water levels (GW) Z and mean degrees of saturation S^w at three locations X from the crest of the embankment horizontally down the slope for each of the dry, intermediate and wet cases both at the earlier steady state and the state after 60 days of drought

It is noted that the calculated phreatic levels for the dry case concern estimates as the graphical results are suspected to be very inaccurate. The estimated values are indicated by the symbol *.

5.5.3 Unsaturated self-weight of Holland peat

To take account of the loss of the self-weight of the soil in the embankment above the phreatic surface due to drought, for each of the three cases, namely the dry, intermediate and wet cases, representative unsaturated dry-weights of the Holland peat above the phreatic surface are calculated on the basis of the calculated distributions of the degree of saturation after 60 days of drought. Furthermore, considering that the mean degree of saturation also depends on the location along the slope in fact for each case two mean degrees of saturation are recognized, namely one for the lower half of the slope together with the polder and the other for the remainder of the cross section of the embankment. The resulting mean degrees of saturation are collected in table 5.3.

Next application of eq. (4.21) for these mean degrees of saturation together with the mean data of porosity and material density in table 4.3 leads to the mean unsaturated self-weights as also collected in table 5.3.

Case	State	Lower half of slope and polder		Remainder of embankment	
		Mean S^w	γ_{unsat} kN/m^3	Mean S^w	γ_{unsat} kN/m^3
Dry	After drought	0.56	6.06	0.62	6.57
Intermediate	After drought	0.66	6.91	0.68	7.08
Wet	After drought	0.90	8.95	0.81	8.18

Table 5.3: Calculated mean degrees of saturation S^w above the phreatic surface after 60 days of drought along the lower half of the slope and the polder and in the remainder of the embankment

5.6 Parametric study of deformation, instability and failure

Based on the results of table 5.3 the model is modified in order to take into account the variation of the unsaturated self-weight of Holland peat. The upper Holland peat layer is thus divided vertically into 2 parts at the middle of the slope of the embankment. The 2 different material models that are applied contain the same values for all parameters (see table 4.4) except for the unsaturated volumetric weight for which the values from table 5.3 are used. The model to be used for the final analyses can be seen in figure 5.49 below.

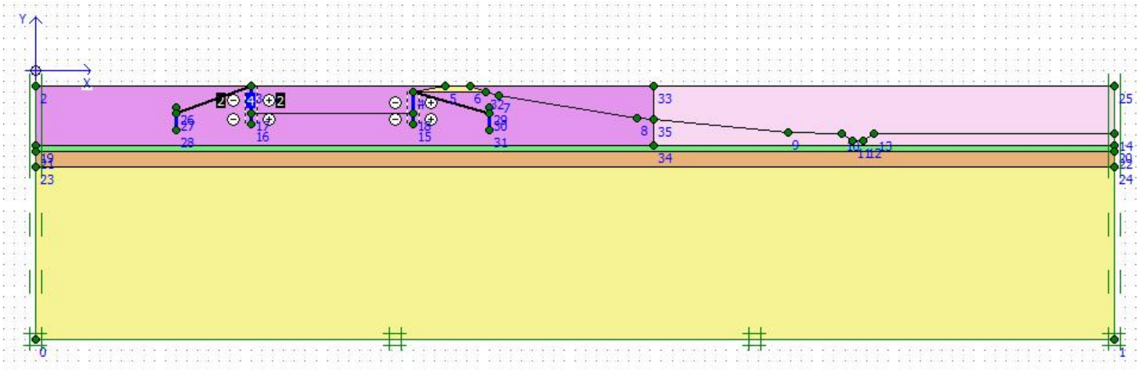

Figure 5.49: Geometry of final model with the 2 regions of Holland peat with different mean unsaturated weights

A governing factor in the stability analyses is naturally the strength of the material. In order to see the effect of the strength of the material for each of the 3 cases regarding the permeability (dry, intermediate and wet) 3 different cases of strength are investigated for all the material types. One with the average values of the strength properties (cohesion c and angle of internal friction φ), one with the average values minus one quarter of the standard deviation and one with the average values plus one quarter of the standard deviation. The specific variation of one quarter of the standard deviation was selected through trial and error since larger percentages of standard deviation led to numerically unstable models. The calculation phases are defined in the same way as described in paragraph 5.4 in all cases, thus resulting to 9 different models as illustrated in table 5.4 below.

Case	Dry	Intermediate	Wet
$k_x (m/day)$	0.004	0.04	0.4
$\gamma_{unsat} (kN/m^3)$	6.06 / 6.57	6.91 / 7.08	8.95 / 8.18
$mean - \sigma/4$ (Low strength)	DL	IL	WL
$mean$ (Mean strength)	DM	IM	WM
$mean + \sigma/4$ (High strength)	DH	IH	WH

Table 5.4: Nine cases for parametric study of deformation, stability and failure

The mean values and standard deviations of the strength properties (cohesion c and angle of internal friction φ) can be found in tables 3.5 to 3.8. The rest of the model parameters remain the same in all the different models and can be seen in table 4.4. Following are the results of the parametric analyses. In total there are 9 models analyzed (see table 5.4). The procedure followed in all cases is the one described in paragraph 5.4.

5.6.1 Steady state and failure at the end of phase 2

In the same manner as in paragraph 5.4 the safety factor was calculated for each of the 9 models at the end of phase 2 (the assumed situation at the beginning of summer of 2003). The results are similar to the ones in paragraph 5.4 (see figures 5.16-5.19) with displacement and strain exclusively located around the sheet pile wall. No failure mechanism can be identified in any of the results and therefore they are omitted. Below in table 5.5 the accumulated safety factors for all 9 models can be found.

Parameter values	Safety factors at end of phase 2		
	Dry	Intermediate	Wet
$mean - \sigma / 4$	1.21	1.45	1.43
$mean$	0.77	0.82	1.68
$mean + \sigma / 4$	1.75	1.21	1.69

Table 5.5: Safety factors for all 9 models at end of phase 2

The safety factors of the DM and IM models are below 1.00 which raises concern about the reliability of the “phi-c reduction” analyses performed at the end of phase 2, since in all cases phase 2 was stable. Furthermore for the intermediate case of saturation the calculated safety factor for the lower parameter values ($mean - \sigma / 4$) is larger (1.45) than the value (1.21) for the larger parameter values ($mean + \sigma / 4$). In most cases the tolerated error for the iterative procedure calculating phase 2 was reduced from the default value of 0.01 to 0.0001. This was hoped to lead to more accurate results but unfortunately the safety factors for 2 of the 9 models remain unrealistic. The rest of the safety factors calculated seem reasonable enough but the absence of any clear failure mechanism in any of the models renders these results as untrustworthy.

5.6.2 Drought and failure at the end of phase 3

In this paragraph the results of phase 3 (simulated drought) of each model will be shown. For each of the models analyzed, the effective stresses, displacements and shear strains are shown in the figures below. Furthermore, the results of the “phi-c reduction” analyses are shown for each model, namely the displacements of the failure mechanism following phase 3 as well as the deviatoric strain invariant distribution of the failure mechanism following phase 3. First the results of the 3 dry cases with different strengths (DL, DM and DH) can be found in figures 5.50 to 5.54 for the dry case with low strength (DL), in figures 5.55 to 5.59 for the dry case with mean strength (DM) and in figures 5.60 to 5.64 for the dry case with high strength (DH). Following are the results of the 3 intermediate cases with different strengths (IL, IM and IH). Figures 5.65 to 5.67 refer to the intermediate case with low strength (IL), figures 5.68 to 5.72 to the intermediate case with mean strength (IM) and figures 5.73 to 5.77 to the intermediate case with high strength (IH). The results of the 3 wet cases with different strengths (WL, WM and WH) are presented in figures 5.78 to 5.82 for the wet case with low strength (WL), in figures 5.83 to 5.87 for the wet case with mean strength (WM) and in figures 5.88 to 5.92 for the wet case with high strength (WH). In all figures the groundwater table is visible as a dark blue line below the ground surface.

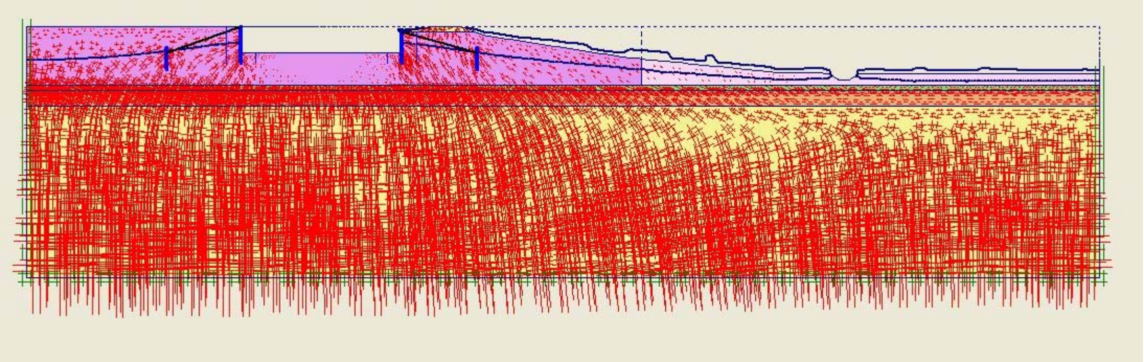

Figure 5.50: Effective stress distribution at the end of phase 3 of DL model

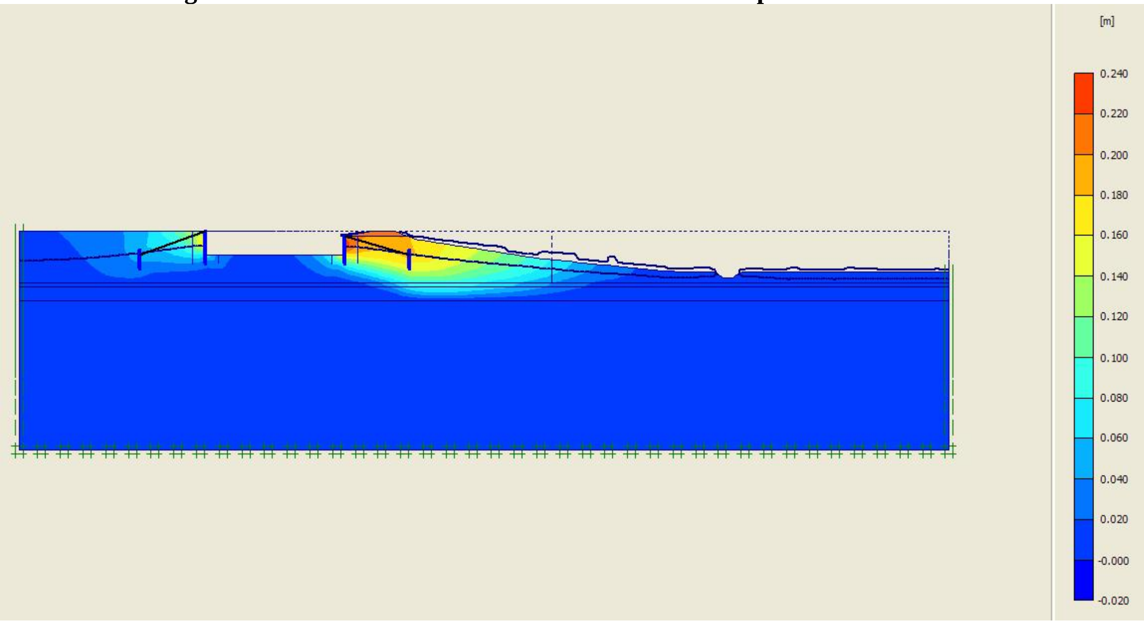

Figure 5.51: Displacements after drought of DL model

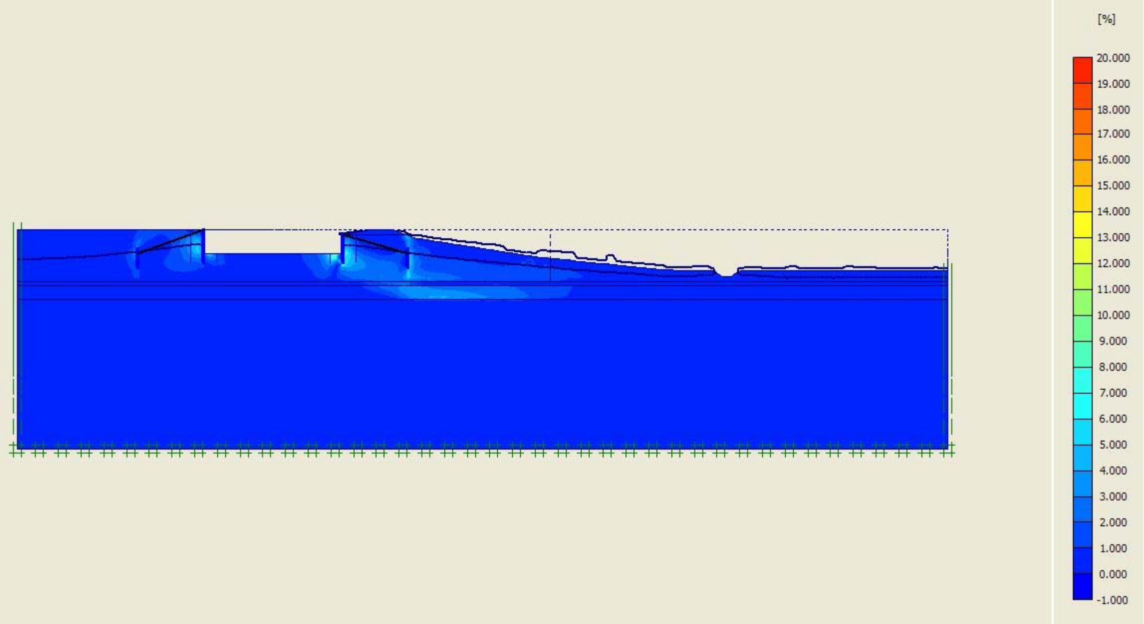

Figure 5.52: Shear strain invariants after drought of DL model

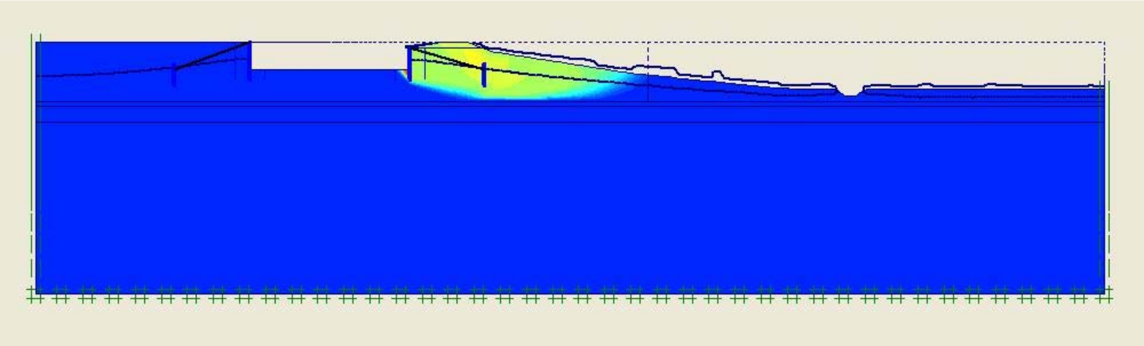

Figure 5.53: Displacement of failure mechanism following phase 3 of DL model

Figure 5.54: Deviatoric strain invariant distribution of failure mechanism following phase 3 of DL model

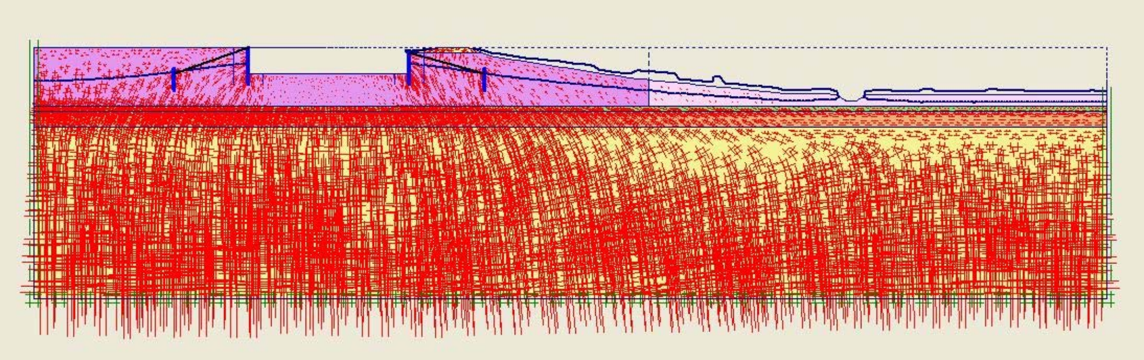

Figure 5.55: Effective stress distribution at the end of phase 3 of DM model

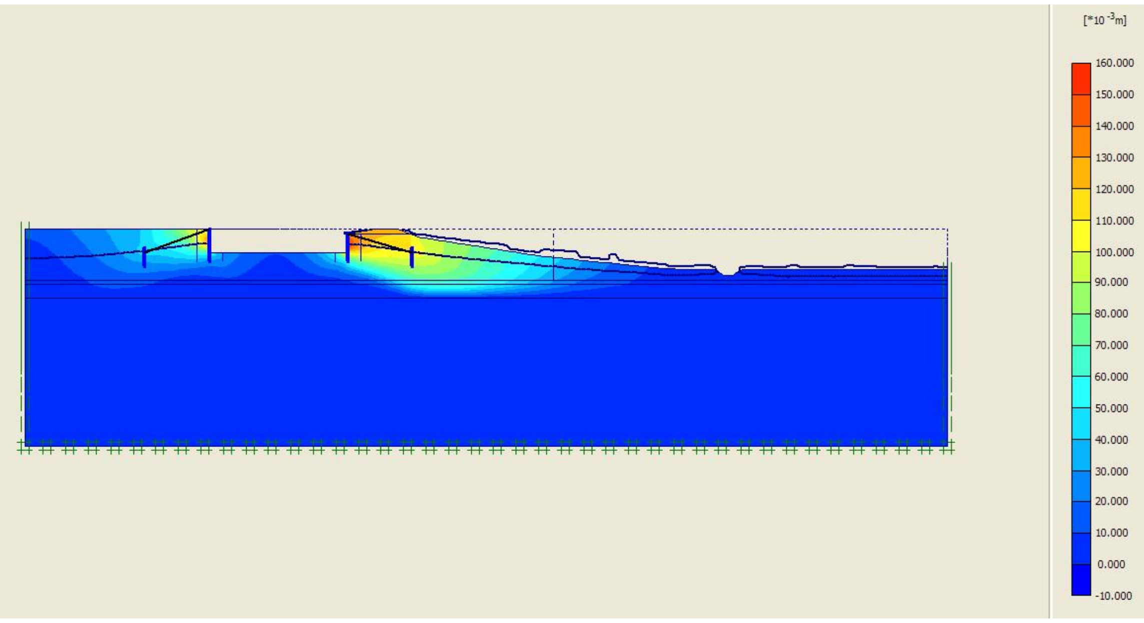

Figure 5.56: Displacements after drought of DM model

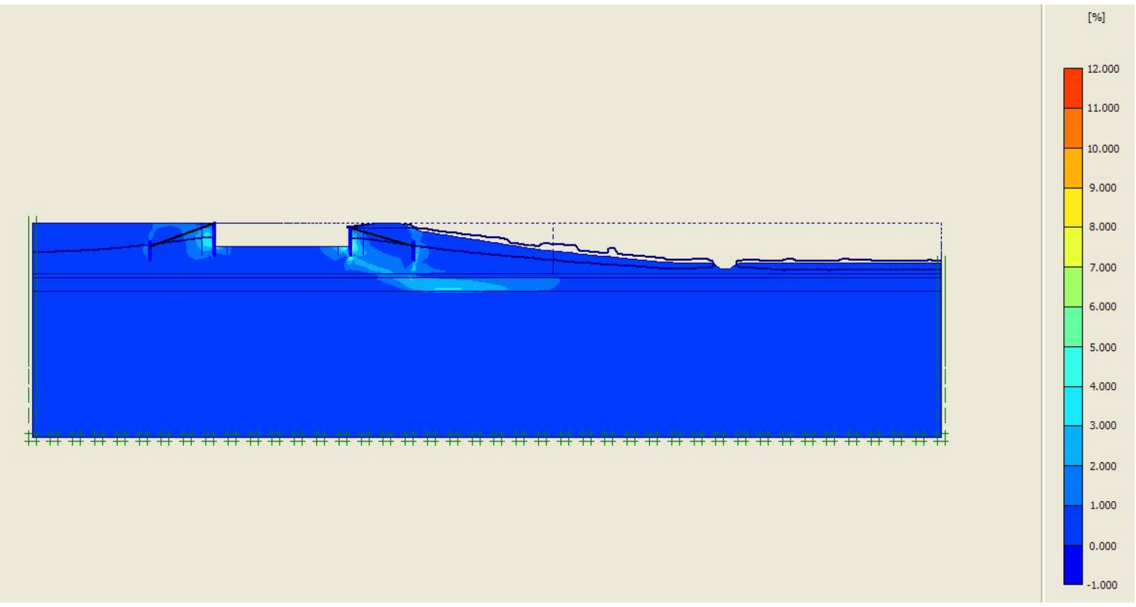

Figure 5.57: Shear strain invariants after drought of DM model

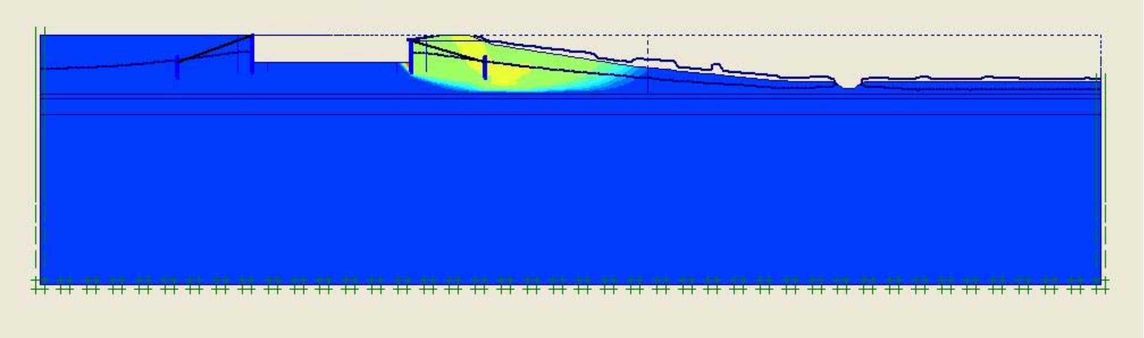

Figure 5.58: Displacement of failure mechanism following phase 3 of DM model

Figure 5.59: Deviatoric strain invariant distribution of failure mechanism following phase 3 of DM model

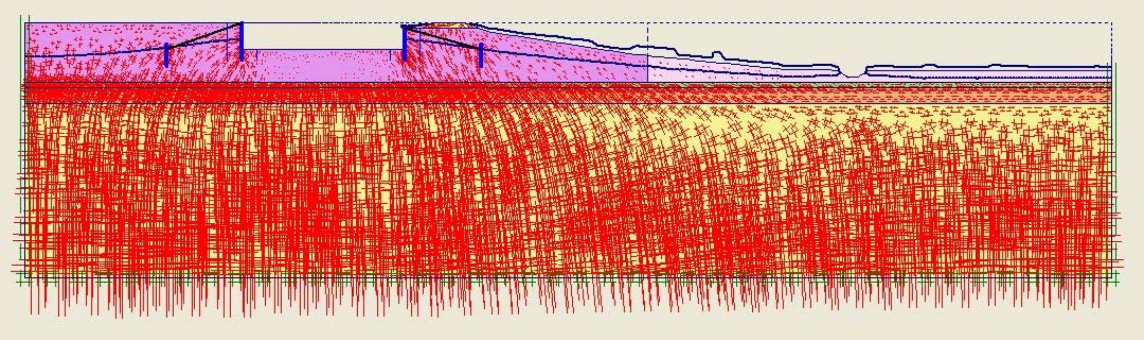

Figure 5.60: Effective stress distribution at the end of phase 3 of DH model

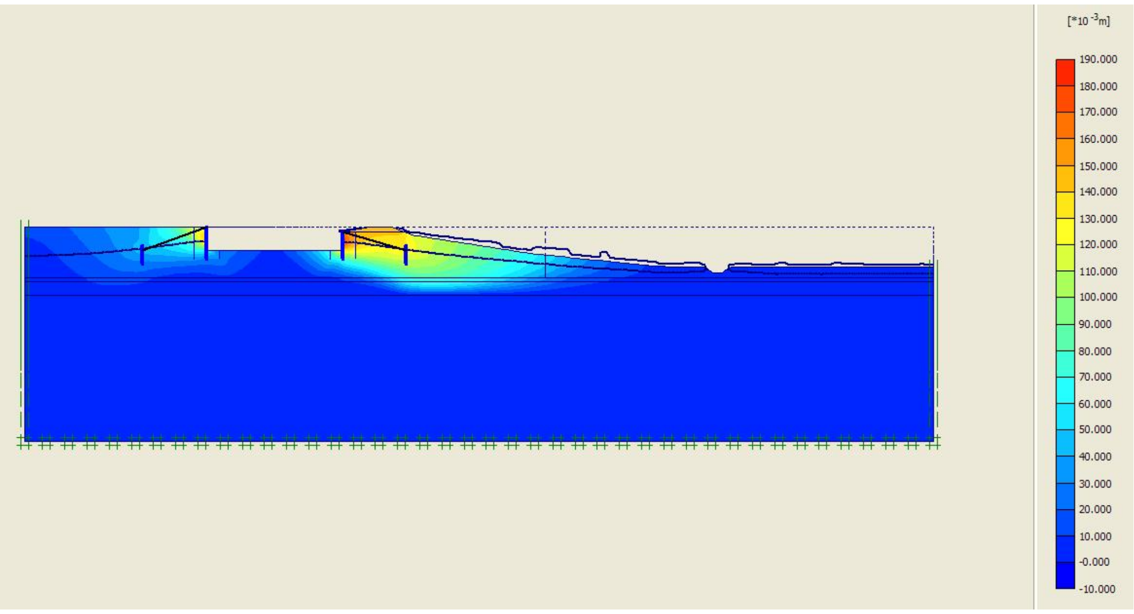

Figure 5.61: Displacements after drought of DH model

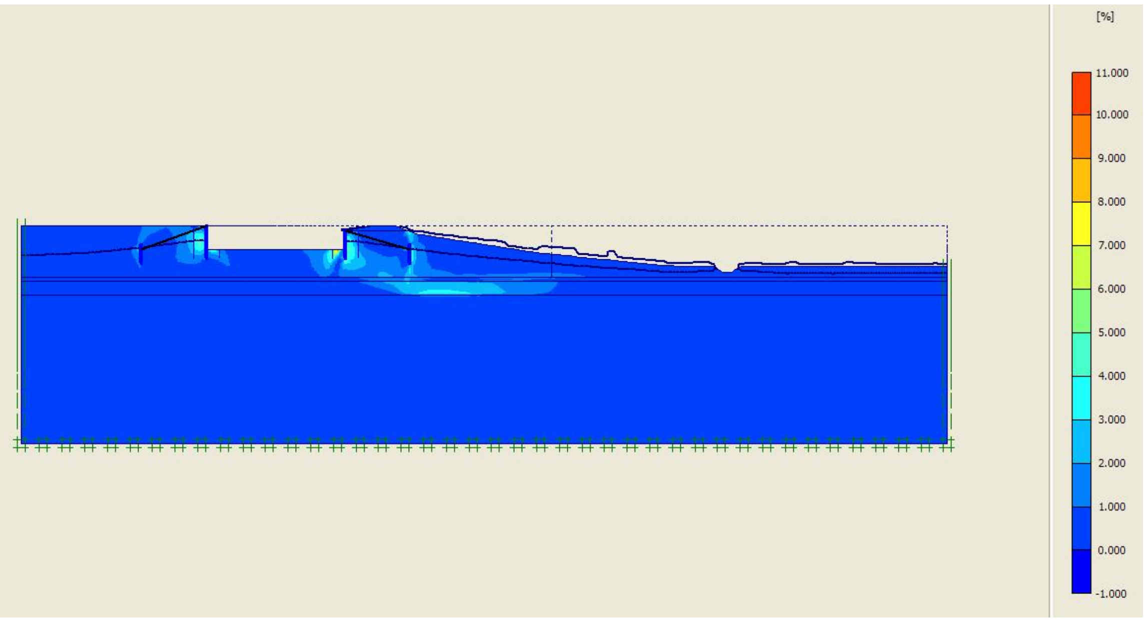

Figure 5.62: Shear strain invariants after drought of DH model

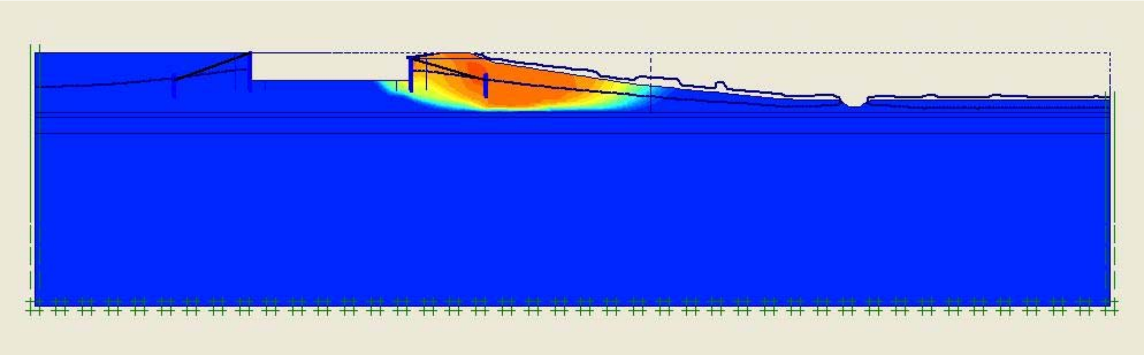

Figure 5.63: Displacement of failure mechanism following phase 3 of DH model

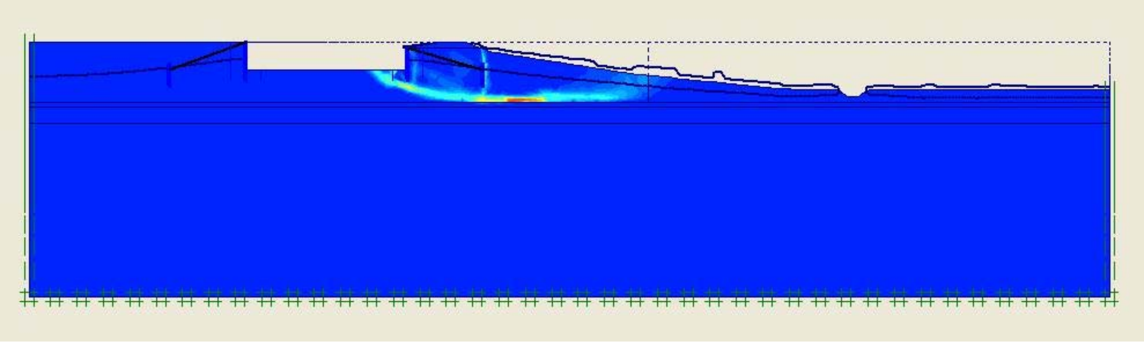

Figure 5.64: Deviatoric strain invariant distribution of failure mechanism following phase 3 of DH model

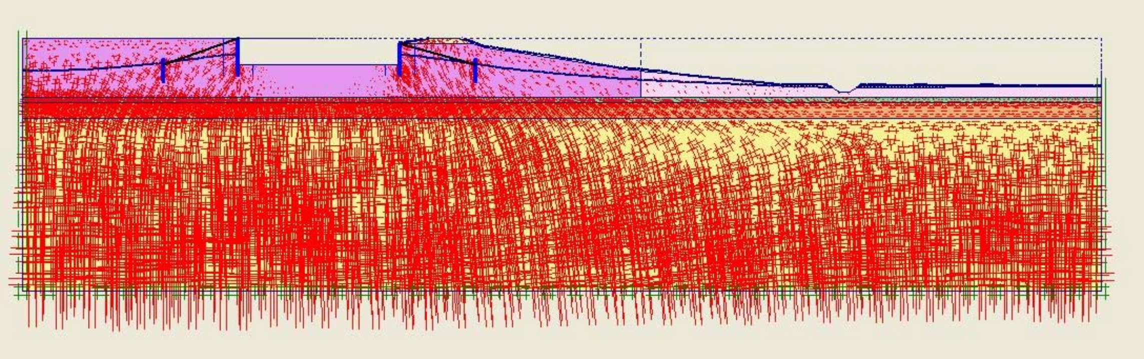

Figure 5.65: Effective stress distribution at the end of phase 3 of IL model

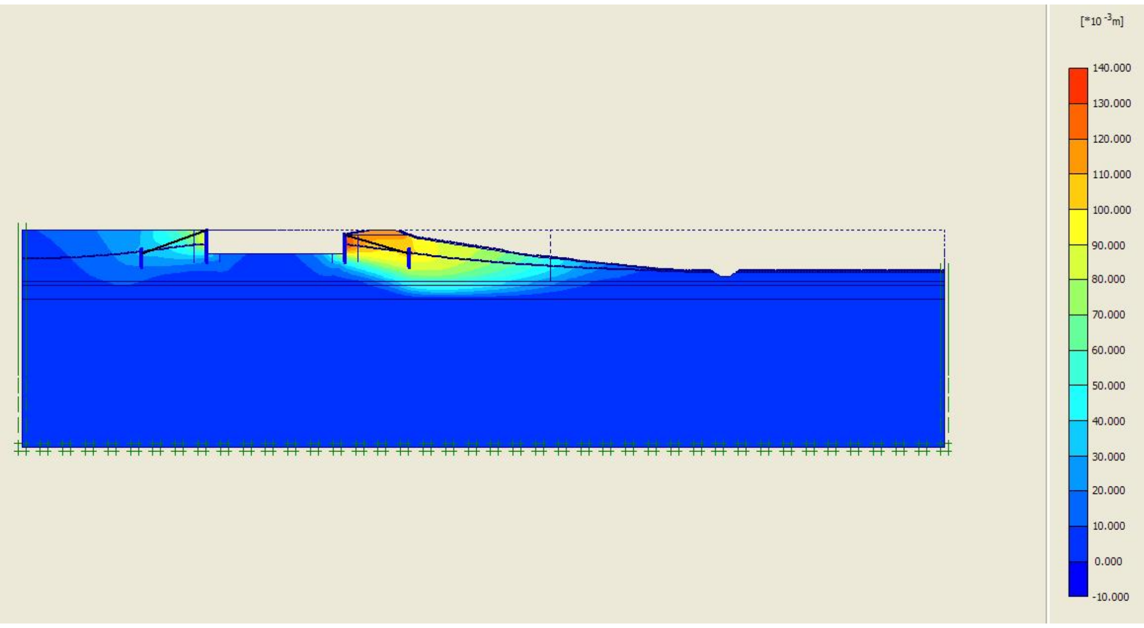

Figure 5.66: Displacements after drought of IL model

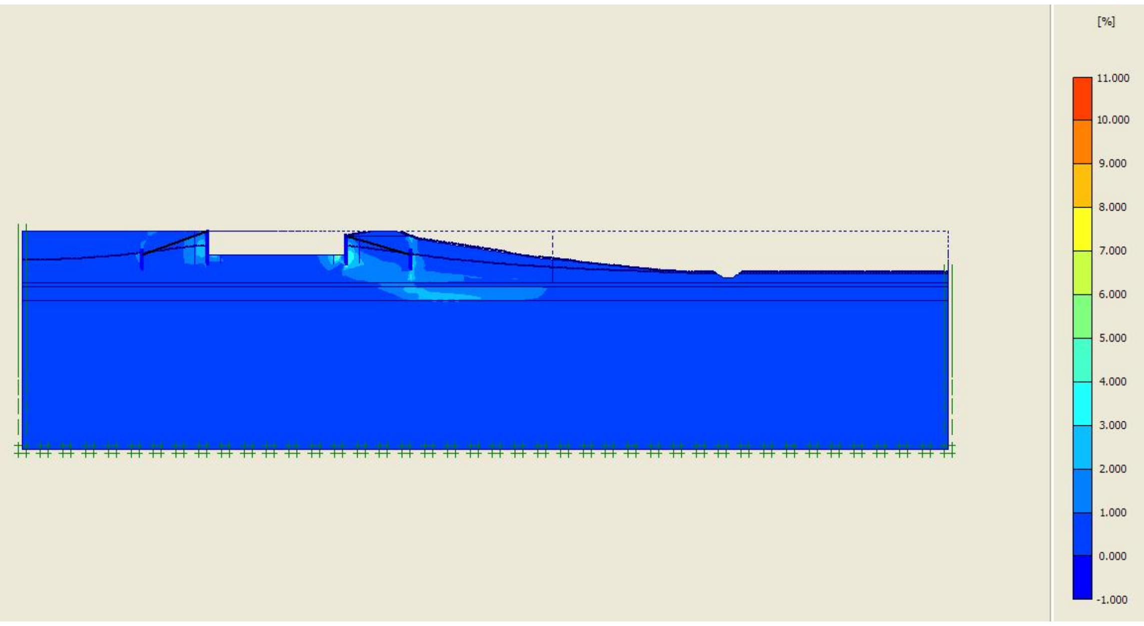

Figure 5.67: Shear strain invariants after drought of IL model

It should be noted that failure occurred only in the intermediate case with low strength (IL model). The realised time for failure in the IL model is just 0.15 days (out of 60 that is the entire drought period set in Plaxis). The fact that failure time is so small leads to disbelief about the soundness of this model which can be attributed to a possible numerical error in Plaxis. Furthermore no “phi-c reduction” analysis was possible to be performed for this model therefore no related results are displayed here.

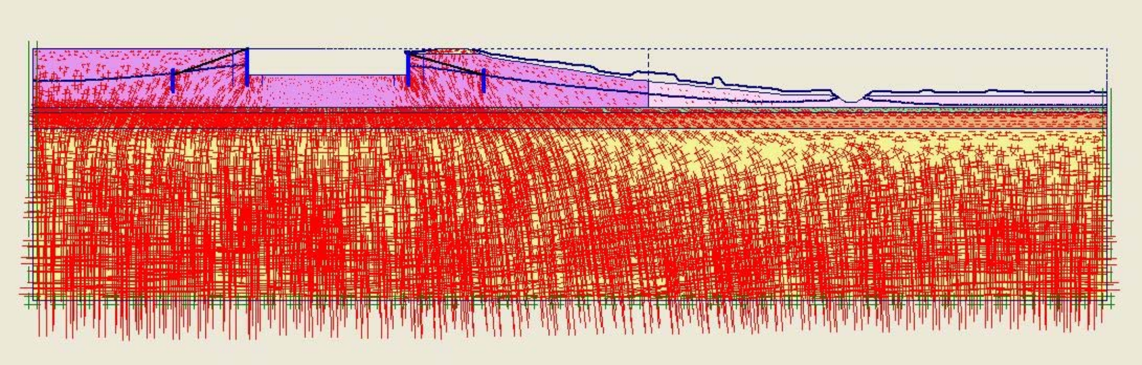

Figure 5.68: Effective stress distribution at the end of phase 3 of IM model

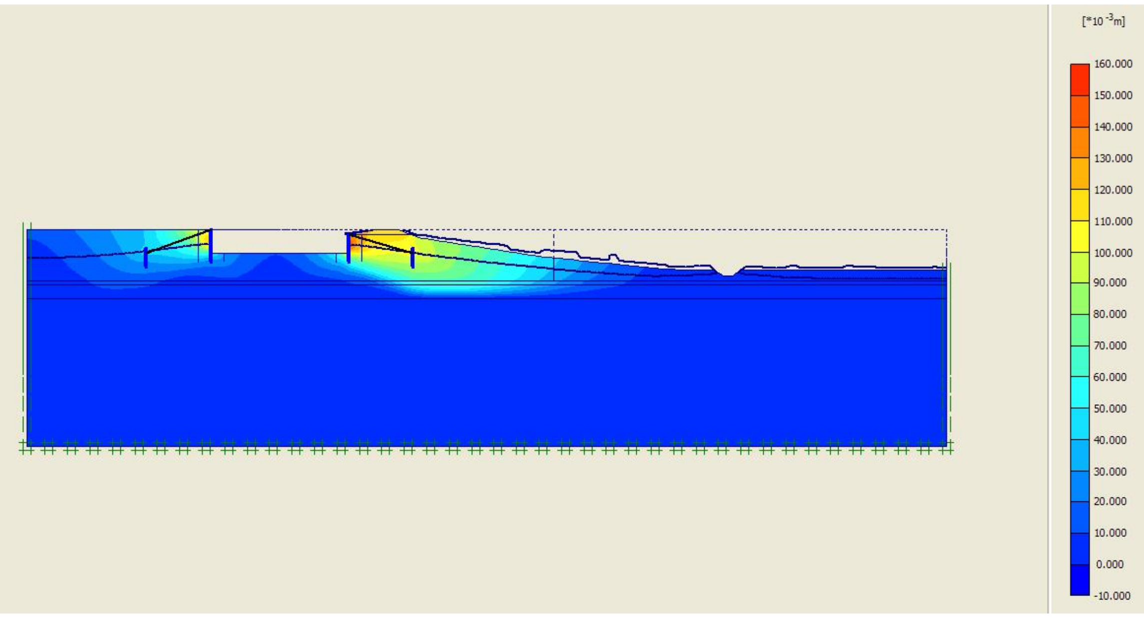

Figure 5.69: Displacements after drought of IM model

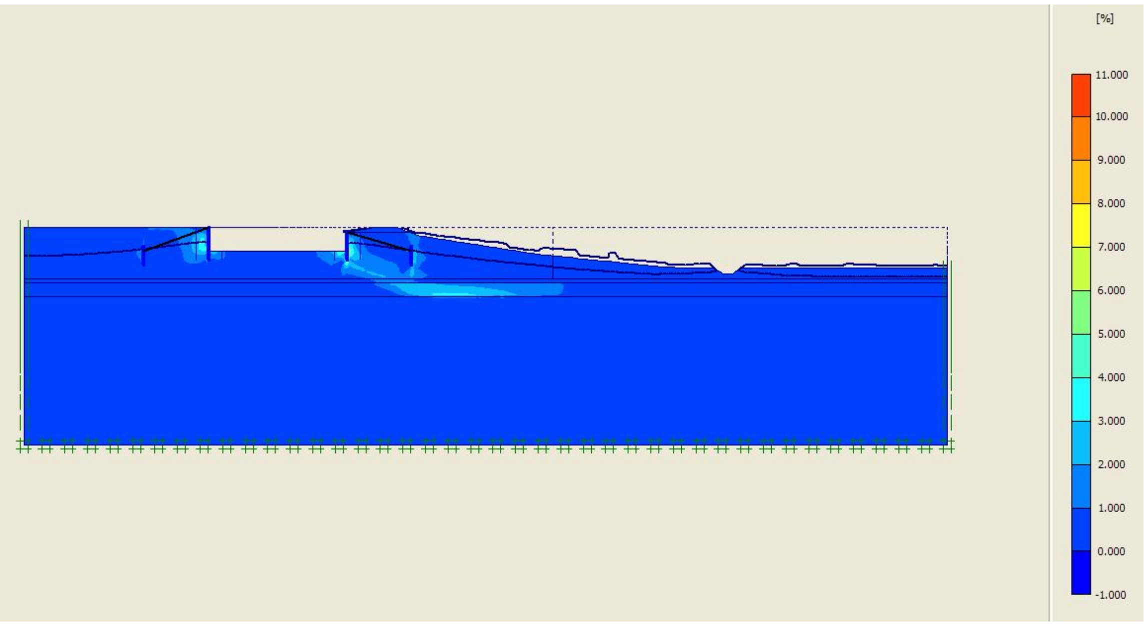

Figure 5.70: Shear strain invariants after drought of IM model

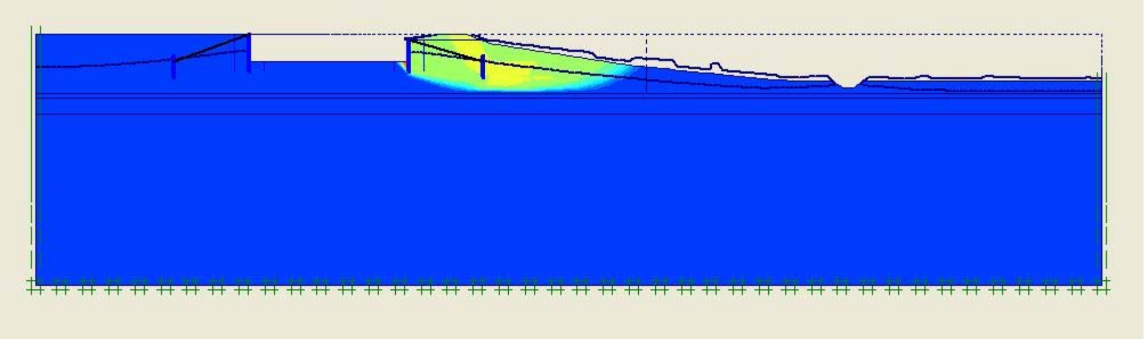

Figure 5.71: Displacement of failure mechanism following phase 3 of IM model

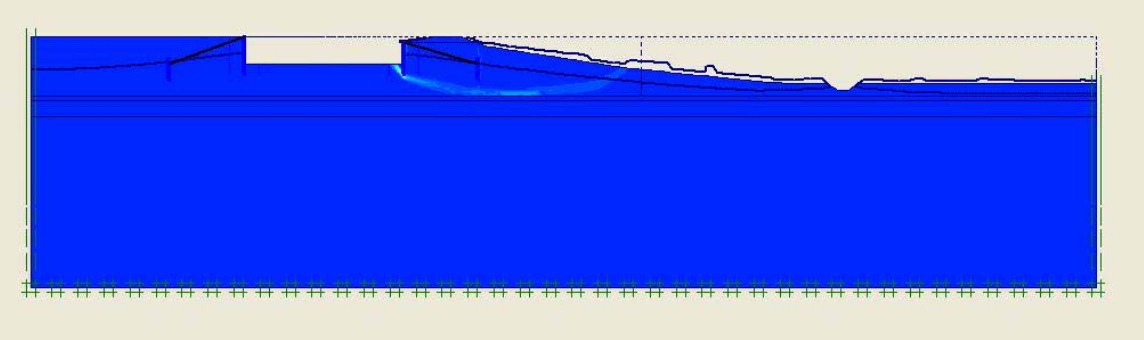

Figure 5.72: Deviatoric strain invariant distribution of failure mechanism following phase 3 of IM model

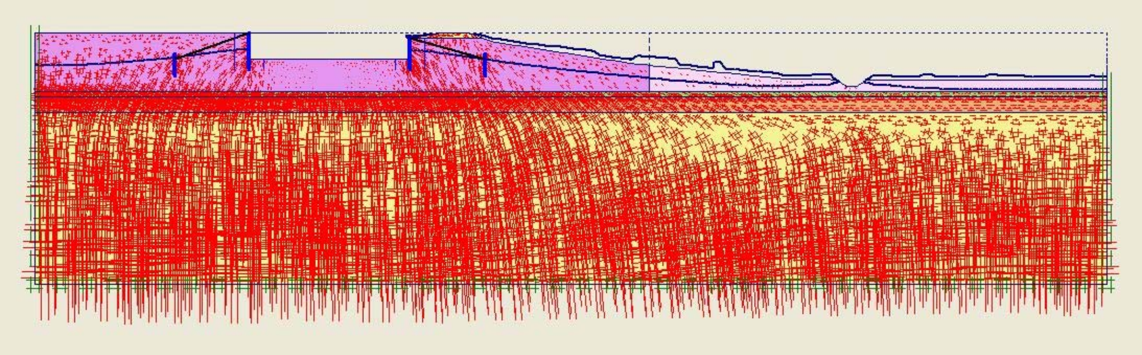

Figure 5.73: Effective stress distribution at the end of phase 3 of IH model

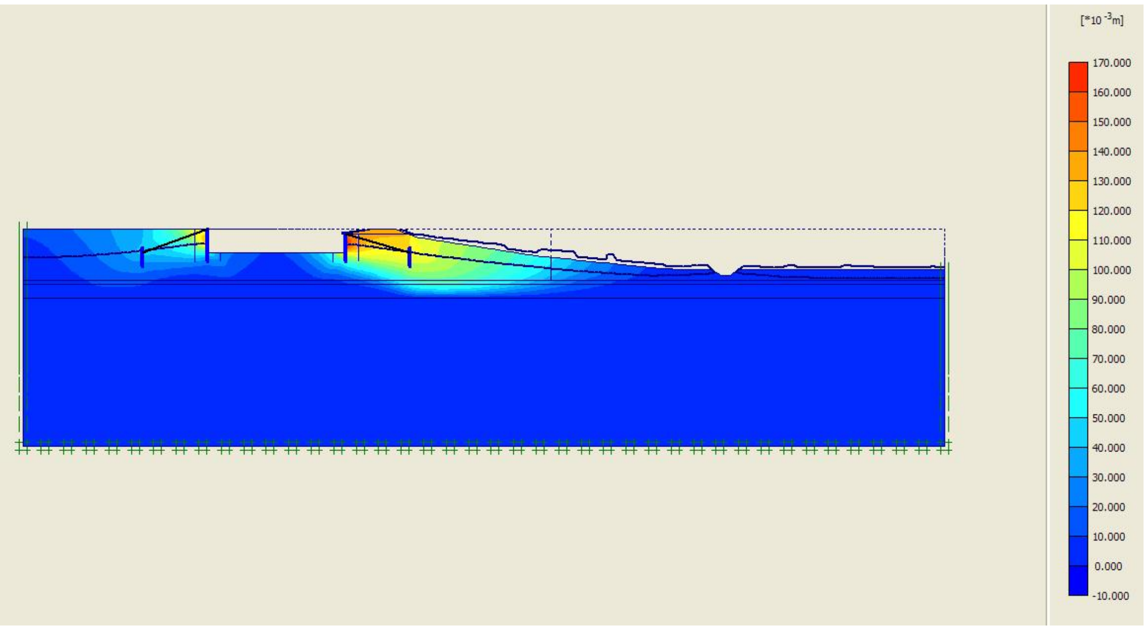

Figure 5.74: Displacements after drought of IH model

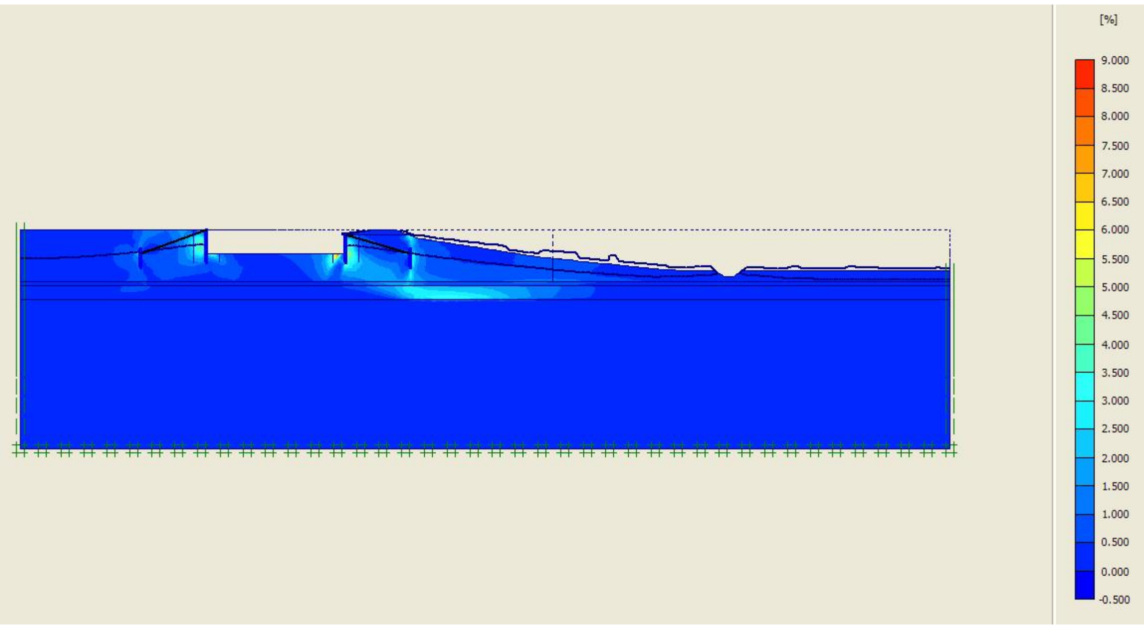

Figure 5.75: Shear strain invariants after drought of IH model

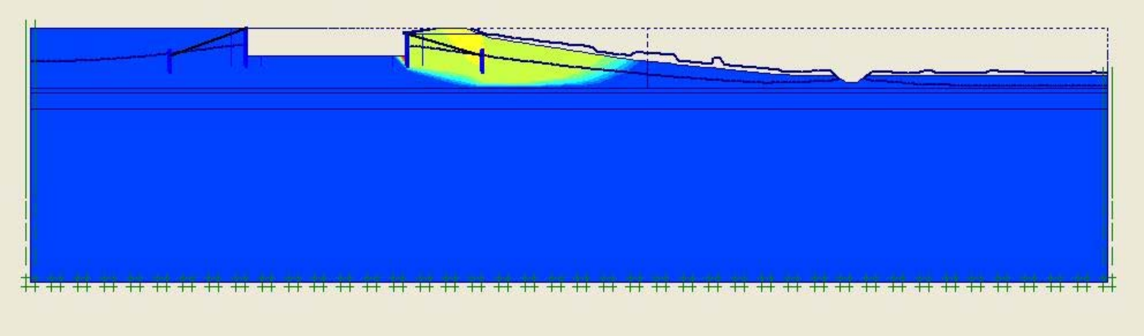

Figure 5.76: Displacement of failure mechanism following phase 3 of IH model

Figure 5.77: Deviatoric strain invariant distribution of failure mechanism following phase 3 of IH model

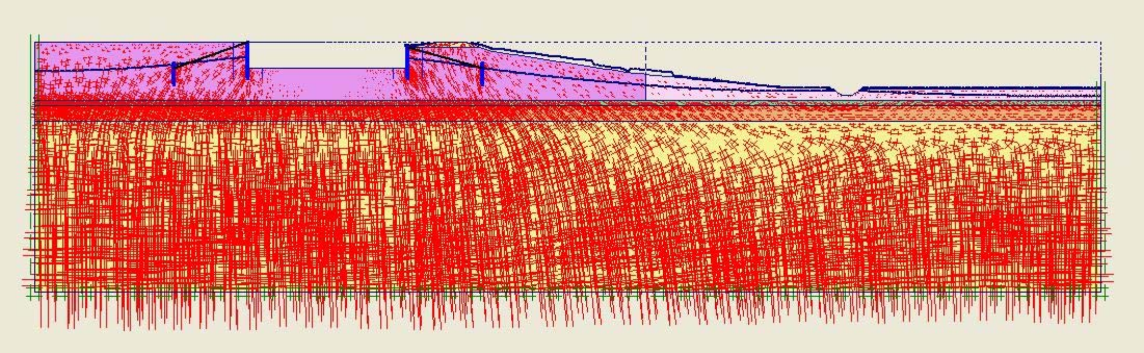

Figure 5.78: Effective stress distribution at the end of phase 3 of WL model

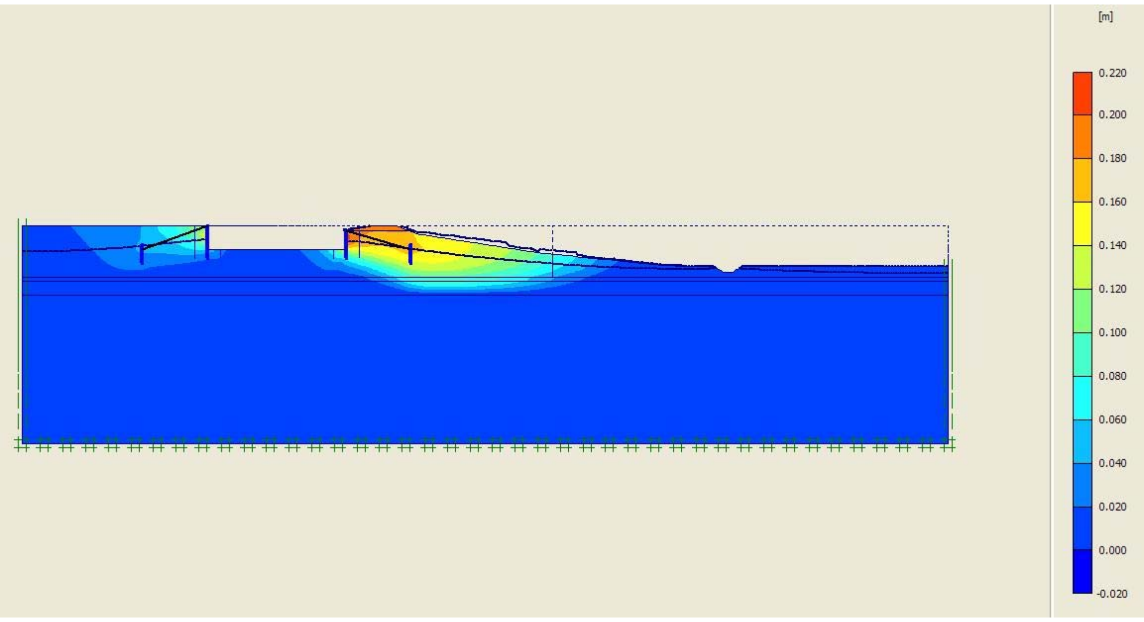

Figure 5.79: Displacements after drought of WL model

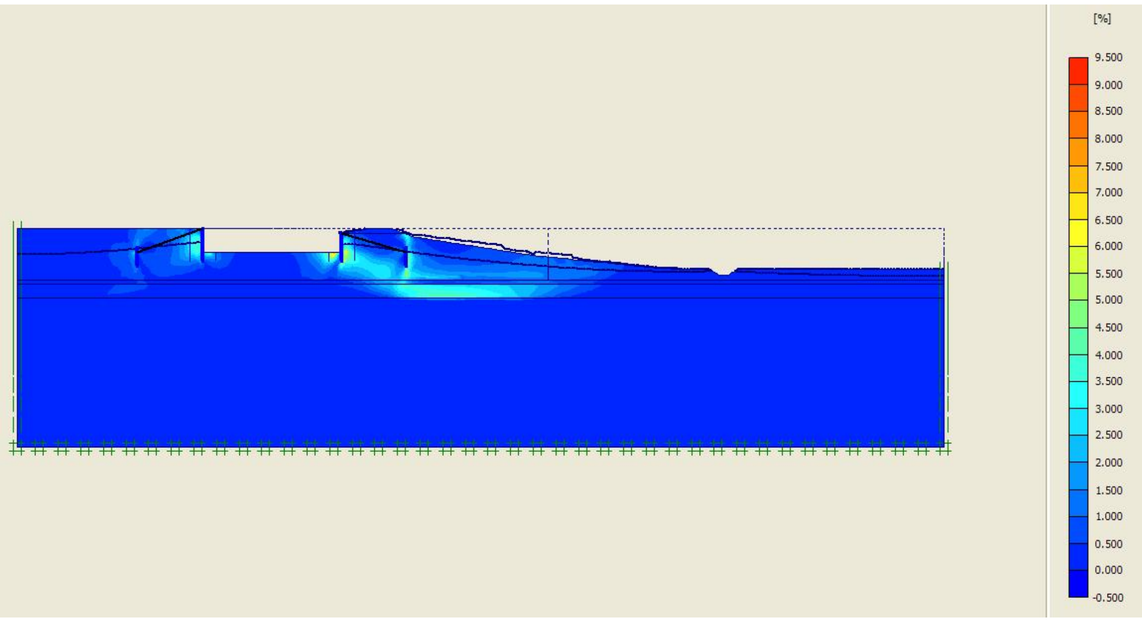

Figure 5.80: Shear strain invariants after drought of WL model

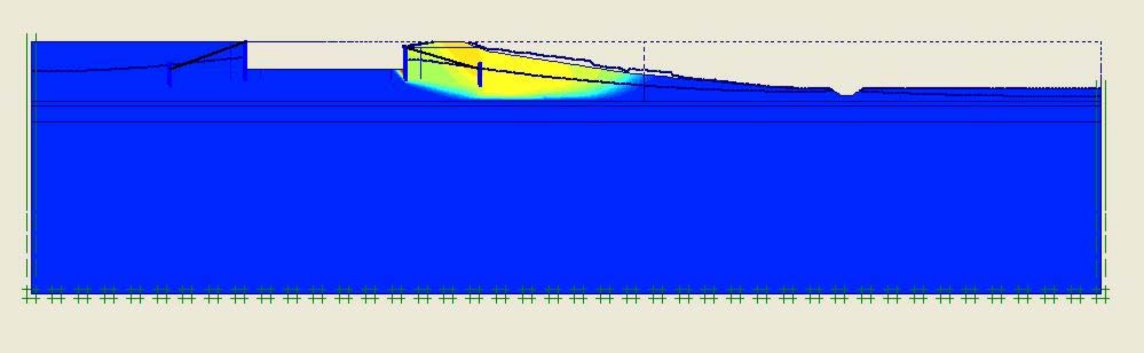

Figure 5.81: Displacement of failure mechanism following phase 3 of WL model

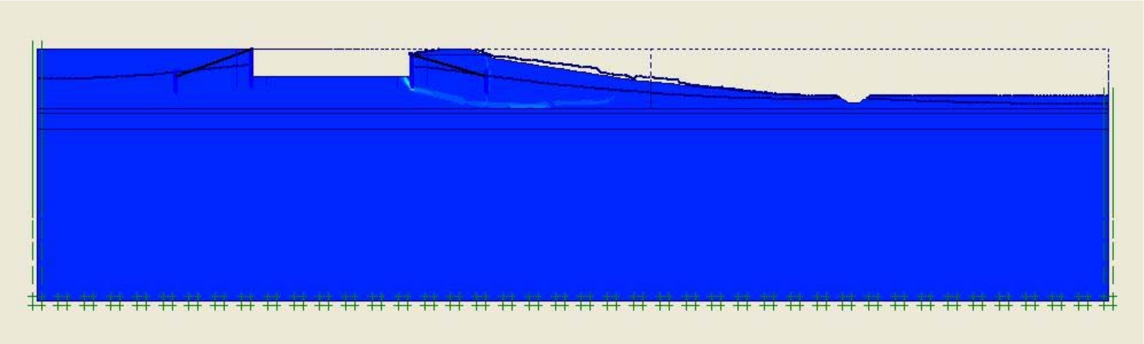

Figure 5.82: Deviatoric strain invariant distribution of failure mechanism following phase 3 of WL model

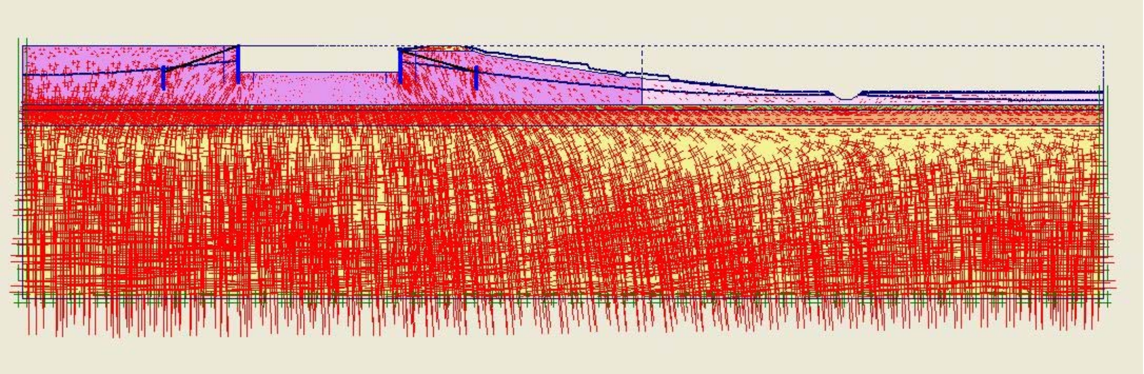

Figure 5.83: Effective stress distribution at the end of phase 3 of WM model

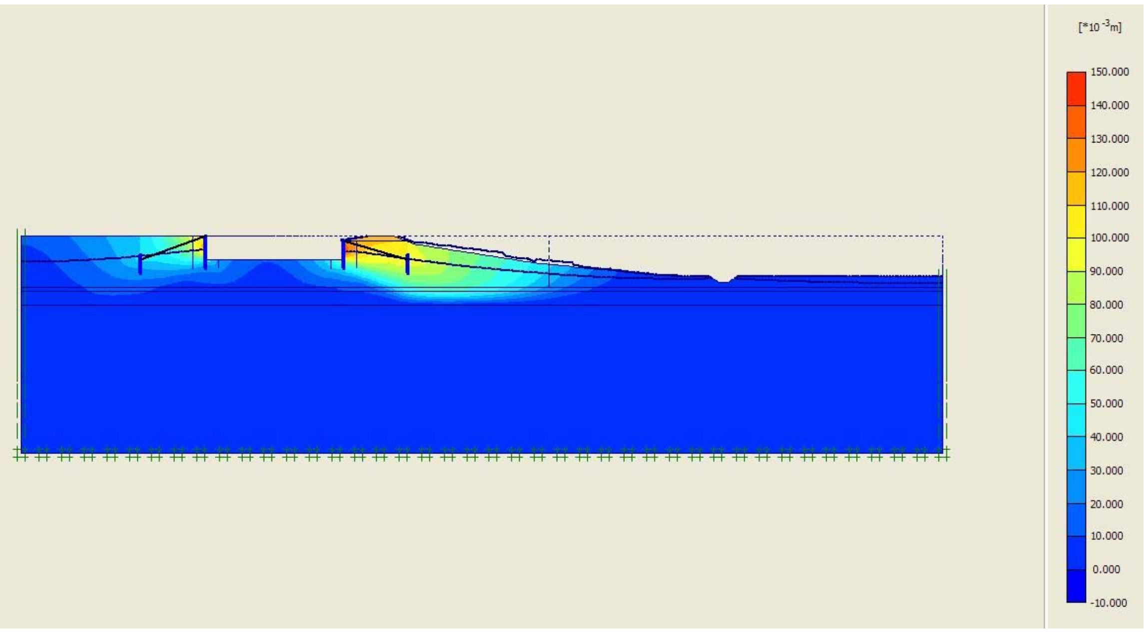

Figure 5.84: Displacements after drought of WM model

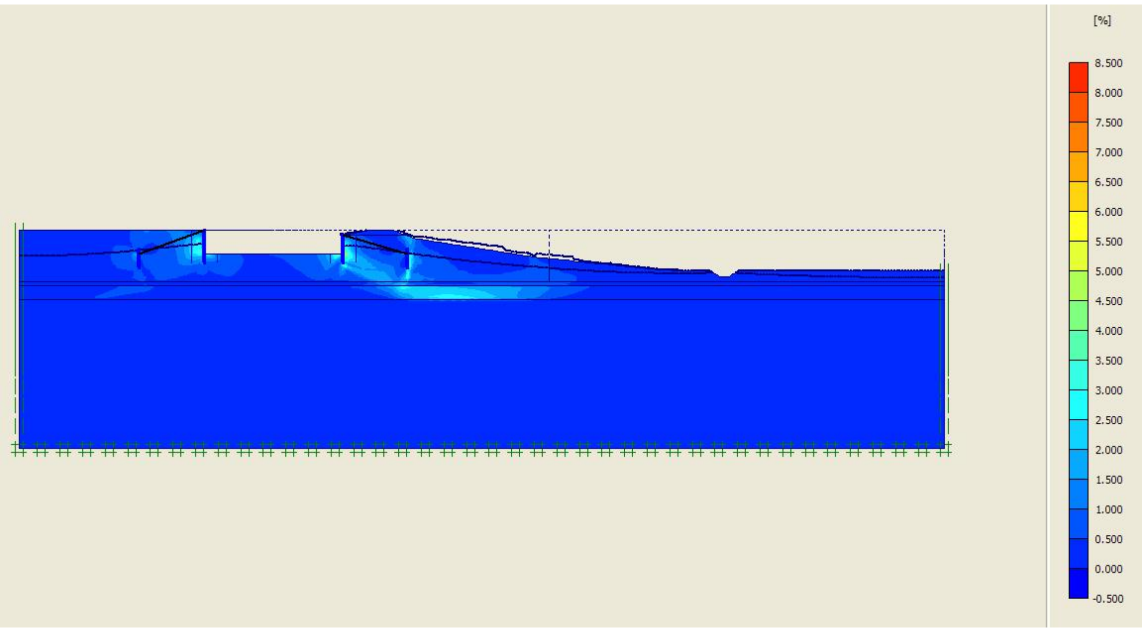

Figure 5.85: Shear strain invariants after drought of WM model

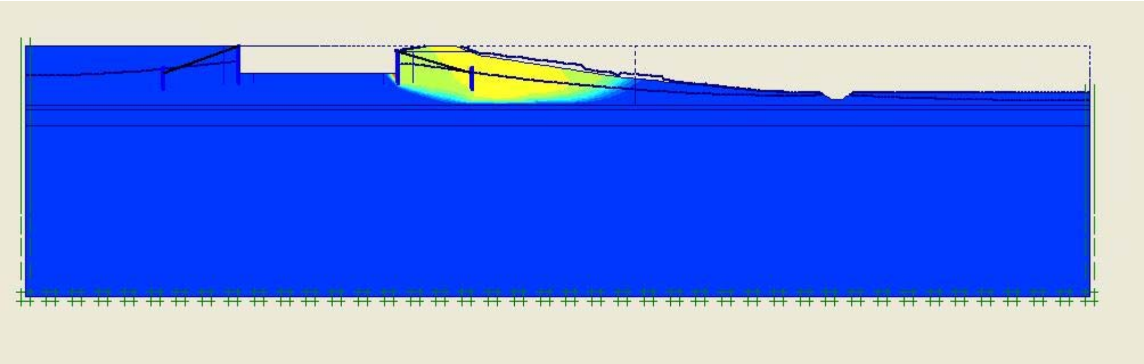

Figure 5.86: Displacement of failure mechanism following phase 3 of WM model

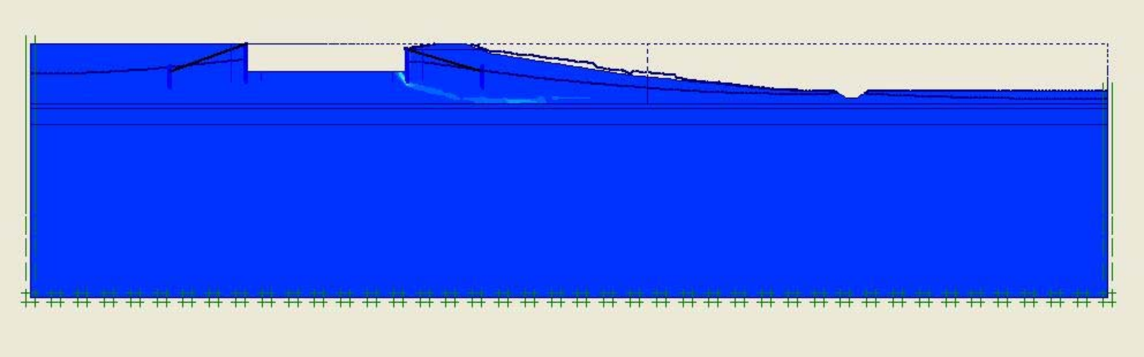

Figure 5.87: Deviatoric strain invariant distribution of failure mechanism following phase 3 of WM model

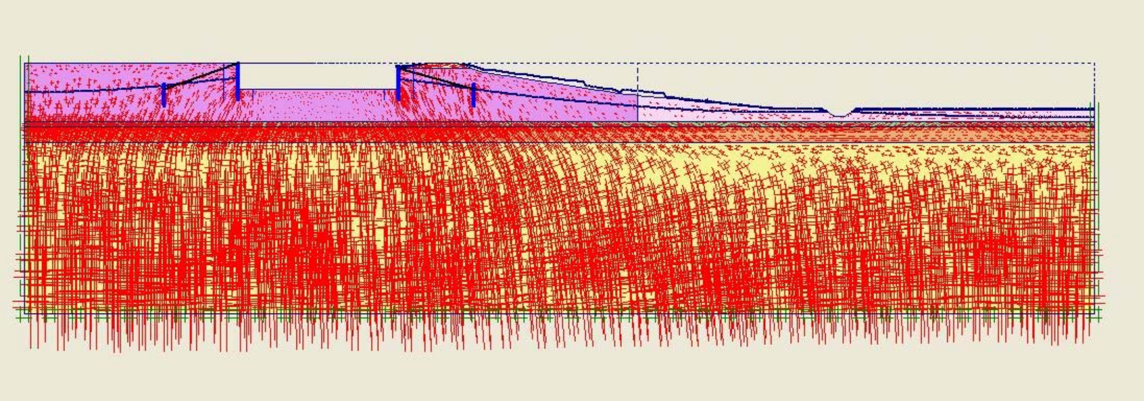

Figure 5.88: Effective stress distribution at the end of phase 3 of WH model

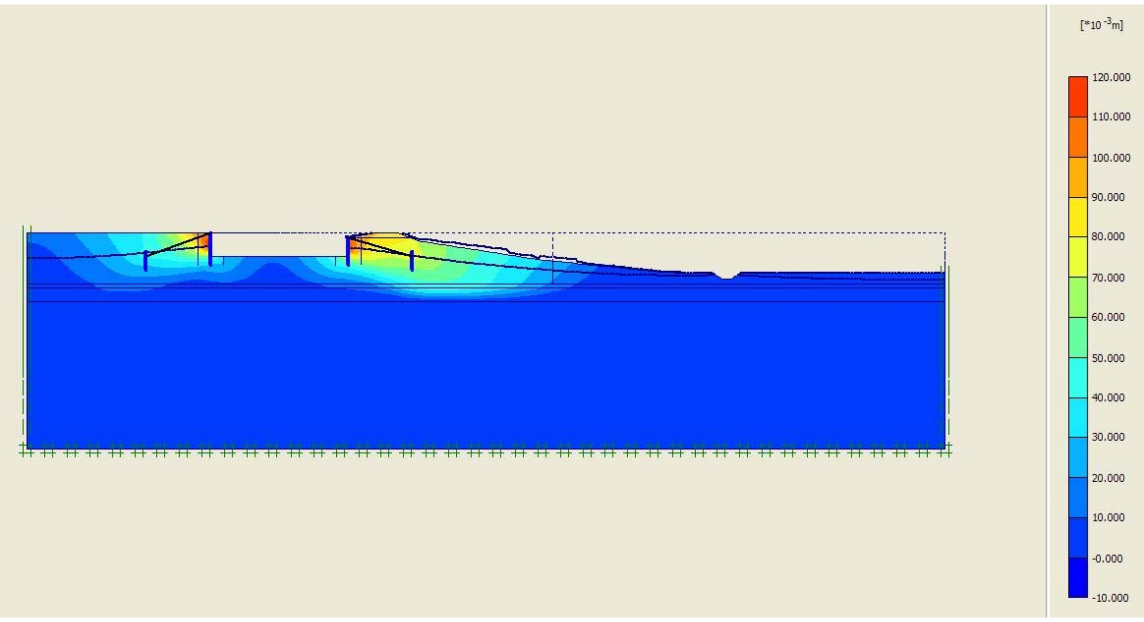

Figure 5.89: Displacements after drought of WH model

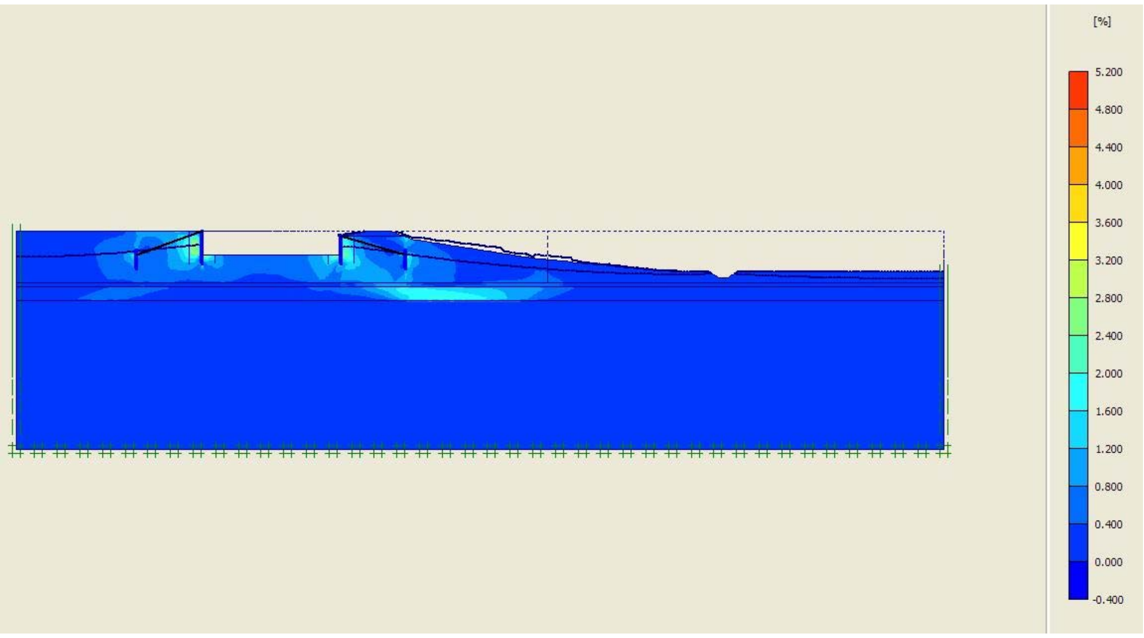

Figure 5.90: Shear strain invariants after drought of WH model

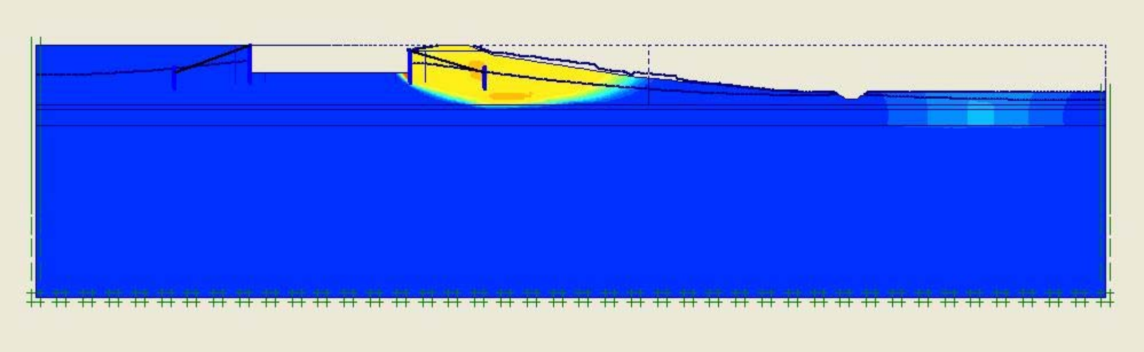

Figure 5.91: Displacement of failure mechanism following phase 3 of WH model

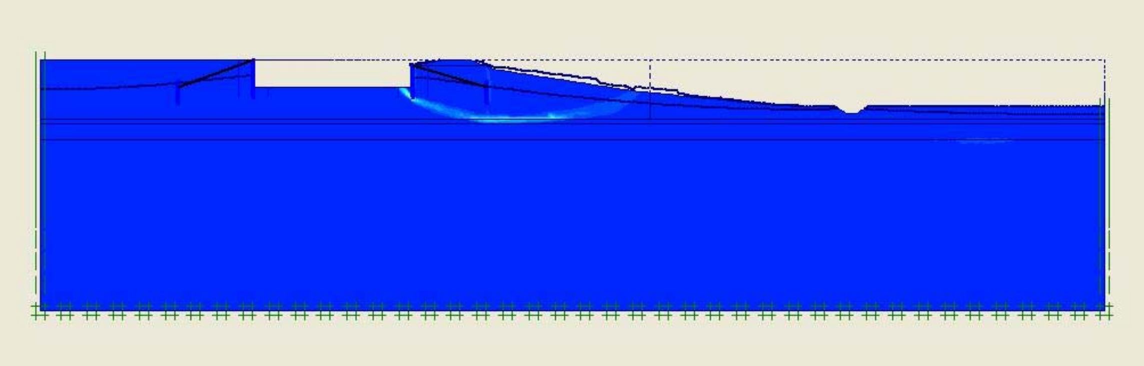

Figure 5.92: Deviatoric strain invariant distribution of failure mechanism following phase 3 of WH model

Below in tables 5.6 to 5.8 the accumulated results of the main values can be found. Namely, table 5.6 contains the maximum displacement increment for all 9 models, table 5.7 contains the maximum incremental deviatoric strain invariant and table 5.8 the safety factors following phase 3.

Parameter values	Maximum displacement increments (cm)		
	Dry	Intermediate	Wet
$mean-\sigma/4$	23.7	13.6	21.0
$mean$	15.7	15.4	14.1
$mean+\sigma/4$	17.4	16.4	11.7

Table 5.6: Maximum displacement increments for all 9 models at end of phase 3

Parameter values	Maximum incremental deviatoric strain invariants (%)		
	Dry	Intermediate	Wet
$mean-\sigma/4$	19.73	10.91	9.29
$mean$	11.47	11.62	8.35
$mean+\sigma/4$	8.26	7.10	5.01

Table 5.7: Maximum incremental deviatoric stain invariants for all 9 models at end of phase 3

Parameter values	Safety factors at end of phase 3		
	Dry	Intermediate	Wet
$mean-\sigma/4$	1.56	-	1.47
$mean$	1.53	1.78	1.16
$mean+\sigma/4$	2.22	1.96	2.76

Table 5.8: Safety factors for all 9 models following phase 3

The calculated maximum displacements as indicated in table 5.6 are inconsistent for the intermediate saturation case with the maximum displacement decreasing with decreasing strength. Furthermore for the dry case inconsistencies can be observed for mean and maximum parameter values.

From table 5.7 the results seem more logical with the maximum deviatoric strain invariant increasing with decreasing parameter values and decreasing saturation. Only for the intermediate case and mean parameter values the results are inconsistent.

The safety factors according to table 5.8 are very inconsistent while for the intermediate saturation case and low parameter values no results could be obtained at all.

Apparently this parameter study does not lead to any consistent results and consequently should be considered as completely unreliable.

6 Evaluation

The research was based on the soil investigation performed by GeoDelft. The investigation included both field and laboratory data. In more detail the field data consisted of 67 CPTs (Cone Penetration Tests) and 48 Borings while the laboratory data counted 15 Ko-CRS tests, 12 Triaxial tests and 13 Simple Shear tests. The field data were used to comprise the stratification of the soil and the laboratory data for the determination of the soil parameters.

The amount of field data is considered adequate but their dispersion over about 1700m along the dike reduces their usefulness because the breach was obviously a local phenomenon. Furthermore there is a large number of borings and CPTs performed directly on the breached area which consists naturally of highly disturbed soil. The interpretation of these data (see paragraph 3.2) leads to results with decreased reliability. The intact soil in the vicinity of the breach has been investigated with only 2 CPTs and no borings thus rendering it at least very difficult to get reliable data about the stratification of the subsoil of the dike. More investigation of the region near the failure would greatly have increased the quality of the results.

The amount of laboratory data is not considered as adequate to lead to a statistically sound evaluation of the soil properties. Their practicability is further degraded by the fact that the samples tested in the laboratory came from borings at a minimum distance of 250m going up to even 700m from the breach.

The geometry of the surface was measured by GeoDelft and was used along with the estimated stratification to create the model to be analysed by Plaxis and PlaxFlow. For the properties of the structural elements (sheet pile wall and anchors) estimated values were used. There were 3 calculation phases defined, the first 2 phases were aimed at arriving at the stress state in the dike at the beginning of the dry summer of 2003 and the third one involved the analysis of the desiccation and deformation due to the drought. Drought results in evapotranspiration of water from the ground which is a very complicated procedure. In this study it was simulated in a simple way by prescribing an outflow of 5mm of water per day for 60 days from the entire ground surface.

The results of the groundwater flow analyses, performed by PlaxFlow, appear normal and more or less as expected for all 9 models. The only inconsistency was in the dry case after drought where the level of the groundwater table was found higher than the expected one leading to suspicion about the accuracy of the specific calculation and therefore was replaced by extrapolated values based on the other cases analysed (see table 5.2).

The results of the Plaxis deformation and stability analyses for the 9 models with different properties (strength and permeability) produced similar results in terms of overall behaviour. The values for maximum displacement of each of the models were quite inconsistent, specially for the intermediate saturation cases, where with increasing strength also displacement increases (see table 5.6). The wet cases with varying strengths produced logical results with displacements decreasing as the strength increases.

The distributions of the maximum shear strains invariants seem more consistent as they show a decrease in the values of maximum shear strain as the strength increases (see table 5.7). The only inconsistency of these results is in the intermediate saturation case and with mean strength, where the maximum shear strain calculated is larger than the intermediate saturation case with reduced strength.

The resulting figures in paragraph 5.6 show that all 9 models show similar behaviour. The effective stresses are almost identical. Maximum displacements occur at the top of the right sheet pile wall as to be expected with considerable displacements reaching as deep as the basis peat layer. In the figures displaying the shear strain invariants after drought maximum shear strain is observed at the toe of the right sheet pile wall. This is probably were failure starts. The zone with high shear strain invariants starting from that point goes downwards with an inclination of about 45^0 to the horizontal and becomes horizontal in the basis peat layer. However the resulting figures for the safety factor analyses performed for each model show displacements concentrated above the clay layer, therefore only in the Holland peat layer, reaching in length about half of the slope of the dike. The zone of high deviatoric strain invariants for the safety factor analyses begins at the toe of the right sheet pile wall, goes downwards with and angle of about 20^0 and becomes horizontal just above the clay layer so still in Holland peat. Consequently there is a significant difference between the calculated deformation pattern after drought and the failure calculation following drought. The position of the failure plane occurs above the clay layer (in Holland peat) while the earlier deformation pattern due to drought occurs in the basis peat. Unfortunately the forensic evidence taken after the breach, including photographs of the breached area (see paragraph 2.1), is not clear enough to firmly decide about the quality of the location of the calculated failure zone.

From the 9 models analysed only one of them failed (intermediate case with low strength, IL model) during phase 3 (drought) in contrast to what was expected beforehand. The fact that failure of this model occurred only after 0.15 days of drought creates a great deal of doubt about the quality of this calculation.

The safety factors were determined with separate calculations for both the end of phase 2 and 3. The safety factors at the end of phase 2 for all 9 models show results that are not believed to be accurate. In 2 of the models the safety factor calculated by Plaxis is below 1.00, which implies failure, although these models were also found to be stable in the stability calculation (see table 5.5). The wet cases with different strengths are the only safety factor results that seem to be more consistent leading to increasing safety factors with increasing strength. The resulting safety factors of phase 3 are also inconsistent with the 3 models with mean strength and varying permeabilities exhibiting the lowest safety factors. Also the values of some of these safety factors are very high in the 3 cases of high strength models with values around or even higher than 2.00 (see table 5.8). Furthermore when comparing the safety factors of phase 2 with the ones of phase 3 it is observed that the safety factors of phase 3 are higher than the ones of phase 2 for the corresponding models in all cases except one. This renders the overall results of the safety factor calculations completely unrealistic and untrustworthy.

7 Conclusions and Recommendations

Conclusions

- Failure in a manner compatible to the forensic evidence collected at the breached area was not possible to be simulated within a parametric study.

- All the models analysed showed maximum shear strains near the toe of the right sheet pile wall. The analyses of deformation due to drought showed a band of large distortional strains developing within the basis peat layer. The final failure analyses following drought showed a mechanism with a thin band of significant distortional strains in the Holland peat, just above the clay layer.

- The safety factor analyses performed generated inconsistent results that are not believed to be trustworthy.

- The simulation of drought with outflow of water from the ground surface produced realistic results in terms of groundwater flow and regions of unsaturation.

Recommendations

- The field investigation could have been better by performing more tests in the intact soil close to both sides of the failed soil volume.

- The groundwater head of the deep sand layer was measured at NAP-6.00m with a standard deviation of 4cm. The effect of this deviation was not taken into account but could have a serious impact on the results and should be investigated further.

- In order to achieve realistic results the presented uncoupled analyses with subsequent phases of groundwater flow and deformation and stability should be improved by coupling both aspects within one coherent analysis

8 References

BOOKS

[1] MacFarlane, I.C. (ed.) (1969), “Muskeg Engineering Handbook”, University of Toronto Press.

[2] Noto, S. (1991), “Peat Engineering handbook”, Civil Engineering Research Institute of Hokkaido Development Bureau.

[3] Yanagisawa, Moroto & Mitachi (eds) (1999), “Problematic soils Vol. 1, Peats and organic soils”, Balkema, Rotterdam.

[4] C.W.W. Ng, L.M. Zhang, Y.H. Wang (2006), “Physical Modeling in Geotechnics – 6th ICPMG ‘06”, Taylor & Francis Group, London, UK.

THESES

[5] Thomas, S.D. (1987), “The consolidation behaviour of gassy soils”. PhD Thesis.

[6] Den Haan E.J. (1994) “Vertical compression of soils”. PhD Thesis TU Delft.

[7] Zwanenburg, C. (2005), “The influence of anisotropy on the consolidation behaviour of peat”. PhD thesis TU Delft.

[8] Havel F. (2004), “Creep in soft soils”, PhD Thesis Norwegian University of Science and Technology.

[9] Kanning W. (2005), “Safety format and calculation methodology slope stability of dikes”, MSc Thesis TU Delft.

[10] De Jong, A. K. d. (2007). “Modelling peat dike stability. Back-analysis of Direct Simple Shear results”. Department of GeoSciences, Engineering Geology. Delft University of Technology. M.Sc.: 264.

PAPERS

[11] Hobbs N.B. (1986), “Mire morphology and the properties and behaviour of some British and foreign peats”, Quarterly Journal of Engineering Geology, Geological Society Publishing House, pages 7-80.

[12] Dyvik R., Berre T., Lacasse S. & Raadim B. (1987), “Comparison of truly undrained and constant volume direct simple shear tests”, Géotechnique, vol. 37, No 1, pages 3-10.

[13] Pigott, P. T., Hanrahan, E. T, & Somers, N. (1992), “Major canal reconstruction in peat areas”. Proc. Instn. Civ. Engrs. Water Marit. & Energy, Vol. 96, pages 141-152.

[14] Evans M.G., Burt M.G., Holden J., Adamson J.K. (1999), ”Run-off generation and water table fluctuations in blanket peat: evidence from UK data spanning the dry summer of 1995”, Journal of hydrology, vol. 221, n°3-4, Elsevier Science, Amsterdam, pages 141-160.

[15] Holden J., Burt T. P. and Cox N. J. (2001), “Macroporosity and infiltration in blanket peat: the implications of tension disc infiltrometer measurements”, Hydrological Processes, vol. 15, No 2, pages 289-303.

[16] Gould R.A., Bedell Philip R., and Muckle J.G. (2002), “Construction over organic soils in an urban environment: four case histories”, Canadian Geotechnical Journal 39(2), NRC Canada, pages 345-356.

[17] Lafleur Peter M., Hember Robbie A., Admiral Stuart W. and Roulet Nigel T. (2005), “Annual and seasonal variability in evapotranspiration and water table at a shrub-covered bog in southern Ontario, Canada”, Hydrological Processes Vol. 19 No 18, John Wiley & Sons, Ltd, pages 3533-3550.

[18] Cola S. and Cortellazzo G. (2005), “The shear strength behavior of two peaty soils”, Geotechnical and Geological Engineering, Volume 23, No 6, Springer, pages 679-695.

[19] Zwanenburg, C. and Barends F.B.J. (2004), “Anisotropic behaviour vs 3D consolidation of soft soils”, 5th Internationtal PhD Symposium in Civil Engineering, Taylor & Francis, London, pages 1-8.

[20] Warburton J., Holden J., Mills A.J. (2004), ” Hydrological controls of surficial mass movements in peat”, Earth Science Reviews, Volume 67, No 1-2, pages 139-156.

[21] Van Baars, S. (2004), “Peat Dike Failure in the Netherlands”, European Water Management Online, European Water Association (EWA), Hennef, Germany, pages 1-11.

[22] Van Baars, S. (2005), “The horizontal failure mechanism of the Wilnis peat dyke”, Géotechnique, Vol. 55 No 4, pages 319-323.

[23] Price J.S., Cagampan J. and Kellner E. (2005), "Assessment of peat compressibility: is there an easy way?", Hydrological Processes Vol. 19 No 17, pages 3469-3475.

[24] Long M., Jennings P. (2005), "Analysis of the peat slide at Pollatomish, CountyMayo, Ireland", Landslides Journal Vol. 3 No 1, Springer, pages 51-61.

[25] Leroueil S. (2006), "Embankments on soft clays", CIGMAT Conference.

[26] Den Haan E.J. & Kruse G.A.M. (2007), "Characterisation and engineering properties of Dutch peats", Characterization & Engineering Properties of Natural Soils Vol. 4, Taylor & Francis Group, London, pages 2101-2133.

[27] Van Baars, S. (2008), "Dutch peat dyke failure during dry summer of 2003", International symposium Drought and Construction.

REPORTS AND OTHERS

[28] Van Esch J.M. (2001), "Groundwater flow module GeoPlax"

[29] R.B.J. Brinkgreve (2002) "Plaxis General Information manual", Balkema, Tokyo.

[30] R.B.J. Brinkgreve (2002) "Plaxis Material Models manual", Balkema, Tokyo.

[31] R.B.J. Brinkgreve (2002) "Plaxis Reference manual", Balkema, Tokyo.

[32] R.B.J. Brinkgreve (2002) "Plaxis Scientific manual", Balkema, Tokyo.

[33] R.B.J. Brinkgreve (2002) "Plaxis Tutorial manual" , Balkema, Tokyo.

[34] R.B.J. Brinkgreve (2002) "Plaxis Validation manual" , Balkema, Tokyo.

[35] GeoDelft report 1 (2003):
Labonderzoek Oorzaak Wilnis kadeverschuiving: sterkte en samendrukkingsproeven, CO-411242-0022-version 01 concept, November 2003

[36] GeoDelft report 2 (2003):
Oorzaak Onderzoek Wilnis - Invloed van gas, temperatuur en andere weersomstandigheden, CO-411242.604-0027- version definitief, December 2003

[37] GeoDelft report 3 (2004):

Kadeverschuiving Wilnis – onderzoek naar de oorzaak van de kadeverschuiving, , CO-411242-0018-version 01 definitief, Januari 2004

[38] GeoDelft report 4 (2004):
Bodemonderzoek naar aanleiding van afschuiven boezemkade te Wilnis-feitelijke rapportage, CO-411242-0030-version 02 definitief, Januari 2004, met 13 bijlagen (3-13 in tweede band)

[39] GeoDelft report 5 (2004):
Achtergrondrapport sterkteonderzoek oorzaak kadeverschuiving Wilnis, CO-411242-0025-version 01 definitief, Januari 2004

[40] GeoDelft report 6 (2004):
Oorzaken onderzoek Wilnis - Deelrapport waarnemingen en Materiaalgedrag, deel 1, CO-411242-0026-version 02 definitief, Januari 2004

[41] GeoDelft report 7 (2004):
Oorzaken onderzoek Wilnis - Achtergrondrapport waarnemingen en materiaalgedrag, deel 2, CO-411242-0026-version 3, Januari 2004

9 Appendices

A. Drawings

Drawing A1: Top view of Wilnis breached area with location of CPTs and borings
Drawing A2: Geotechnical longitudinal profile along crest of dike
Drawing A3: Geotechnical longitudinal profile along slope of dike
Drawing A4: Geotechnical longitudinal profile along toe of dike

B. In situ testing methods description

B.1 General

Following the Wilnis peat dike failure an extensive site investigation was conducted by GeoDelft in the period from the end of August 2003 until the end of October 200B. Since much of the investigation took part directly on the failed area caution was paid in the execution of all tests. In order to get more insight into the soil conditions piezo-cone tests were performed with dissipation tests and the ground was sampled by the Begemann-boring system. Also ground-gas samples and camera-cone tests were taken. For monitoring groundwater levels pore pressure meters were installed in the embankment and the cracks. These pore pressure meters function automatically and all measurements are recorded in GeoDelft's database. Furthermore, monitoring wells, that were manually monitored, were placed.

B.2 Electrical probing

The well-known method for ground investigation of cone penetration tests was applied. This method consists of pushing a cone with a diameter of 36mm into the ground and measuring the resisting force at the tip of the cone and the friction force on the sides almost continuously using strain gauges inside the cone. The measurements are sent electrically to the surface and recorded there.

The cone is pushed into the ground hydraulically with a constant speed of about 20mm/s. After each meter the penetration process must be stopped for extending the cone penetration testing rod by another meter. The method gives general information about the stratification of the ground as well as an indication of the properties of deformation and failure of the ground. The test was conducted with accordance to Dutch norm NEN 5140. The standard version is type 2 (cone penetration resistance and local friction).

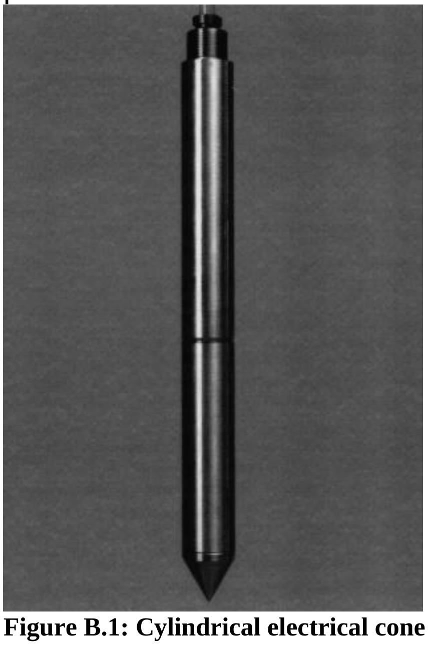

Figure B.1: Cylindrical electrical cone tip

For the determination of the temperature profile with depth temperature cone penetration testing (cone equipped with temperature gauge) was performed. Every 20 centimetres a measurement was taken.
In total 55 electrical cone penetration tests (43 of which with pore pressure), 44 dissipation tests and 9 temperature cone penetration tests were conducted.

B.3 Begemann boring with diameter of 66mm

When performing laboratory tests on soil samples one crucial factor of the process that has a great impact on the quality and reliability of the results is the disturbance of the samples. One of the methods with the minimum possible disturbance is the Begemann system. This system consists of two open tubes, one in the other, that are pushed together into the ground. The external sampling tube has sharp edges and is cutting the soil. The sample is being held in the internal PVC tube that acts as a sample holder. The sample is gradually surrounded by a nylon stocking, which is initially furled in the head of the sampling apparatus and is gradually stripped off during penetration of the apparatus into the soil, while the end of the stocking is kept in position with respect to the ground level by the rope. In this way a continuous sample of great length (to about 18 m) is formed, surrounded by a nylon stocking kept in the slightly wider plastic tube. In between the stocking and plastic tube a thin layer of a heavy supporting drilling liquid is applied. The density of such supporting drilling liquid is selected depending on the soil type, in order to maintain the correct horizontal supporting pressure on the sample. Due to the drilling liquid the friction between the sample and the surrounding tube remains small, so limiting the vertical shear forces on the sample and thus the sample disturbance. During the withdrawal of the Begemann sampling apparatus from the ground the continuous sample is cut in parts of 1 m. The resulting PVC sample holder with a length of 1 meter is closed on both end with a cap and transported to the laboratory standing vertically (partly in contravention of NEN 5119, chapter 7.4.3). In the laboratory these samples, still at 1 metre lengths, are removed from the plastic holder tubes. Then for each sample the volumetric weight at the natural moisture content is determined. From the samples with lengths of 1 metre, representative samples are selected and prepared for classification and mechanical testing. Then the remaining parts are cut longitudinally, photographed, tagged and described according to NEN 5104. The results of the descriptions of the retrieved soil types are presented in the form of a boring profile. In total 36 Begemann borings with a diameter of 66 mm were performed.

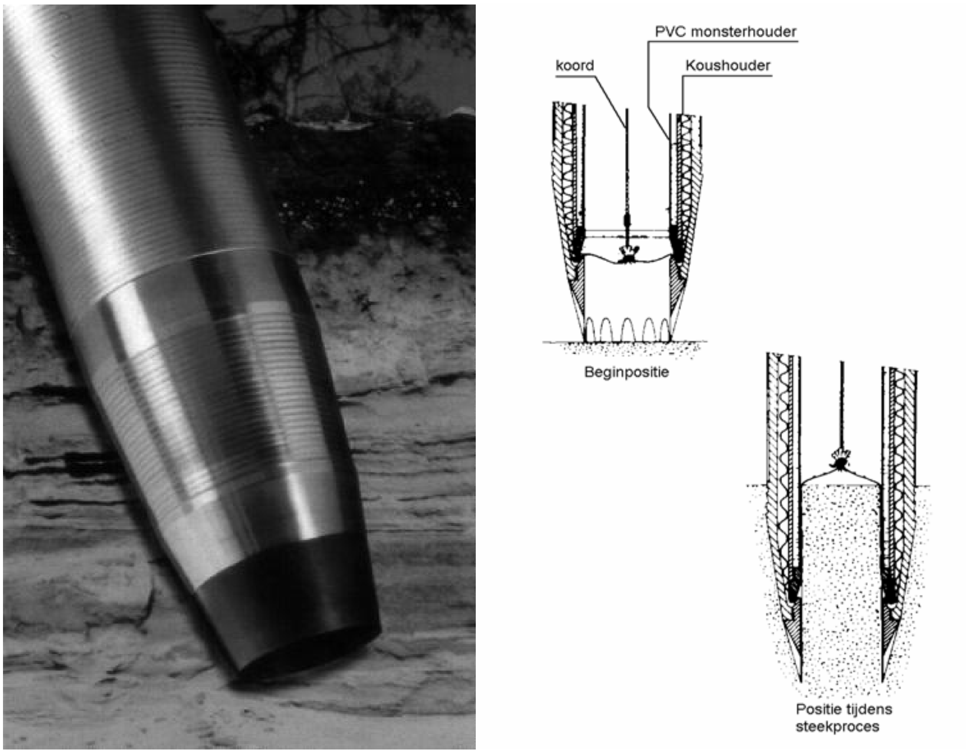

Figure B.2: Operation of Begemann boring system

B.4 Manual boring

A number of shallow Edelman borings were performed. The retrieved sample materials were visually classified. With this boring method fine layering is disrupted. The boring results are presented in the form of descriptions of boring profiles. In total 30 manual borings were conducted

B.5 Observation wells

For determining the hydraulic head observation wells were installed. These consist of steel tubes with a filter at the end that allows water to enter but keeps the soil out. They are pushed into the ground similarly to a cone penetration test and when in place the jacket of the filter is withdrawn and the filter is exposed. The filter consists of a 170mm long nylon or permeable steel. The measurements are taken manually. The placement of the monitoring well and the determination of the hydraulic head were executed in accordance with NEN 5120 and NEN 5766. In total 6 steel observation wells were placed, distributed along 2 measuring lines.


Figure B.3: Steel monitoring

B.6 Pore pressure gauge

The pore pressure gauge consists of a cone equipped with a transducer using a vibrating wire (VW) type of pressure gauge. The cone is pushed into the ground at the required depth and then the pore water is brought into contact with the membrane of the transducer via two filters with a diameter of 10 mm. The accuracy of the measurement is 0.5 kPa (5 cm water column). Transported through a 4-wire electrical cable, the signal can be read anywhere. The measurements are taken automatically and are also corrected for temperature and air pressure variations. In total 42 pore pressure gauges (vibrating wire) were placed. The results of the pore pressure measurements are shown in the form of graphs.

B.7 BAT probe for sampling of ground gas

Normally the BAT probe is used for measuring the permeability of soil. In this case it was used to sample ground gas (peaty soils often contain gas). A loose filter, mounted at the tip of a penetration tube, is pushed into the ground. The filter is closed at the top by means of a butyl rubber membrane. Then the sampling tube, being still at the ground surface, is subjected to a rinsing process in order to remove any remaining oxygen. To this end the sampling tube, which is closed on both sides by means of butyl rubber membranes, is brought under vacuum and rinsed with argon. This process is repeated three times, after which the sampling tube is brought back under vacuum. Remaining under vacuum, the sampling tube is lowered down through the hollow penetration tube towards the filter at its bottom. A double needle construction for connecting the sampling tube up with the filter enables the sampling tube to be brought into contact with the groundwater and ground gas. A pressure gauge, fitted at the top of the sampling tube, enables the measurement of the occurrence of a pressure difference during sampling.

The weights of a sampling tube are measured both before and after sampling. Together with the pressure difference, occurring during sampling, the amount of gas, collected by the sampling tube, can be quantified. The gas samples were analyzed by gas chromatography on methane, nitrogen, oxygen and carbon dioxide in the laboratory of Saybolt in Vlaardingen. Also, the gas analyser of Royal Haskoning was used. This analysis tool is equipped with a built-in pump. By connecting the instrument to the gas probe a direct analysis of the ground-gases as methane, oxygen and carbon dioxide is possible in the field. The closed gas probe is penetrated to the desired depth, after which the probe is opened. In order to judge the processes in the ground, also the groundwater was sampled and analyzed at two locations.

B.8 Camera cone penetration tests

The camera cone penetration test consists of a stainless steel tube with a diameter of 44 mm and a length of about 1 metre. The window of the camera is made of sapphire glass of 5 to 7 mm and is located at about 30 centimetres above the tip of the tube. To obtain good images the camera cone penetration testing apparatus contains a lamp, mirror and camera. An electrical signal cable connects the camera to a video recorder and a monitoring screen. The camera cone penetration tube is pushed into the ground at a speed of preferably 5 mm per second by means of the extension rods and by using standard equipment for cone penetration testing. Simultaneously continuous video recordings are made of the subsurface. Also, the monitoring screen can be watched on-line. To add commentary to the images a microphone is connected to the sound channel of the camera. During this type of penetration testing a beam of light directly illuminates the adjacent soil through the glass window, which image is recorded by the camera. The image shows the ground with a resolution of 752 x 582 pixels. The grain size and colour are clearly visible. Because the images on the monitoring screen are magnified up to 100 times, the camera functions simultaneously as a microscope. This provides information which may not immediately be visible to the naked eye. For example mineral parts like shells become well distinguishable from other mineral parts and small spaces and gas bubbles become visible as well. Camera cone penetration tests were performed at three locations, one at the failure and two on the west side. The camera cone penetration tests were continued to a depth of about 6 m below ground level. The aim of this investigation was to determine the stratification of the ground, in particular thin layers. The second objective was the visualisation of the occurrence of gas in the ground.

C. Laboratory testing methods

C.1 General

As part of the research regarding the Wilnis dike failure a number of laboratory tests were conducted by GeoDelft. These test include:

- K_0-CRS tests: These are advanced continuous oedometric compression tests (CRS = Constant Rate of Strain);
- Isotropic and anisotropic triaxial tests
- Simple Shear tests
- Classification tests

The investigated soil types are clay (Calais), Holland peat, Basis peat and sand.

C.2 K_0-CRS

For testing the special K_0-CRS apparatus of GeoDelft has been used. With this test it is possible to determine many model parameters from one small sample. The K_0-CRS tests are executed in an adapted triaxial apparatus, see Figure C.1. GeoDelft uses a triaxial apparatus with slow-displacement control by means of a step-motor for loading. The minimum speed is about 0.1 mm / day. The maximum vertical pressure on the top platen is about 600 kPa for the K_0-apparatus and 3800 kPa for the standard apparatus.

For the CRS-test with K_0-measurement a special sample with an internal diameter of 65 mm is used. The sample height can be adjusted for the expected compression behaviour. For stiff clay samples an initial height of 20 mm is used, while for peat and soft clay taller samples can be tested. The sample holder consists of a metal ring, in the lower 2 cm of which a constriction has been applied. At the level of this constriction the sample holder has a wall thickness of only 0.6 mm and a strain gauge has been attached to measure the horizontal stress. Because of the high sensitivity of the strain transducer to temperature the tests are conducted in a room with constant temperature.

At the beginning of the test the zero point of the displacement is adjusted at a minor surcharge of about 3 kPa. The standard strain rate is approximately $1.9 * 10^{-6}$ s^{-1}, which corresponds to 3.3 mm / day for a sample height of 20mm.

In the current test series the following standard schedule has been applied:

- Loading up to 130 kPa
- Unloading down to 30 kPa
- Reloading up to 200 kPa
- Relaxation (decrease of pressure at constant height) during 16 hours
- Loading up to 250 kPa
- Unloading and dismantling

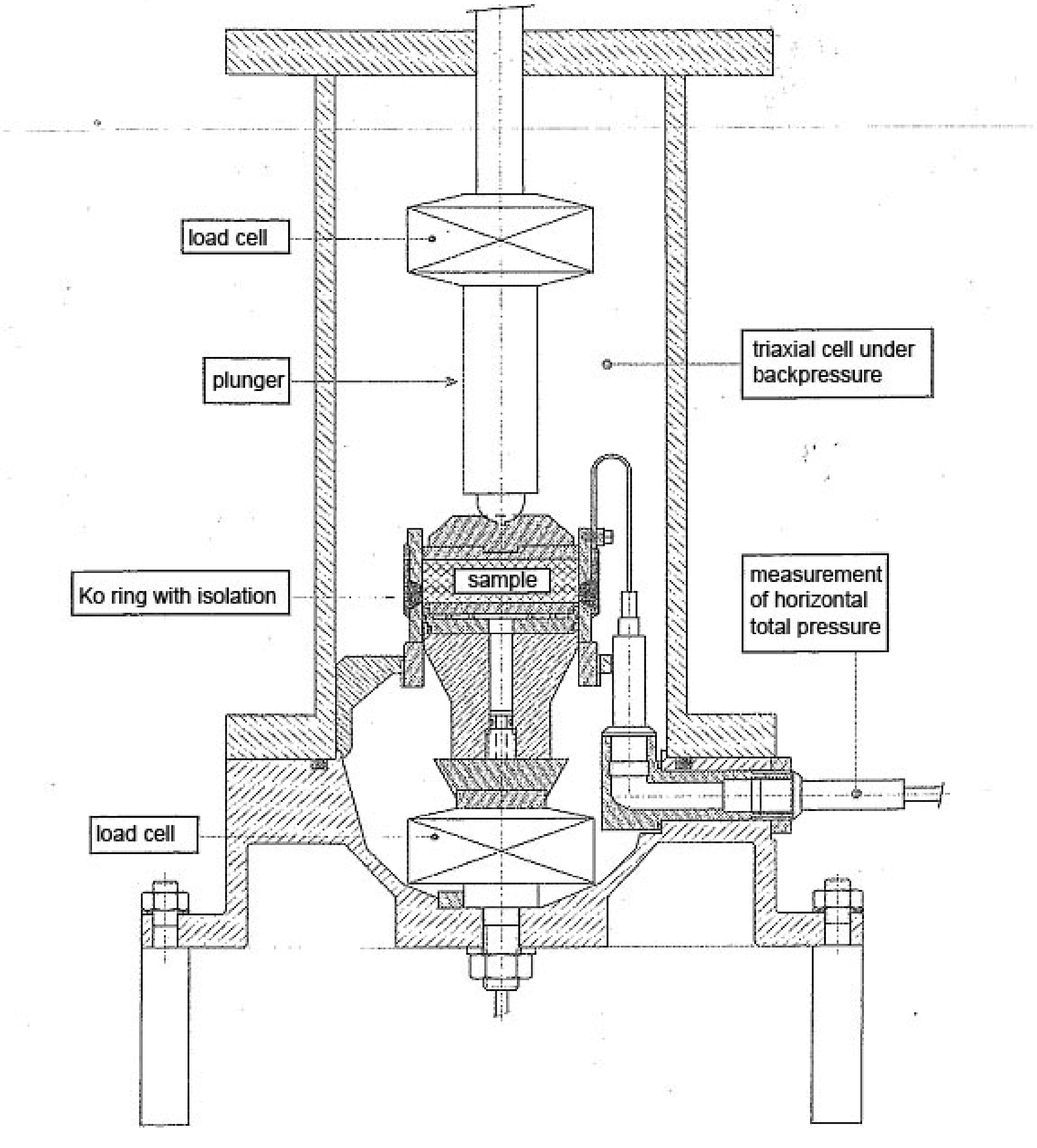

Figure C.1: Vertical cross section of K_0-CRS apparatus

C.3 Triaxial tests

The triaxial test is described in detail in norm NEN 5117. Clay and peat samples are tested in an undrained way while for sand samples drained testing is applied. These tests provide shear strength and stiffness parameters. Notwithstanding NEN 5117 a test is usually performed using anisotropic consolidation, which means that the sample is consolidated at a non-unit K_0-value, which is the ratio of horizontal and vertical pressures (σ_h/σ_v) being not equal to 1.0. For the reported testing series K_0-values between 0.4 and 0.53 were applied.

The tests are all performed single staged, which means that each sample is loaded to peak failure or 15% strain. The standard sample height is 15 cm and the diameter 63 mm. The loading period is set at approximately 16 hours. The drained sand samples have then already completely consolidated. The consolidation time t_{100} is in the order of 20 minutes. The rate of shearing at failure is related to t_{100} and amounts to 4% to 8% / hour. Note that for 15% strain in 15 hrs a prescribed rate of 1% / hour would be needed.

C.4 Simple shear tests

In the literature the simple shear test is often indicated as Direct Simple Shear test and abbreviated to DSS. However this would only be justified if also a horizontal failure plane would be enforced. In this test a flat sample is subjected to plane deformation with a linearly increasing shear strain with time, while the developing shear stress is measured. Figure C.2 shows the deformation as seen from the side. The sides of the sample are supported by a reinforced membrane, so that the sample diameter remains more or less constant, in accordance with the definition of “simple shear”.

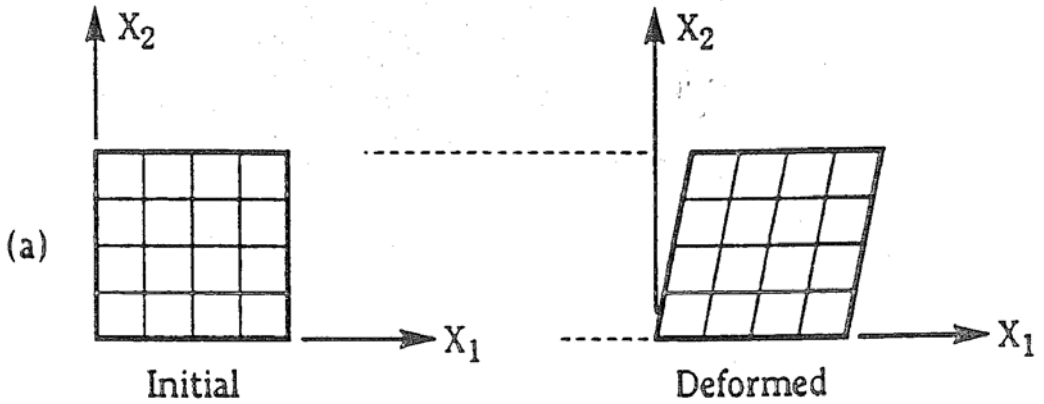

Figure C.2: Enforced deformation for simple shear testing

Both the lateral (horizontal) pressure and the pore water pressure are not measured. The maximum shearing force determines the peak shear strength of the material. Unlike in the triaxial test, the stress state in the simple shear sample is not homogeneous. An important difference between the direct shear and simple shear tests is that in a direct shear test a horizontal shear plane is enforced, while in a simple shear test the failure plane can develop in the weaker region of the sample.
In the current test series during shearing the height of the sample is kept constant. This allows the vertical pressure to change depending on the type of soil, namely increasing in dense sand and decreasing in very loose soils.

At failure the simple shear tests produce a peak value of the horizontal shear stress τ at an effective vertical stress $\sigma_v^{'}$. The interpretation of these data is not trivial, because the horizontal pressure at the membrane, the horizontal shear stress and the orientation of any failure plane remain unknown. To obtain a transparent elaboration usually the following approximation is applied: the failure plane is assumed horizontal, enabling the calculation of both the horizontal shear force and the vertical normal force. From these the corresponding horizontal shear stress τ and vertical normal effective stress $\sigma_v^{'}$ can be derived. The horizontal shear stress is corrected for the friction in the system (0.3 kPa) and for the strain dependent shear stress in the membrane by means of the following formula:

$$\tau_c = \tau - 0.3 - 0.09\gamma_h \text{ [kPa]}$$

in which

τ = measured shear stress [kPa]
γ_h = measured angular distortion [%]

D. Plaxis input data

General Information

Table [1] units

Type	Unit
Length	m
Force	kN
Time	day

Table [2] Model dimensions

	min.	max.
X	0,000	100,000
Y	-25,000	0,000

Table [3] Model

Model	Plane Strain
Element	15-Noded

Geometry

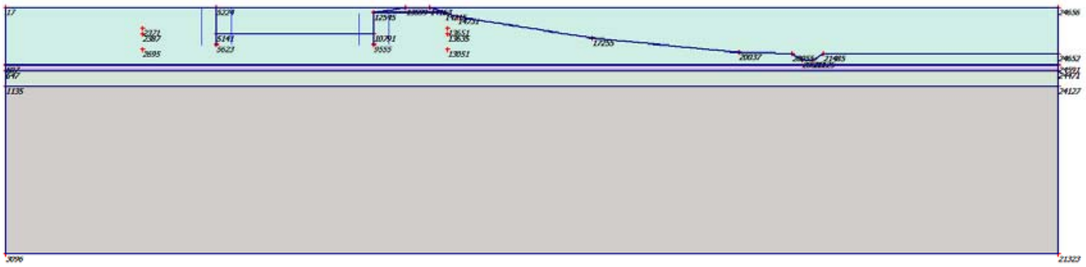

Fig. 1 Plot of geometry model with significant nodes

Table [4] Table of significant nodes

Node no.	x-coord.	y-coord.	Node no.	x-coord.	y-coord.
3096	0,000	-25,000	5141	20,000	-4,000
21323	100,000	-25,000	10791	35,000	-4,000
17	0,000	-1,500	507	0,000	-7,000
5224	20,000	-1,500	24591	100,000	-7,000
12545	35,000	-2,000	647	0,000	-7,500
13599	38,000	-1,500	24471	100,000	-7,500
14163	40,300	-1,500	1135	0,000	-9,000
14731	42,900	-2,400	24127	100,000	-9,000
17255	55,700	-4,400	24656	100,000	-1,500
20037	69,700	-5,800	2371	13,000	-3,500
20955	74,700	-5,900	2387	13,000	-4,000
20609	75,700	-6,500	2695	13,000	-5,500
21125	76,700	-6,500	13651	42,000	-3,500
21485	77,700	-5,900	13635	42,000	-4,000
24652	100,000	-5,900	13051	42,000	-5,500
9555	35,000	-5,000	14215	41,744	-2,000
5623	20,000	-5,000			

Clusters

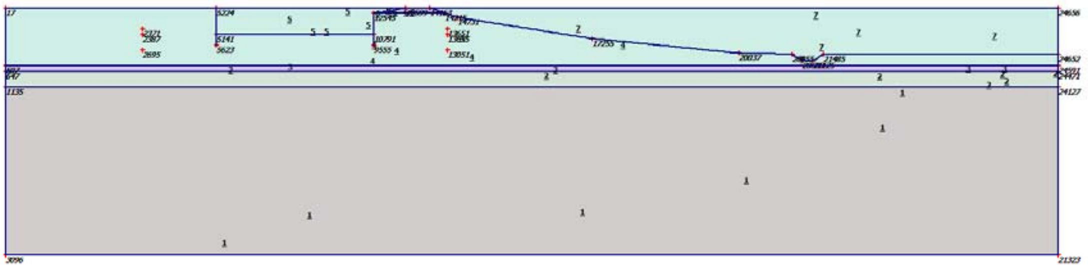

Fig. 2 Plot of geometry model with cluster numbers

Table [5] Table of clusters

Cluster no.	Nodes
1	3096, 21323, 1135, 24127.
2	647, 24471, 1135, 24127.
3	507, 24591, 647, 24471.
4	17, 5224, 12545, 14731, 17255, 20037, 20955, 20609, 21125, 21485, 24652, 9555, 5623, 5141, 10791, 507, 24591, 2371, 2387, 2695, 13651, 13635, 13051, 14215.
5	5224, 12545, 13599, 5141, 10791.
6	12545, 13599, 14163, 14215.
7	14163, 14731, 17255, 20037, 20955, 20609, 21125, 21485, 24652, 24656, 14215.

Structures

Fig. 3 Plot of geometry model with structures

Table [6] Beams

Plate no.	Data set	Length [m]	Nodes
1	Wooden sheet piling	2,000	13635, 13651, 13635.
2	Wooden sheet piling	2,000	2387, 2371, 2387.
3	Wooden sheet piling	3,000	12545, 10791, 9555.
4	Wooden sheet piling	3,500	5141, 5224,

Table [7] Interfaces

Interface no.	Data set	Nodes
1	Holland peat Sand	12545, 10791, 10791, 9555, 9555, 10791. 10791, 12545.
2	Holland peat Sand	5141, 5224, 5141, 5623, 5623, 5141. 5224, 5141.

Table [8] Node-to-node anchors

Anchor no.	Data set	Length [m]	First node	Last node
1	Anchor rod	7,433	2387	5224
2	Anchor rod	7,280	12545	13635

Mesh data

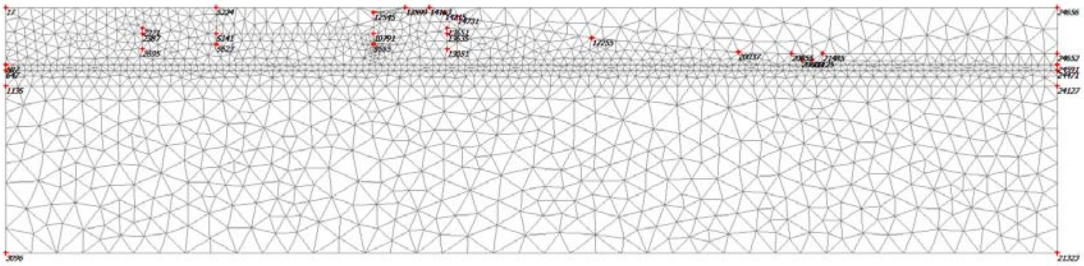

Fig. 4 Plot of the mesh with significant nodes

Table [9] Numbers, type of elements, integrations

Type	Type of element	Type of integration	Total no.
Soil	15-Noded	12-point Gauss	3050
Plate	5-node line	4-point Gauss	19
Interface	5-node line	4-point Newton-Cotes	26

Material data

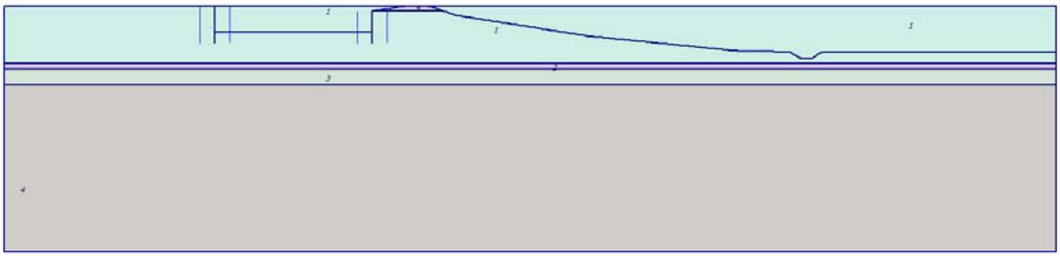

Fig. 5 Plot of geometry with material data sets

Table [10] Soil data sets parameters

Hardening Soil		1 **Holland peat**	2 **Clay**	3 **Basis peat**	4 **Sand**
Type		UnDrained	UnDrained	UnDrained	Drained
γ_{unsat}	[kN/m³]	6,40	9,00	7,50	17,00
γ_{sat}	[kN/m³]	9,80	11,90	10,10	20,10
k_x	[m/day]	0,040	0,001	0,004	5,000
k_y	[m/day]	0,040	0,001	0,004	5,000
e_{init}	[-]	3,27	1,59	3,27	0,58
e_{min}	[-]	0,00	0,00	0,00	0,00
e_{max}	[-]	999,00	999,00	999,00	999,00
c_k	[-]	1E15	1E15	1E15	1E15
E_{50}^{ref}	[kN/m²]	2200,00	2000,00	250,00	12000,00
E_{oed}^{ref}	[kN/m²]	970,40	2022,64	670,32	6067,61
power (m)	[-]	1,00	1,00	1,00	0,50
c_{ref}	[kN/m²]	4,58	8,15	9,70	1,79
φ	[°]	26,40	18,20	20,00	31,20
ψ	[°]	0,00	0,00	0,00	0,00
E_{ur}^{ref}	[kN/m²]	5000,00	6000,00	1800,00	50000,00
$\nu_{ur}^{(nu)}$	[-]	0,200	0,200	0,200	0,200
p^{ref}	[kN/m²]	100,00	100,00	100,00	100,00
$c_{increment}$	[kN/m²]	0,00	0,00	0,00	0,00
y_{ref}	[m]	0,00	0,00	0,00	0,00
R_f	[-]	0,90	0,90	0,90	0,90
$T_{str.}$	[kN/m²]	0,00	0,00	0,00	0,00
R_{inter}	[-]	1,00	1,00	1,00	1,00
δ_{inter}	[m]	0,00	0,00	0,00	0,00
Interface permeability		Neutral	Neutral	Neutral	Neutral

Table [11] Beam data sets parameters

no.	**Identification**	**EA** [kN/m]	**EI** [kNm²/m]	**w** [kN/m/m]	**ν** [-]	**Mp** [kNm/m]	**Np** [kN/m]
1	Wooden sheet piling	500,00	104,17	8,30	0,15	1E15	1E15

Table [12] Anchor data sets parameters

no.	**Identification**	**EA** [kN]	**|Fmax,comp|** [kN]	**|Fmax,tens|** [kN]	**L spacing** [m]
1	Anchor rod	62832,00	1E15	1E15	2,50